SCUOLA DI DOTTORATO
UNIVERSITÀ DEGLI STUDI "MEDITERRANEA" DI REGGIO CALABRIA
UNIVERSITÀ DEGLI STUDI DI MESSINA

DOTTORATO DI RICERCA IN
INGEGNERIA CIVILE, AMBIENTALE E DELLA SICUREZZA

CURRICULUM
INGEGNERIA IDRAULICA, COSTRUZIONI IDRAULICHE E MARITTIME,
IDROLOGIA ED ENERGIA DALLE ACQUE

XXXI CICLO

HYDRODYNAMICS OF INTERACTING WAVES AND CURRENTS IN THE NEARSHORE ZONE

Dottorando:
Carmelo Petrotta

Tutor:
Prof. Carla Faraci

Coordinatore:
Prof. Felice Arena

REGGIO CALABRIA, APRILE 2019

Carmelo Petrotta

HYDRODYNAMICS OF INTERACTING WAVES AND CURRENTS IN THE NEARSHORE ZONE

The author wish to thank the Tutor and the Referees for their valuable comments.

Cover photo:
Sand ripples at San Leone (Agrigento), Italy

"*La vita si ascolta così come le onde del mare... Le onde montano... crescono... cambiano le cose... Poi, tutto torna come prima... ma non è più la stessa cosa....*"

Alessandro Baricco

Contents

Abstract

Detailed measurements are presented of the hydrodynamics and the morphodynamics in the nearshore zone. Measurements were obtained throughout three experimental campaigns. Both small and large scale models were adopted, thus allowing to analyse the wave-current interaction and its effects on the nearbed morphodynamics. Both co-linear and orthogonal waves and currents were reproduced.

Measurements focused particularly on the dynamics of the wave bottom boundary layer in terms of velocity statistics, i.e. standard deviation, skewness and kurtosis, of turbulent kinetic energy and Reynolds stresses. The effects of such complex flow on the nearbed morphodynamics were examined. The hydrodynamics was measured by means of both acoustic and laser Doppler velocimeters whereas bedform shape and migration were measured by means of a structured light approach.

Waves interacting with a sloping rippled bed were observed to give rise to steady flow components as the Longuet-Higgins steady streaming and the wave-asymmetry steady streaming, the undertow and the Stokes drift. The high turbulence generated by the wave breaking considerably influenced the sediment transport in the nearshore zone, both within the small scale model and the large scale model. These phenomena caused ripples to be asymmetric and to migrate downward in the offshore direction.

Above a horizontal rough bed, the waves superimposing at a right angle on a current was examined. Their influence on the bottom boundary layer both in terms of the equivalent roughness and the friction velocity was analysed. An overview of the two conditions of wave dominated and current dominated flow above both small and big roughness bottoms was described.

1 Introduction

Waves gather their energy and momentum from winds blowing over possibly huge areas. During their motion, waves keep this energy as long as they reach the nearshore zone where the wave bottom interaction starts. Due to this interaction, waves gradually become skewed and asymmetric, with sharp crests and flat troughs. The wavefront steepness increase leads to the wave breaking, within the surf zone where much of the accumulated energy is dissipated. The organized wave motion makes room for a chaotic turbulence, which acts on non-cohesive beaches mobilizing and suspending loose sediments. Moreover, the breaking waves create nearshore currents that flow along the shoreline and in the cross-shore direction. These currents can transport large quantities of sediment in both directions in volumes as large as hundreds of thousands of cubic meters of sand per year in some places, thus considerably transform the shoreline.

1.1 Aim of the study

During the past several decades, the foreshore developed due to many economic reasons like commerce, tourism, mobility, housing needs, etc. At the same time, increasing emphasis was placed on the knowledge of natural coastal processes in order to design effective coastal protection works and mitigate erosion problems.

Thus, in recent years, the attention on the behaviour of the sand and water at the shoreline grew. Nevertheless, sometimes the complex mathematical and statistical equations which govern the coastal phenomena could not be analytically solved. These cases could be handled by the modelling or by the direct numerical simulations in the case of low Reynolds Numbers.

The present thesis describes three campaigns aimed at analysing the waves plus current propagating over rough beds, which could assist in literature model calibration. Particular attention was given to the near-bed region hydro-morphodynamics. Thus, since physical processes interact at different scales, different models are required to address different questions. It is always auspicable to work with large

scale model as scale effects are reduced to a minimum. The advantage of small scale model is that they are cheaper and measurements can be more easily carried out. Large-scale models are preferred to examine the boundary layer and the near-bed vorticity within the breaking zone.

1.2 Methodology

The hydrodynamics of the coastal zone was analysed by three experimental campaigns. The hydro-morphodynamics of a sloping bed was investigated within the small-scale wave flume of the University of Messina (Italy); the hydrodynamics of the breaking zone was examined within the large-scale wave flume of the Universitat Politècnica de Catalunya (Spain); lastly, the waves and current at a right angle were analysed within DHI (Denmark) shallow water basin.

More in details, the small-scale campaign focused on the near-shore hydrodynamics over a sloping rippled bed. It consisted of two parts, the first of which deals with the influence of the bottom slope on the wave and flow asymmetry, undertow and bedform shape and migration. Moreover, it examined the near-shore morphodynamics with a particular interest in the ripple growth process, the reaching of the equilibrium shape and its asymmetry due to the wave asymmetry and undertow.

Throughout the second part of the campaign, the experimental set up was improved by fixing ripples at the equilibrium by a thin layer of concrete. In such a way, near-bed data-scattering produced by the high suspended sediment concentration was avoided and hydrodynamics could be more carefully measured. Moreover, the absence of ripple migration allowed several measuring positions within a ripple length to be set which are useful to analyse, more in detail, the effects of ripples on the near-bed hydrodynamics, more in detail.

Within the large-scale wave flume, the monochromatic wave plunging over a fixed bar was studied. Both the bottom boundary layer and the lower part of the water column was investigated in order to provide insights on the mean velocity distribution, turbulent velocity fluctuations and Reynolds stresses.

Finally, throughout the shallow water basin campaign, the hydrodynamics generated by wave superimposition on a current at a right angle was studied. The boundary layer structure and, in particular, the equivalent roughness and the friction velocity were analysed by discriminating the current-dominated regime and the wave-dominated regime.

1.3 Outline of the thesis

The thesis consists of five chapters and some conclusions as described below. Chapter 2 includes an overview of the near-shore hydrodynamics with particular regard to the wave-current interaction within the near-bed region which includes the wave bottom boundary layer. Although in nature, waves and current co-exist at various angles the co-directional case and the orthogonal case are examined separately for sake of clarity.

Chapter 3 describes the instruments deployed during the three experimental campaign successively described. More in detail, velocities were measured by both acoustic Doppler velocimeters and laser Doppler anemometers; instead, waves characteristics were measured by resistive wave gauges, acoustic wave gauges and pressure pore transducers.

Chapter 4 describes the experimental campaign carried out within the small scale wave flume of the University of Messina. Experimental set-up, measurements and data treatment were reported. The influence of the sloping bed on the flow and, in turn, on ripple asymmetry and migration were analysed. Moreover, the near-bed velocity statistics and turbulence were reported. For the reason of readability, the two parts of the campaign which involved respectively a moveable and a fixed rippled bed were separately described. Nevertheless, experimental results were jointly discussed as two points of views of the same phenomenon.

Chapter 5 describes the experimental campaign carried out within the LIM-UPC in Barcelona. Differently from the other two campaigns where, under the supervision of Prof. C. Faraci, I managed the whole experiment, i.e. set up building, data collection, treatment and analysis, throughout the present experiment I contributed as a part of a team and I mainly focused on data collection and treatment. Nevertheless, the analyses earlier presented by Scandura et al. (2018) and here reported help to reach a deeper understanding of the co-linear wave and current propagation above a sloping beach. More in detail, the fourth chapter of this thesis examines the turbulent velocity fluctuations within the breaking zone.

Chapter 6 describes the experimental campaign carried out within the DHI Denmark shallow water basin. A prominent place is given to the instrumentation deployed and to data treatment procedures. The main results achieved throughout the experimentation regarding the wave superimposition on a current, in terms of bed equivalent roughness and friction velocity were reported.

The general conclusions (Chapter 7) examine the implications of the present study's results for the future development of both near-shore hydrodynamic and

morphodynamic models.

2 Coastal hydrodynamics

In a coastal environment, waves interact with currents, tides or even storm surges and tsunamis, giving rise to a complex kinematic. Its prediction is a task involved in a large number of engineering problems covering two main fields: the design of offshore and nearshore structures and the computation of sediment transport on the shoreface and in the nearshore zone.

In particular, the mechanisms by which waves and currents mutually interact were summarized by Soulsby et al. (1993):

(a) refraction of the waves by horizontally sheared currents;

(b) modification of wave kinematics by the (possibly vertically sheared) current;

(c) generation by the waves of "mass transport" or "streaming" currents;

(d) generation by the waves of radiation stresses giving rise to currents, particularly longshore currents in the surf zone;

(e) enhancement of the bottom friction felt by the currents, due to the interaction with the wave boundary layer;

(f) enhancement of the bed shear-stresses and energy dissipation of the waves, due to interaction with the current boundary layer.

Furthermore, if the flow is propagating over a non-cohesive bed, sedimentary structures like ripples, bars, dunes may appear.

This thesis is mainly focussed on the wave-current interaction in the vertical plane, i.e. mechanisms (b), (c), (d), (e), (f). Discussions about mechanism (a) and (d) can be found in Peregrine (1976); Grant and Madsen (1986); Jonsson (1990); Sleath (1990).

2.1 The bottom boundary layer

The flow generated by the interaction of waves and currents propagate in a viscous fluid over an irregular bottom of varying permeability. The main body of the fluid motion is, in most cases nearly irrotational. This is because the viscous effects are usually concentrated in thin "boundary" layers near the surface and the bottom. The bottom boundary layers generated by the steady flow and the oscillating flow are here described.

2.1.1 The bottom boundary layer in a steady flow

Within a wall-bounded turbulent flow, shear stresses can be classified as viscous or turbulent in accordance with their origin. This leads to the identification of two different scaling laws. The first is known as the *law of the wall* and it applies throughout the region of the boundary layer where viscosity matters and the largest relevant length scale is y, the distance from the wall. This region of the flow is typically called the *inner layer*. The second scaling law is known as the *velocity defect law*, and it applies where the flow is largely independent of viscosity and the largest relevant length scale is the overall thickness of the turbulent layer δ. This region of the flow is typically called the *outer layer*. Fortunately, the inner and outer layers of wall-bounded turbulent flow overlap and, in this overlap region, the form of the mean stream-wise velocity profile may be deduced from dimensional analysis.

2.1.2 Inner layer: law of the wall

The velocity profile near the water bottom does not depend on the free stream velocity or the thickness of the flow but on the shear stress at the wall τ_0, on the water density ρ, on the kinematic viscosity of the water ν and, finally, on the distance to the wall y

$$U = U(\tau_0, \rho, \nu, y). \tag{2.1}$$

Because of both τ_0 and ρ involve the dimension of the mass, it is possible to combine them in the ratio

$$u_* = \sqrt{\frac{\tau_0}{\rho}} \tag{2.2}$$

that has the dimension of a velocity and is called friction velocity. Equation 2.1 can then be written as

$$U = U(u_*, \nu, y). \tag{2.3}$$

According to the π theorem there must be only $4-2=2$ non-dimensional groups U/u_*, and yu_*/ν, which should be related by some universal functional form

$$U_+ \equiv \frac{U}{u_*} = f\left(\frac{yu_*}{\nu}\right) = f(y_+). \tag{2.4}$$

Equation 2.4 is called *law of the wall* and states that U/u_* is a function of the distance from a smooth wall non-dimensionalised by the *viscous scale* $l_\nu = u_*/\nu$.

The subscript plus signs are standard in the literature and indicate a dimensionless law-of-the-wall variable. The inner part of the wall layer, right next to the wall, is dominated by viscous effects (Figure 2.1) and is called the viscous sublayer. It used to be called the "laminar sublayer" until experiments revealed the presence of considerable fluctuations within the layer. In spite of the fluctuations, the Reynolds stresses are still small here because of the dominance of viscous effects. At high Reynolds numbers, the viscous sublayer is thin enough so that the stress is uniform within the layer and equal to the wall shear stress τ_0. Therefore the mean velocity gradient in the viscous sublayer is given by

$$\mu \frac{dU}{dy} = \tau_0 \tag{2.5}$$

which shows that the velocity distribution is linear. Integrating, and using the no-slip boundary condition, we obtain

$$U = \frac{\tau_0 y}{\mu} \tag{2.6}$$

In terms of non-dimensional variables appropriate for a wall layer, this can be written as

$$U_+ \equiv \frac{U}{u_*} = y_+ \tag{2.7}$$

Experiments show that the linear distribution holds up to $yu_*/\nu \sim 5$, which may be taken to be the limit of the viscous sublayer.

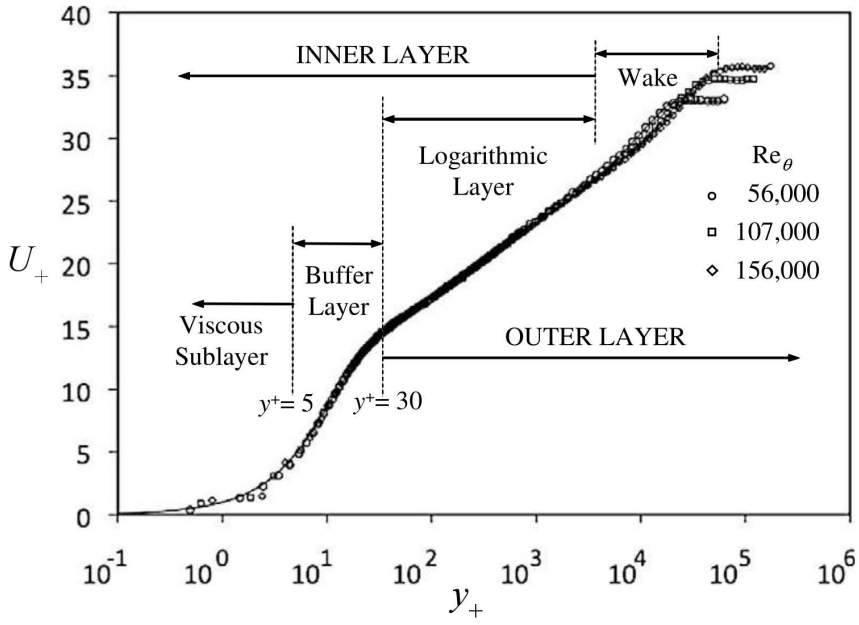

Figure 2.1: Mean velocity profile of a smooth-flat-plate turbulent boundary layer plotted in log-linear coordinates with law-of-the-wall normalizations, (Kundu et al., 1990). The data are replotted from Oweis et al. (2010) and represent three Reynolds numbers. The extent of the various layers within a wall-bounded turbulent flow are indicated by vertical dashed lines. The log-layer-to-wake-region boundary is usually assumed to begin at y/d z0.15 to 0.20 in turbulent boundary layers. Overall the data collapse well for the inner layer region, as expected, and the logarithmic layer extends for approximately two decades. The wake region shows differences between the Reynolds numbers because its similarity variable is y/δ, and δ/l_v differs between the various Reynolds numbers.

2.1.3 Outer layer: velocity defect law

Within the outer part of the turbulent boundary layer, the gross characteristics of the turbulence in the outer region are inviscid and resemble those of a free shear flow. The existence of Reynolds stresses in the outer region results in a drag on the flow and generates a velocity defect $\Delta U = U_\infty - U$, just like the planar wake: the so-called *velocity defect law* show its dependence on the friction velocity u_* and on the boundary layer thickness δ

$$\frac{U_\infty - U}{u_*} = F\left(\frac{y}{\delta}\right) = F(\xi). \tag{2.8}$$

2.1.4 Overlap layer: logarithmic law

The mean velocity profiles in the inner and outer layers of a wall-bounded turbulent flow are governed by different laws, (2.4) and (2.8), in which the independent coordinate y is scaled differently. Distances in the outer part are scaled by δ, whereas those in the inner part are scaled by the much smaller viscous wall unit $l_\nu = \nu/u_*$. Thus, wall-bounded turbulent flows involve at least two turbulent length scales, and this prevents them from reaching the same type of self-similar form with increasing Reynolds number as that found for simple free turbulent shear flows.

A region of overlap in the two profile forms can be found by taking the limits $y_+ \to \infty$ and $\xi \to 0$ simultaneously, as shown by Kundu et al. (1990)

$$U_+ = \frac{U}{u_*} = \frac{1}{\kappa}\ln(y_+) + B \tag{2.9}$$

$$F(\xi) = -\frac{1}{\kappa} ln(\xi) + A \tag{2.10}$$

where B and A are constants with values around 4 or 5, and 1, respectively, and $\kappa = 0.4$ is the von Kármán constant. Equation (2.9) or (2.10) is the mean velocity profile in the overlap layer or the logarithmic layer. They are only valid for large y_+ and small y/δ, respectively.

Experimental confirmation of the logarithmic law (2.9) is shown in Figure 2.2a in law-of-the-wall coordinates for the turbulent boundary-layer data reported in Oweis et al. (2010). Nominal specifications for the extent of the viscous sublayer, the buffer layer, the logarithmic layer, and the wake region are shown there as well. On this log-linear plot, the linear viscous sublayer profile appears as a curve for

$y_+ < 5$. However, a logarithmic velocity profile will appear as a straight line on a log-linear plot, and such a linear region is evident for approximately two decades in y_+ starting near $y_+ \sim 10^2$. The extent of this logarithmic region increases in these coordinates with increasing Reynolds number. The region $5 < y_+ < 30$, where the velocity distribution is neither linear nor logarithmic, is called the buffer layer. Neither the viscous stress nor the Reynolds stresses are negligible here, and this layer is dynamically important because turbulence production reaches a maximum here. Overall, the measured results collapse well to a single curve below $y_+ \sim 10^4$ (or $y/\delta \sim 0.2$) in conformance with the law of the wall. For larger values of y_+, the collapse ends where the overlap region ends and the boundary layer's wake flow begins. Although the wake region appears to be smaller than the log-region on the plot, this is an artefact of the logarithmic horizontal axis. A turbulent boundary layer's wake region typically occupies the outer 80% of the flow full thickness.

2.1.5 Rough surfaces

In deriving the logarithmic law (2.9), it was assumed that the flow in the inner layer is determined by viscosity. This is true only for hydrodynamically smooth surfaces, for which the average height of the surface roughness elements is smaller than the thickness of the viscous sublayer. For a hydrodynamically rough surface, on the other hand, the roughness elements like ripples protrude out of the viscous sublayer. A wake develops behind each roughness element, and shear stress is transmitted to the wall by the resulting drag on the roughness elements. Viscosity becomes irrelevant for determining either the velocity distribution or the overall drag on the surface.

The velocity distribution near a rough surface is again logarithmic, but the intercept constant can be set by noting that the mean velocity U is expected to be negligible somewhere within the roughness elements (Figure 2.2b). We can, therefore, assume that (2.9) applies for $y > y_0$, where y_0 is a measure of the roughness heights and is defined as the value of y at which the logarithmic distribution gives $U = 0$. It could be also expressed by the Nikuradse equivalent sand roughness $y_0 = k_s/30$.

Appropriately evaluating the constant B in (2.10) then produces

$$U_+ = \frac{U}{u_*} = \frac{1}{\kappa} \ln\left(\frac{y}{y_0}\right). \tag{2.11}$$

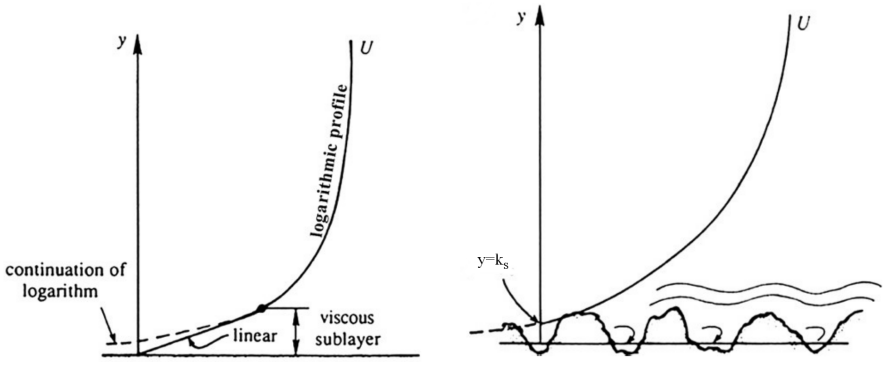

Figure 2.2: Logarithmic velocity distributions near smooth (a) and rough (b) surfaces (Kundu et al., 1990). The presence of roughness may eliminate the viscous sublayer when the roughness elements protrude higher than several l_ν. In this case the log-law may be extended to a virtual wall location k_s where U appears to go to zero.

2.1.6 The bottom boundary layer in a oscillating flow

Formulation of the problem The velocity field beneath a water wave can be analysed by means of the Navier Stokes equation and the continuity equation. The non linear system of equations requires suitable boundary conditions and can be solved only introducing significant approximations.

Figure 2.3 shows a monochromatic, two dimensional, small amplitude wave which propagates above a horizontal plane bed. Being (x,y) the reference system, where x lying on the bottom in the direction of the wave propagation and y is upward at a right angle with the abscissae axis. Moreover, the following parameters are defined:

- L is the wavelength [m];
- $H(x,y,t)$ is the wave height [m];
- T is the wave period [s];
- $\eta(x,y,t)$ is the surface elevation with respect to the mean water level [m];

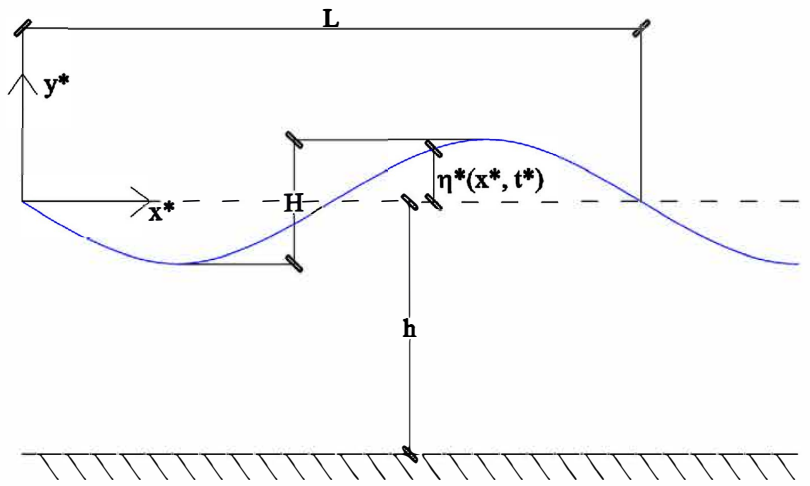

Figure 2.3: Wave characteristics.

- h is the water depth [m];
- $H(x,y,t)$ is the wave height [m];
- $A = H/2$ is the wave amplitude [m];
- $k = 2\pi/L$ is the wave number [m^{-1}];
- $\omega = 2\pi/T$ is the angular frequency [s^{-1}];
- U, V are the velocity components in the directions x and y [$\mathrm{m}\cdot\mathrm{s}^{-1}$];
- ρ is the water density [$\mathrm{kg}\cdot\mathrm{m}^{-3}$];
- μ is the water dynamic viscosity [$\mathrm{kg}\cdot\mathrm{m}^{-1}\cdot\mathrm{s}^{-1}$];
- ν is the water kinematic viscosity [$\mathrm{m}^{2}\cdot\mathrm{s}^{-1}$];
- g is the gravitational acceleration [$\mathrm{m}\cdot\mathrm{s}^{-2}$].

When the assumptions of inviscid fluid ($\mu = 0$), incompressible (ρ=constant), heavy (mass forces are proportional to the gravitational acceleration, thus $\underline{f} = -g \cdot \nabla y$); irrotational flow (the flow vorticity is zero, $\nabla \times \underline{v} = 0$); small amplitude progressive waves are propagated ($H/L << 1$) are made, it is possible to separate the study of the flow field from the study of the pressure field by means of the Laplace equation:

$$\nabla^2 \phi = 0 \tag{2.12}$$

The following boundary conditions must be introduced:

- at the bottom the vertical component of the velocity is null

$$\frac{\partial \phi}{\partial y} = 0 \quad \text{for } y = 0 \tag{2.13}$$

- water particles cannot detach or permeate the water surface. This leads to the kinematic free-surface boundary-condition

$$\frac{\partial \phi}{\partial y} = \frac{\partial \eta}{\partial t} + \frac{\partial \phi}{\partial x} + \frac{\partial \eta}{\partial x} \quad \text{for } y = \eta(x,t) + h \tag{2.14}$$

- the dynamic free-surface condition is provided by Bernoulli's equation for an unsteady potential flow which assures the pressure continuity across the water surface

$$-\frac{\partial \phi}{\partial t} + \frac{P_\eta}{\rho} + \frac{1}{2}\left[\left(\frac{\partial \phi}{\partial x}\right)^2 + \left(\frac{\partial \phi}{\partial y}\right)^2\right] + g\eta = 0 \quad \text{for } y = \eta(x,t) + h \tag{2.15}$$

where P_η is the pressure at $\eta(x,t)$ which is assumed equal to zero. The free-surface conditions can be linearised, thus obtaining:

$$\begin{aligned} &\nabla^2 \phi = 0 \\ &\frac{\partial \phi}{\partial y} = 0 \qquad \text{for } y = 0 \\ &\frac{\partial \phi}{\partial y} = \frac{\partial \eta}{\partial t} \quad \text{for } y = h \\ &\frac{\partial \phi}{\partial t} = -g\eta \quad \text{for } y = h. \end{aligned} \tag{2.16}$$

By separating variables, it can be written

$$\phi = \frac{H}{2} \cdot \frac{g}{\omega} \cdot \frac{cosh\,(ky)}{cosh\,(kh)} \cdot sin\,(kx - \omega t)\,. \tag{2.17}$$

The velocity components for a monochromatic wave can be obtained by deriving ϕ with respect to x and y

$$\begin{aligned} U &= \frac{\partial \phi}{\partial x} = \frac{H}{2} \cdot \frac{gk}{\omega} \cdot \frac{cosh\,(ky)}{cosh\,(kh)} \cdot cos\,(kx - \omega t) \\ V &= \frac{\partial \phi}{\partial y} = -\frac{H}{2} \cdot \frac{gk}{\omega} \cdot \frac{sinh\,(ky)}{cosh\,(kh)} \cdot sin\,(kx - \omega t)\,. \end{aligned} \tag{2.18}$$

Above an horizontal plane bed, at $y = 0$

$$\begin{aligned} U &= \frac{H}{2} \cdot \frac{gk}{\omega} \cdot \frac{1}{cosh\,(kh)} \cdot cos\,(kx - \omega t) = U_0 \cdot cos\,(kx - \omega t) \\ V &= 0 \end{aligned} \tag{2.19}$$

where U_0 is the oscillating amplitude in the case of an irrotational flow.

Looking at a very thin region near the bottom, assuming that the spatial scale of the phenomenon under consideration is much smaller than the spatial scale of the wave, it follows that

$$cos\,(kx - \omega t) = cos\,(kx) \cdot cos\,(\omega t) + sin\,(kx) \cdot sin\,(\omega t) \cong cos\,(\omega t) \tag{2.20}$$

thus being kx very close to zero and, in turn, $cos\,(kx) \cong 1$ and $sin\,(kx) \cong 0$. As a consequence $U = U_0 cos\,(\omega t)$.

However, a contradiction appeared. At the bottom, under the assumption of inviscid, incompressible, heavy fluid, the horizontal component of the velocity U harmonically oscillates. However, both velocity components should be null at the bottom due to the no-slip condition. Moreover, the shear stresses should be null throughout the water depth due to the inviscid fluid assumption, as stated by Newton's equation $\tau = \mu \partial U / \partial n$. Nevertheless, experimental results show that the shear stresses at the bottom are strong due to the considerable velocity gradients. This contradiction can be addressed by defining the so-called boundary layer

where both the viscous stresses induced by the solid bed and the vorticity are significant. Within this region, the assumption of inviscid, irrotational flow has to be removed and the Navier-Stokes equations can not be simplified, thus the Laplace's equation is invalid. Moreover, the velocity in the upper part of the boundary layer, i.e. at $y = \delta$, have to be equal to the velocity in the lower part of the irrotational flow ($U = U_0 cos(\omega t)$), being $\delta << L$ the boundary layer thickness.

$$\begin{aligned}
\rho\left(\frac{\partial U}{\partial t}+U\frac{\partial U}{\partial x}+V\frac{\partial U}{\partial y}\right) &= -\frac{\partial p}{\partial x}+\nu\frac{\partial^2 U}{\partial x^2}+\nu\frac{\partial^2 U}{\partial y^2} \\
\rho\left(\frac{\partial V}{\partial t}+U\frac{\partial V}{\partial x}+V\frac{\partial V}{\partial y}\right) &= -\frac{\partial p}{\partial y}+\nu\frac{\partial^2 V}{\partial x^2}+\nu\frac{\partial^2 V}{\partial y^2} \\
\frac{\partial U}{\partial x}+\frac{\partial V}{\partial y} &= 0 \\
U = V &= 0 \qquad \text{at } y = 0 \\
U &= U_0 cos(\omega t) \qquad \text{at } y = \delta
\end{aligned} \tag{2.21}$$

Imposing that within the boundary layer the magnitude of the local inertial forces is equal to the magnitude of the diffusive terms, the boundary layer thickness can be calculated. Thus, from the equation of motion

$$O\left(\frac{\partial U}{\partial t}\right) \cong O\left(\nu\frac{\partial^2 U}{\partial y^2}\right). \tag{2.22}$$

The variables can be non-dimensionalised, as follows [1]

- $x = x^* \cdot L$
- $y = y^* \cdot \delta$
- $p = p^* \cdot \rho \cdot U_0^2$
- $\tau = \tau^* \cdot \rho \cdot U_0^2$
- $U = u^* \cdot U_0$
- $t = t^* / \omega$

[1] In this section the asterisk denotes a non dimensional variable.

Thus,

$$O(U_0 \cdot \omega) \cong O\left(\frac{\nu \cdot U_0}{\delta^2}\right). \tag{2.23}$$

As a consequence, the boundary layer thickness is proportional to $\sqrt{\nu/\omega}$; conventionally

$$\delta = \sqrt{\frac{2\nu}{\omega}}. \tag{2.24}$$

The magnitude of the vertical component of the velocity can be obtained from the continuity equation

$$V\frac{\partial U}{\partial x} + \frac{\partial V}{\partial y} = 0 \Rightarrow V \cong O\left(\frac{U_0\delta}{L}\right) \tag{2.25}$$

moreover

$$\begin{aligned}
&\frac{\partial U}{\partial x} \cong O(1);\\
&\frac{\partial U}{\partial y} \cong O\left(\frac{1}{\delta}\right);\\
&\frac{\partial V}{\partial x} \cong O(\delta);\\
&\frac{\partial V}{\partial y} \cong O(1);\\
&\frac{\partial p}{\partial x} \cong O(1);\\
&\frac{\partial \tau_{xy}}{\partial x} \cong O(1);\\
&\frac{\partial \tau_{xy}}{\partial y} \cong O\left(\frac{1}{\delta}\right);\ldots
\end{aligned} \tag{2.26}$$

$$\begin{aligned}
&\frac{\partial U}{\partial t} \cong O(1);\\
&\frac{\partial V}{\partial t} \cong O(\delta).
\end{aligned}$$

High order terms can be neglected obtaining

$$\begin{aligned} \rho \cdot \left(\frac{\partial U}{\partial t} + U\frac{\partial U}{\partial x} + V\frac{\partial U}{\partial y} \right) &= -\frac{\partial p}{\partial x} + \frac{\partial \tau_{xy}}{\partial y} \\ \frac{\partial p}{\partial y} &= 0 \\ \frac{\partial U}{\partial x} + \frac{\partial V}{\partial y} &= 0. \end{aligned} \tag{2.27}$$

From the second equation $p = f(x)$. Moreover, by imposing the pressure congruence between the upper part of the inner flow and the lower part of the lower flow

$$\frac{\partial p}{\partial x} = 0 \qquad \text{at } y = \delta. \tag{2.28}$$

Under the assumption that the component velocity along the x direction U is constant, it follow that $\partial U/\partial x = 0$. Moreover, the vertical component of the velocity is null both at the bottom due to the no-slip condition and throughout the whole boundary layer due to the continuity equation $\partial v/\partial y = 0$. As a consequence:

$$\begin{aligned} \frac{\partial U}{\partial t} &= -\frac{1}{\rho}\frac{\partial p}{\partial x} + \frac{1}{\rho}\frac{\partial \tau_{xy}}{\partial y} \\ \frac{\partial p}{\partial y} &= 0. \end{aligned} \tag{2.29}$$

Moreover, being $\tau = 0$ in the outer flow, due to the congruence condition

$$\frac{\partial U}{\partial t} = -\frac{1}{\rho}\frac{\partial p}{\partial x} \qquad \text{at } y = \delta \tag{2.30}$$

thus, the pressure gradient $\partial p/\partial x = 0$ is constant throughout the boundary layer, being $\partial p/\partial y = 0$.

As a consequence the equation of motion become

$$\frac{\partial}{\partial t}(U_0 - U) = -\frac{1}{\rho}\frac{\partial \tau_{xy}}{\partial y} \tag{2.31}$$

from which

$$\tau_{xy} = \rho \int_y^{\delta} \frac{\partial}{\partial t} (U_0 - U)\, dy \tag{2.32}$$

being $\tau_{xy} = 0$ at $y = \delta$. The solution can be particularized for the laminar and turbulent flow by introducing an assumption on the nature of the shear stress τ.

In the case of a laminar flow, these equations can be written as

$$\begin{aligned} \tau &= \rho \nu \frac{\partial U}{\partial y} \\ \frac{\partial}{\partial t}(U_0 - U) &= -\nu \frac{\partial^2 U}{\partial y^2} \\ U &= U_0 cos(\ \omega t) \end{aligned} \tag{2.33}$$

By deriving the differential equation of motion, the Stokes solution can be obtained

$$U = U_0 \left[1 - \exp\left(-(1+i)\frac{y}{\delta}\right)\right] \exp(i\omega t) + \text{c.c.}, \tag{2.34}$$

by which the velocity profiles of the bottom boundary layer can be represented as in Figure 2.4.

Replacing the Stokes expression for the horizontal velocity component within the Newton formula, the shear stress can be calculated

$$\tau(y,t) = \rho \nu U_0 \frac{(1+i)}{\delta} \left[\exp\left(-(1+i)\frac{y}{\delta}\right)\right] \exp(i\omega t) + \text{c.c.} \tag{2.35}$$

which at the bottom is

$$\tau(0,t) = \rho \nu U_0 \frac{\sqrt{2}}{\delta} \left[\exp\left(i\left(\omega t + \frac{\pi}{4}\right)\right)\right] + \text{c.c.}. \tag{2.36}$$

It could be observed that the shear stress at the bottom is out of phase of $\pi/4$ with respect to the velocity in the upper part of the inner flow.

In the case of a turbulent flow, the true analytical solution of the equation of motion cannot be obtained. Indeed, even in the simple case of horizontally uniform flow, the equation of motion includes two variables, i.e. U and τ_{xy}:

$$\frac{\partial}{\partial t}(U - U_0) = \frac{1}{\rho} \frac{\partial \tau_{xy}}{\partial y} \tag{2.37}$$

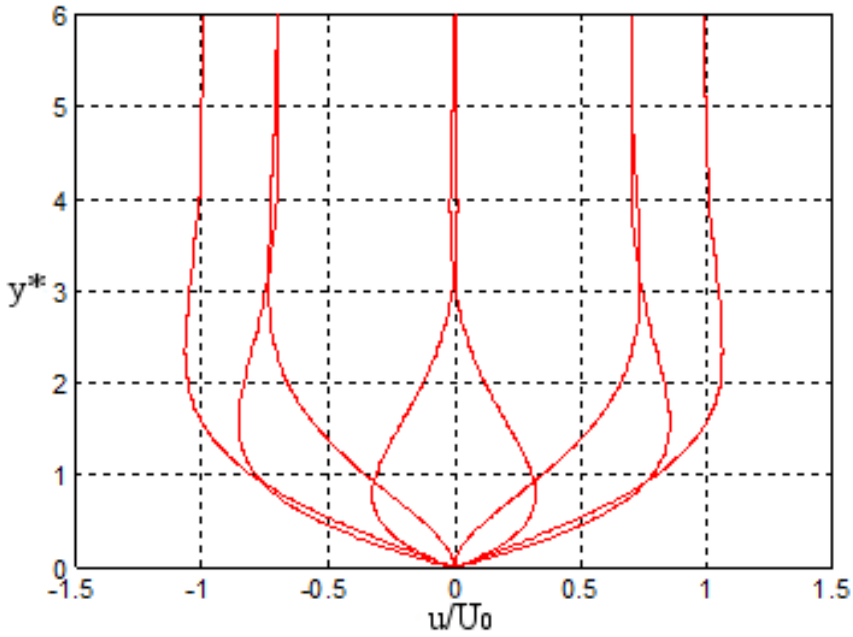

Figure 2.4: Velocity profiles within the Stokes boundary layer in the case of a laminar flow.

Nevertheless, the solution of the Reynolds equation can be obtained through empirical approaches that link the Reynolds stress to the mean velocity. Boussinesq (1877) defined the turbulent viscosity ν_t variable, which depends on the flow field characteristics but, differently from the kinematic viscosity, does not depend on the fluid properties. As a consequence, it is possible to extend the Newton formula to the turbulent flow case. In such case, the shear stress can be expressed as

$$\tau^* = \rho \cdot \nu_t \frac{\partial U}{\partial y}. \tag{2.38}$$

In order to get an analytical solution of the equation of motion, variables can be phase averaged. The velocity field of a flow can be split into a mean part and a fluctuating part using Reynolds decomposition

$$\begin{aligned} U &= \overline{u} + u' \\ V &= \overline{v} + v'. \end{aligned} \tag{2.39}$$

This operation does not influence linear formulae like the continuity equation. Indeed, the period average of a fluctuating component is null by definition. However, the period average of the product of two fluctuating components is not null. Thus, time averaging the equation of motion, several terms which have the dimensions of stresses appear, e.g. $\rho\overline{u'v'}$. These terms are called Reynolds or turbulent stress and by the Boussinesq assumption can be expressed as

$$\overline{u_i'u_j'} = \frac{2}{3}\delta_{ij}k - \nu_t\left(\frac{\partial u_i}{\partial x_j} + \frac{\partial u_j}{\partial x_i}\right) \tag{2.40}$$

being $k = 1/2\overline{u_i'^2}$ the turbulent kinetic energy and δ_{ij} the Kronecker symbol.

This equation can be solved by introducing a model for the turbulent viscosity which depends on both the distance from the bottom and the flow field, thus, in turn on the wave phase. Nevertheless, most models give a turbulent viscosity which does not depend on the time. Time dependence slightly affects the solution and can be neglected. Kajiura (1968) defined three formulae for the turbulent viscosity with respect to the distance from the bed

$$\begin{aligned} \nu_{t1} &= 0.185 \cdot \kappa \cdot u_* \cdot r \qquad 0 \le y \le r/2 \\ \nu_{t2} &= \kappa \cdot u_* \cdot y \qquad\quad r/2 \le y \le d \\ \nu_{t3} &= \kappa \cdot u_* \cdot d \qquad\quad d \le y \end{aligned} \tag{2.41}$$

Where $\kappa = 0.4$ is the von Kármán constant, r is the bottom roughness and d is the boundary layer thickness as defined as

$$d = 0.05 \cdot u_* \frac{1}{\omega}, \tag{2.42}$$

and u_* is the friction velocity

$$\begin{aligned} u_* &= \sqrt{\frac{\tau_0}{\rho}} = U_0\sqrt{\frac{f_w}{2}} \\ \tau_0^* &= \frac{1}{2} f_w \cdot \rho \cdot {U_0}^2 \\ f_w &= f_w\left(Re, r/A\right) \end{aligned} \tag{2.43}$$

During the last decades, several eddy viscosity models were proposed. A sketch of the main mean turbulent viscosity models is reported in Figure 2.5.

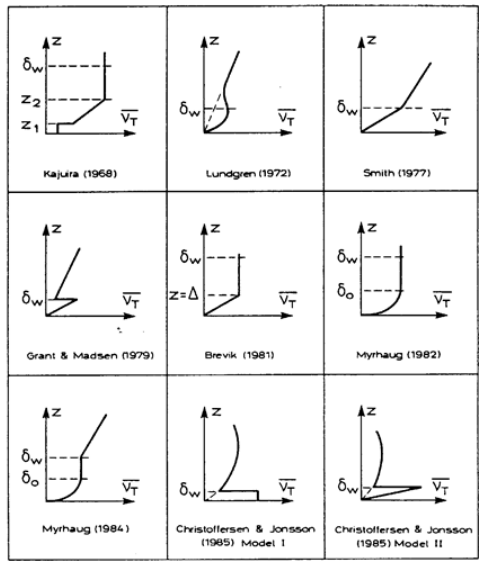

Figure 2.5: Sketch of several time-independent eddy viscosity turbulence models (Deigaard et al., 1992).

In particular, Bakker (1974) proposed a model based on the mixing length $l = \kappa z$, where z is the distance from the theoretical bed. Thus,

$$\tau = \rho l^2 \frac{\partial U}{\partial y} \left| \frac{\partial U}{\partial y} \right| . \tag{2.44}$$

Nevertheless, analytical models should deal with the strong assumptions made, e.g. plane, horizontal and fixed bottom, monochromatic and small amplitude waves. In order to overcome these difficulties, the structure of the turbulent boundary layer was explored by both numerical models and laboratory measurements.

Numerical and experimental studies on the bottom boundary layer Depending on the Reynolds number $Re_\delta = U_0 \delta / \nu$, Vittori and Verzicco (1998) identified four flow regimes in the Stokes boundary layer:

- the laminar regime characterized by unidirectional flow ($Re_\delta < 100$),

- the disturbed laminar regime where appear small flow perturbations ($100 < Re_\delta < 550$),
- the intermittently turbulent regime where perturbations appear only during the decelerating phase of the cycle ($550 < Re_\delta < 3500$),
- the fully developed turbulent regime where turbulence is present throughout the cycle ($Re_\delta > 3500$, see Jensen et al. (1989)).

The oscillatory flow instability was at first examined by Li (1954) for the Stokes layer on smooth and rough plates, by Collins (1963) for the modified Stokes layer induced by progressive surface waves and by Sergeev (1966) for oscillatory pipe flow. Hino et al. (1976) observed the explosive appearance of turbulence bursts towards the end of the accelerating phases of the cycle. Finally, Jensen et al. (1989) found that for $Re_\delta > 3500$ turbulence is present throughout the whole cycle. Only recently these experimental observations found an appropriate theoretical interpretation Blondeaux and Seminara (1979) and Akhavan et al. (1991). In particular, Vittori and Verzicco (1998) delineated the mechanism of transition from the laminar to the intermittently turbulent regime through the disturbed laminar regime in a Stokes boundary layer by means of direct simulations. However, direct numerical simulations of the Stokes boundary layer in the turbulent regime were not carried out as yet, due to prohibitive computational costs as also observed by Costamagna et al. (2003).

Nevertheless, in the ocean the wave-induced bottom boundary layer is generally turbulent, and the ocean bed is generally hydrodynamically rough. Indeed, differently from the steady flow condition, in the oscillating case, the viscous effect (vorticity) associated with the satisfaction of the no-slip condition has only a limited time, of the order half a wave period, to be transmitted (diffuse) away from the boundary layer. As a consequence, the near bed flow is highly rotational and shear stresses associated with the fluid motion cannot be neglected. Thus, several studies were directed toward determining the boundary shear stress and energy dissipation associated with a horizontally uniform, harmonically oscillating fully turbulent flow. Based on laboratory measurements and the analogy to steady turbulent flow, Jonsson (1963, 1967) and Jonsson and Carlsen (1976) developed simple, semi-empirical expressions for the maximum bed shear stress and the boundary layer thickness for this type of flow. Kajiura (1968) elaborated an analytical model by using a time-invariant effective viscosity similar to that proposed by Clauser (1956) for steady turbulent boundary layers. Analytical models similar to that of Kajiura, based on a time-invariant effective viscosity, were proposed by Grant

(1977), Smith (1975), Brevik (1981), Long (1981) and Myrhaug (1982). Similar numerical studies based on Prandtl's mixing-length hypothesis were reported by Johns (1975) and Bakker (1974). All of the above theoretical models reproduce velocity measurements reported by Jonsson (1963, 1967) and Jonsson and Carlsen (1976) reasonably well. Kamphuis (1975) reported an extensive, purely empirical study in which the maximum boundary shear stress in a turbulent oscillatory flow was measured directly. Subsequent discussions by Grant (1975) and Jonsson (1976) indicate that the above semi-empirical, theoretical, and purely empirical studies give essentially the same maximum bed shear stress over a wide range of bed and flow conditions. The maximum bed shear stress can therefore be predicted with confidence by using relatively simple expressions based on concepts borrowed from steady turbulent flow.

Lavelle and Mofjeld (1983) reported a theoretical study of a oscillatory uniform turbulent channel flow. Similarly, Trowbridge and Madsen (1984a) carried out an experimental study near a fixed, hydrodynamically rough bed with roughness elements small in comparison to the excursion amplitude of the fluid motion. It found that third and higher harmonics are present in the velocity and stress fields in an oscillatory turbulent boundary layer and that this feature is predicted by a linear model only if the eddy viscosity varies in time.

Finally, equilibrium as well as non-equilibrium turbulent flows were accurately simulated by means of large-eddy simulations (Sarghini et al., 1999; Wu and Squires, 1998; Henn and Sykes, 1999; Falcomer et al., 2001; Salon et al., 2007). Moreover large-eddy simulations, used in conjunction with dynamic subgrid-scale models, could simulate correctly flow fields characterized by sharp transition to turbulence and local re-laminarization (see for example Germano et al., 1990; Meneveau et al., 1996; Armenio and Sarkar, 2002).

2.1.7 The ripple covered bed case

The flow over a ripple-covered bed differs considerably from the flow over a uniform roughness bed. Indeed, the relatively large and regular roughness produces the entrainment into the main body of the water of regular, large-size vortices at certain locations, at specific flow phases.

The problem of separating oscillatory flow near a bed with large fixed ripples was treated numerically by Longuet-Higgins (1981), who used a "discrete vortex" method, and by Sleath (1982), who solved the 2-D Navier-Stokes equations and averaged the results over a number of wave periods large enough to give a stable

solution. Both methods reproduce reasonably accurately the laboratory measurements of energy dissipation reported by Bagnold (1946). Grant and Madsen (1979) presented a semi-empirical analysis of the potentially important effect of a movable bed on a turbulent, oscillatory flow and obtained favourable agreement with the limited laboratory data of Carstens et al. (1969). The analysis is also supported by the field measurements reported by Grant et al. (1983).

More recently, Fredsøe et al. (1999) proposed the velocity logarithmic distribution to be expressed as

$$\frac{U}{u_*} = \frac{1}{\kappa}\ln\left(\frac{30(y-\Delta y)}{k_s}\right) \tag{2.45}$$

where the so-called displacement thickness Δy from the ripple crest takes into account the shift of the theoretical bed origin in case of a rippled bottom (Figure 2.6).

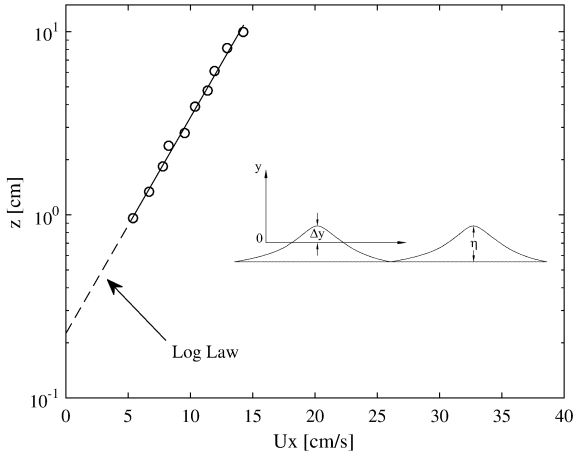

(a)

Figure 2.6: Logarithmic law in dimensional coordinates (phase-averaged velocities vs the distance from the theoretical bed) (Fredsøe et al., 1999).

Moreover, the hydraulic roughness of a cohesive bottom can be recover in an indirect way, i.e. analysing the velocity profile inside the so-called logarithmic layer. Indeed, the friction velocity is the log law slope, whereas the intercept value is equal to the aforementioned $y_0 = k_s/30$. Data reported in literature point out that

$k_s \cong (2-4)\eta$ Bayazit (see, for example 1983); Kamphuis (see, for example 1974) and $\Delta y \cong 0.25\eta$ (Fredsøe et al., 1999; Bayazit, 1976, 1983); being η the ripple height.

2.2 Mass transport

Each fluid particle of a water wave describes an elliptic path moving in the direction of wave propagation at the upper part of the orbit and in the opposite direction at the bottom of the orbit. Due to the non-linear effects, such a path is not precisely closed. Indeed, the forward velocity in the upper orbit is larger than the backward velocity in the lower one.

Therefore, a second-order drift velocity $\overline{U}$ in the direction of wave propagation superimposes to the orbital motion, which is named mass transport velocity. This velocity was determined by Stokes (1847), under the hypothesis of irrotational motion. In particular, assuming that the total horizontal transport is zero, the Stokes's equation for the mass transport velocity is equivalent to

$$\overline{U} = \frac{H^2 \omega k \cosh 2k(z-h)}{2\sinh^2 kh} - \frac{H^2 \omega}{2h} \coth kh, \tag{2.46}$$

where h is the depth, H is the wave height, $k = 2\pi/L$, L is the wave length, $\omega = 2\pi/T$ and T is the wave period.

The Figure 2.7 shows that, at intermediate depth region, the mass transport velocity is offshore directed at the bottom and onshore directed at the surface. Moreover, the mass transport velocity gradient at the bottom is equal to zero. The reference system (x, z) is also indicated.

The offshore directed mass transport is also called "undertow".

2.2.1 Undertow

Consider a regular wave that is propagating in the nearshore zone in a steady situation. Due to the interaction with the bottom, the wave changes its height. At the beginning of the shoaling zone wave height decreases, then at a certain depth, it starts increasing as long as it becomes unstable and breaks. Such a process is highly dissipative due to the turbulence and work against bottom friction.

Therefore, within the surf zone, an onshore directed flow appears due to two mechanisms: the wave drift and the surface rollers carrying water forward in the direction of wave propagation. In a three-dimensional situation, this onshore flux

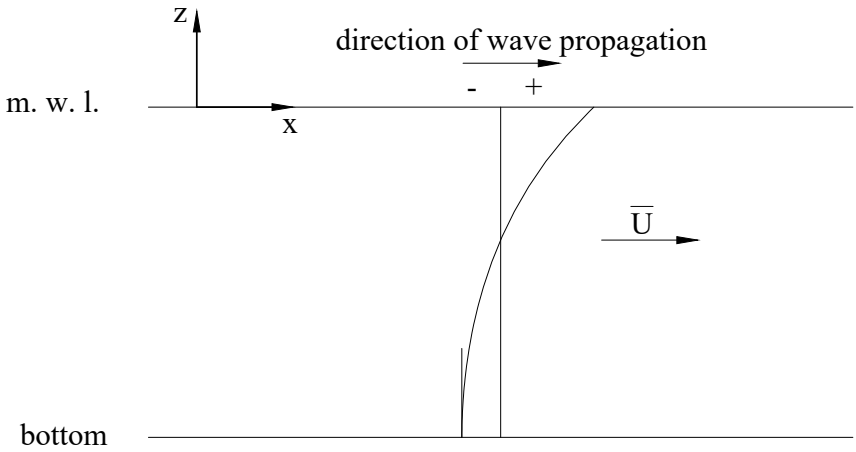

Figure 2.7: Mass transport velocity outside of the breaking zone in a progressive irrotational wave ($kh = 1$).

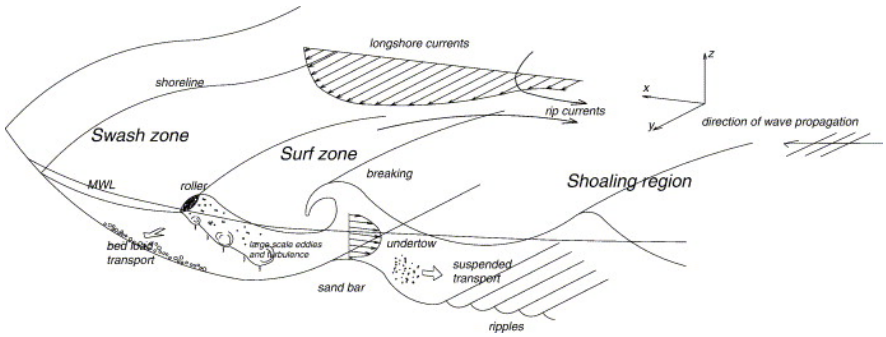

(a)

Figure 2.8: Sketch of the complex surf zone hydrodynamics which typically occurs on gentle sloping beaches (Musumeci et al., 2005).

is often balanced by the rip currents whereas in a strictly two-dimensional situation this role is played by a (strong) seaward current that appears close to the bottom and is called undertow. Such a return current has its maximum in the proximity of the bed whereas the shoreward current together with rollers and wave drift lies near the mean water surface.

Outside of the surf zone, the undertow does not occur because surface rollers do not exist and the friction energy dissipation is confined to the bottom boundary layer.

2.2.2 Longuet-Higgins steady streaming

According to Longuet-Higgins (1953), mass transport velocities measured in the laboratory may sensibly differ from those calculated with the irrotational theory, particularly in water of moderate depth. Indeed, contrary to the Stokes (1847) prediction, Bagnold (1947) measured a strong positive, i.e. onshore directed, velocity near the bottom and a weak negative velocity outside the boundary layer, whereas, both Caligny (1878) and King (1948) found the backward drift in the free stream balanced by the forward velocity measured both near the bottom and near the free surface, see Figure 2.9.

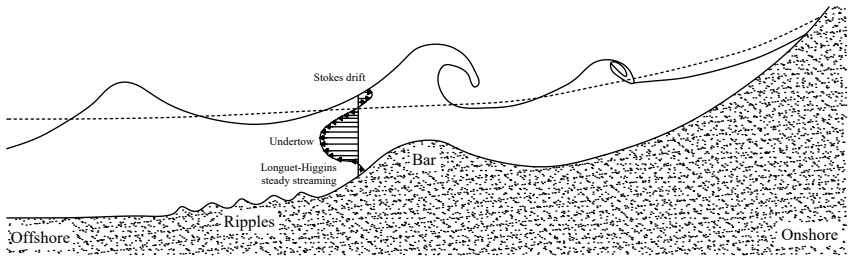

(a)

Figure 2.9: Sketch of the Longuet-Higgins steady streaming together with the Stokes drift in a typical coastal environment.

The disagreement between the Stokes (1847) irrotational theory and the experimental results is due to the considerable vorticity lying within the bottom boundary layer as a result of the boundary layer velocity gradient. Indeed, because of the no-slip condition, a thin layer of viscous fluid is at rest on the bottom, whereas it reaches velocities comparable those measured within the free stream just few millimetres above. Thus, a strong velocity gradient implies a strong vorticity in the

neighbourhood of the bottom which total amount is finite, although it is confined to a layer of small thickness.

Removing the irrotational ideal-fluid hypothesis Longuet-Higgins (1953) realized that in an oscillating motion this vorticity is of alternating sign and it is carried out by convections and viscous diffusion to spread into the interior of the fluid in a layer thicker than the oscillating boundary layer (Batchelor, 2000). Within such a layer, the horizontal and vertical velocities are not exactly $\pi/2$ out of phase which gives rise to a non-zero time-averaged near-bed Eulerian drift (see Holmedal and Myrhaug, 2009; Lwin et al., 2012). Similarly, an onshore flux appears near the free surface. Such a boundary layer drift in the direction of propagation induced by progressive waves is usually called Longuet-Higgins steady streaming. Although such a second-order mean velocity is weak compared with the oscillating component triggered by the surface gravity waves, it plays an important role both in transport processes (Petrotta et al., 2018) and engineering projects which require knowledge of currents present in the sea, like the dumping of pollutants or the design of the offshore structure foundations of offshore structures (Liu, 1977) .

2.2.3 Asymmetry-wave steady streaming

The linear theory gives the best overall agreement with data for flat and sloping beds (slopes between 1:100 and 1:4.45) up to the breaking point and within the surf-zone. Indeed, due to asymmetries, velocities under the trough are overestimated by a factor that reaches 1.5 to 2 near the breaking point and then decreases in the surf zone (Soulsby et al., 1993; Hattori, 1987; Nadaoka and Kondoh, 1982).

Stokes higher order models can predict such velocity asymmetries only in intermediate water depths, when vertical asymmetries are weak. In particular, within a turbulent boundary layer, the mass-transport velocity can be considerably different from that predicted by Longuet-Higgins (1953). Indeed, Brebner et al. (1967); Bijker et al. (1974); van Doorn (1981) measured a steady streaming velocity at the edge of a turbulent boundary layer smaller than the value determined by Longuet-Higgins (1958). Moreover, Trowbridge and Madsen (1984b) found that when the boundary layer is subjected to asymmetric forcing, the steady streaming velocity can be against the direction of wave propagation for very long waves; Deigaard et al. (1999) found similar results for long bound waves. Negative steady streaming velocities are also found in oscillating bottom boundary layers subjected to horizontally uniform forcing by Ribberink and Al-Salem (1995), Davies and Li

(1997) and Holmedal and Myrhaug (2006), in case of a rough bottom. In some shallow depth experiments, (Petrotta et al., 2018) measured an offshore directed steady streaming.

The characteristics of the steady streaming generated within the turbulent wave boundary layer over a infinite smooth plate was examined by Scandura (2007) by means of numerical simulations of the Navier–Stokes equations. He found that the different characteristics of turbulence during the seaward and landward asymmetric wave half-cycles trigger the appearance of the measured backward flow.

Holmedal and Myrhaug (2009) deeply analysed the two mechanisms which cause streaming, i.e. the wave asymmetry (asymmetry of turbulent fluctuations in successive wave half-cycles) and the presence of a small vertical wave velocity in the boundary layer (Longuet-Higgins streaming). More in detail, they performed numerical simulations of the seabed boundary layer beneath both sinusoidal waves and Stokes second order waves, as well as horizontally uniform bottom boundary layers with asymmetric forcing. The interaction between these two mechanisms depends on the degree of wave asymmetry and how long the waves are compared to the water depth. The Longuet-Higgins streaming decreases as the wave length increases for a given water depth, and the effect of wave asymmetry can dominate, leading to a steady streaming against the wave propagation. The streaming velocities beneath sinusoidal waves (Longuet-Higgins streaming) is always in the direction of wave propagation, while the streaming velocities in horizontally uniform boundary layers with asymmetric forcing are always negative. They found that the effect of asymmetry in second order Stokes waves is either to reduce the streaming velocity in the direction of wave propagation, or, for long waves relative to the water depth, to induce a streaming velocity against the direction of wave propagation. The asymmetry of second order Stokes waves reduces the mass transport (wave-averaged Lagrangian velocity); for a fixed water depth this mass transport can become almost zero for sufficiently long waves and large enough wave asymmetry. Moreover, an increase in the bottom roughness leads to an increase in the boundary layer thickness, the maximum steady streaming velocity, and mass transport velocity within the boundary layer. The steady streaming velocity and mass transport velocity at the edge of the boundary layer do not seem to vary much with the bottom roughness. Furthermore, the boundary layer streaming leads to a wave-averaged transport of suspended sediments and bedload in the direction of wave propagation. The Longuet-Higgins streaming is the dominating mechanism acting on the sediments, and thus the total sediment transport is not

very different beneath sinusoidal waves and second order Stokes waves. This is the case except for fine sediments, where the total sediment transport is dominated by suspension, i.e. the larger streaming velocity beneath symmetric waves results in larger suspended sediment transport beneath sinusoidal waves than beneath second order Stokes waves.

Nevertheless, such an asymmetry wave steady streaming was much less studied in literature than the Longuet-Higgins steady streaming in terms of a mathematical problem, probably because of the complexity of the analytical solution. However, asymmetric waves free from the Longuet-Higgins steady streaming cannot normally be produced in a laboratory (Scandura, 2007). Nevertheless, the effects of the wave asymmetry can be analysed within an oscillating water tunnel, generating a spatially uniform oscillating boundary layer free from the Longuet-Higgins steady streaming, (Ribberink and Al-Salem, 1995). However, they mainly focussed on the study of sediment transport under sheet flow conditions and very few results were provided about the steady streaming induced by the wave asymmetry.

At a later time, Scandura et al. (2016) investigated the hydrodynamics of wall-bounded acceleration-skewed oscillatory flows by means of numerical integration of the Navier–Stokes equations. They found that even though the flow is not velocity skewed in the irrotational region, it becomes velocity skewed in the boundary layer, causing an asymmetry between the peaks of the wall shear stress in the two half-cycles. Such an asymmetry increases with acceleration skewness while an increase of Reynolds number from the laminar regime causes the asymmetry first to decrease and then increase.

2.2.4 Ripple formation

Waves propagating over a non-cohesive bed may give rise to the appearance of small-scale bedforms known as ripples. The presence of such small amplitude bottom undulation generates steady streamings which consist of recirculating cells (see Figure 2.10a) the form, intensity and direction of which depend on the characteristics of the wave and of the perturbation (Sleath, 1984). At this stage ripples belong to the so-called rolling-grain stage.

Because the sediment is driven by the fluid, if the steady drift in the vicinity of the bed is directed from the troughs towards the crests of the perturbation and is strong enough to drag the sediments, they tend to move from the troughs towards the crests. The tendency of sediments to pile up near the crests is opposed

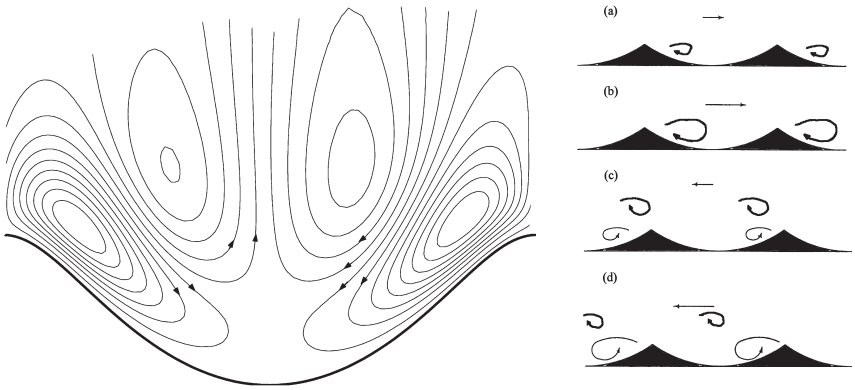

Figure 2.10: Vorticity over a rippled bed: (a) sketch of the double structure of steady streaming recirculation cells; (b) schematic sequence of vortex shedding over a rippled bed (Ourmieres and Chaplin, 2004).

by the component of the gravity force acting in the down-slope direction. It follows that the growth of the amplitude of the bottom waviness is controlled by a balance between these two effects. If gravity prevails over drag, the amplitude decays, otherwise, it grows leading to the appearance of ripples (Blondeaux, 1990). Moreover, Sleath (1991) argued that the effect is stronger for ripple wavelengths of the same order of magnitude as the amplitude of the fluid displacement oscillations since in this case particle settling locations will tend, after several cycles, to the nearest ripple crest. Once formed, ripples do not continue to grow indefinitely because the steady streaming is modified by non-linear effects and, as the ripples get steeper, an equilibrium configuration is attained.

Thus, sediments are trapped in vortex structures which are generated by flow separation at the ripple crests. When flow reverses and the vortex structures are no longer reinforced but simply convected by the local velocity, sediment is carried in suspension far from the point where it was picked up and then is slowly released when vortices decay because of viscous effects (Nielsen, 1979; Sunamura, 1980).

Blondeaux and Vittori (1991) analysed the vorticity dynamics over a rippled bed, showing that: (i) whenever a vortex structure moves towards the bottom, a secondary vortex is generated near the ripple profile, which interacts with the

primary vortex and causes it to move away from the bottom (see Figure 2.10b); (ii) depending on the values of the parameters, the time development of the free shear layer shed from the ripple crest may produce two or even more vortex structures; (iii) occasionally vortices generated previously may coalesce with the free shear layer shed from the ripple crest, generating a unique vortex structure.

More recently, Scandura et al. (2000) studied the growth of vortices above ripples by means of direct numerical simulations at low Reynolds numbers. They found that for a fluid displacement comparable to the ripple wavelength, both flow separation and the presence of a free shear layer can destabilize the two-dimensional flow. Malarkey and Davies (2012) described two discrete vortex models for oscillatory flows over ripples, a non-viscous model with no diffusion of vorticity and a cloud-in-cell model with good results in terms of vortex behaviour for cases with wave orbital amplitudes of the same order as the ripple wavelength.

In presence of an asymmetrical flow, Van der Werf et al. (2007) experienced that the vortex formation on the lee slope (onshore flank) during onshore flow is much stronger than on the stoss slope (offshore flank) during offshore flow, because maximum onshore velocity is larger than maximum offshore velocity (see Figure 2.11).

Named T the wave period, λ the ripple wavelength, η the ripple height, U_∞ the freestream velocity, Van der Werf et al. (2007) found that near-ripple flow reversal occurs at 0–0.3 T, before the free-stream flow reversal due to the vortex formation. Moreover, near the ripple crest, velocities can be up to 1.7 times higher than the freestream velocity U_∞ because of flow acceleration over the crest and vortex ejection. Thus, asymmetry in the free stream and the consequent asymmetry in vortex formation produces steady circulation cells with dominant offshore mean flow up the ripple lee slope and in a layer with a thickness of 1–1.5 η. This offshore mean flow is balanced by weaker onshore streaming up the ripple stoss slope and higher up in the flow. The time- and bed-averaged horizontal velocity profile, which is important for determining current-related sand transport, comprises an offshore near-bed streaming (within the ripple troughs) and an onshore drift over ripple crests. Although the magnitudes of the net velocities are small, they considerably affect net sand transport because of the high sand concentrations within the near-bed layer. In such a circumstance, ripples become asymmetrical, i.e. with the offshore slope steeper than the onshore slope.

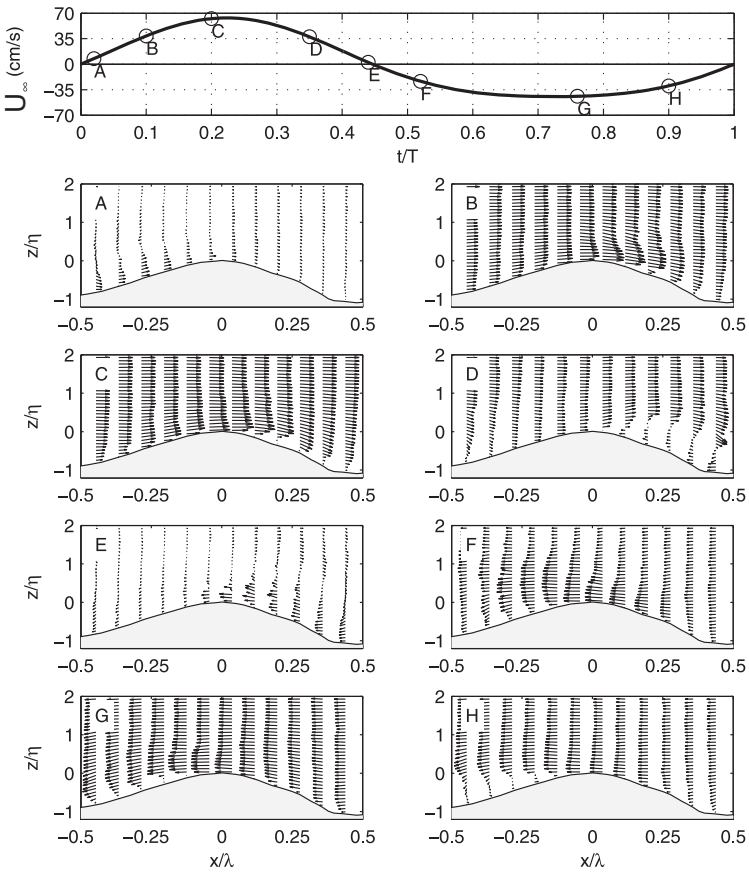

(a)

Figure 2.11: Velocity field for $z < 2\eta$ at eight phases. (top) Free-stream orbital velocity U_∞. The circles on the time series of U_∞ denote the phase of the flow. Positive, "onshore" flow is to the right in the velocity field plots (Van der Werf et al., 2007).

2.3 Hydrodynamics in the surf zone

Within the shoaling region, water waves change their wave heights becoming skewed and asymmetrical, i.e. with high short-duration crests and long-duration flat troughs. With increasing asymmetry, also the steepness of the wave front increases, eventually leading to wave breaking. The region of breaking waves defines the surf zone. Several researchers studied the hydrodynamic processes in the surf zone and the scientific results achieved until the 1980's were summarized by Peregrine (1983); Battjes (1988). Nevertheless, the surf zone is still subject to important deficiencies in terms of understanding for a number of reasons. In particular, wave breaking, which involves the sudden generation of vorticity and turbulence spanning over a wide range of spatial- and temporal scales, is still poorly understood. Furthermore, the strong unsteadiness and spatial variability of the flow field generated within the surf zone makes it generally difficult to collect experimental data with appropriate temporal and spatial resolutions.

Nadaoka and Kondoh (1982) carried out one of the first experiments involving detailed velocity measurements in the surf zone using a laser Doppler velocimeter (LDV). No correlation was found between the strong turbulence near the bed and the wave phase. Such a result, in their opinion, occurs because the turbulence generated by wave breaking was transported down to the bottom. At a later time, Okayasu et al. (1987) measured velocities under plunging waves by using a hot film probe and an LDV. They deduced the existence of a large-scale vortex near the bed, just after plunging, and noted that the oscillating component of the velocity must contain an important rotational part.

Nadaoka et al. (1989) found that some vortex structures referred to as 'horizontal eddies' and 'obliquely descending eddies' which, according to the authors, have a crucial role in the generation of the Reynolds stress and in entraining and re-suspending sediments. Ting and Kirby (1994, 1995) measured both velocity and turbulence in the surf zone by means of LDV, reporting that:

- under plunging breakers the turbulent kinetic energy *tke* is transported landward and dissipates within one wave cycle, whereas, under spilling breakers the *tke*, which dissipates much slower, is carried seaward by the mean flow;

- in the bore region of a plunging breaker the velocity is slightly higher under the crest compared to the trough, but the turbulence is much higher under the crest,

so on average turbulence is transported onshore; instead, the temporal variation of turbulence under spilling breakers is relatively small, but the offshore-directed velocities are of higher magnitude and longer duration, so the net transport is offshore directed.

Ting and Kirby (1996) identified that turbulent transport processes under spilling breakers are similar in the outer and inner surf zones and turbulent diffusion is the primary mechanism for transport while advection becomes noteworthy mainly near the surface.

From field measurements Ruessink (2010) showed that in the surf zone the Reynolds shear stress, which involves the correlation between the cross-shore and the vertical turbulent velocity fluctuations has the opposite sign to that of a boundary layer generated Reynolds stress. This result was explained by the presence of breaking induced vortices similar to those discussed by Nadaoka et al. (1989). Govender et al. (2002) highlighted that the region of highest turbulence production is located in the front part of the wave crest, close to the roller. Near the free surface turbulence has a clear phase dependence but this does not occur near the bed. Further contributions to the understanding of turbulence dynamics under breaking waves were provided by numerous studies such as Cox and Kobayashi (2000); De Serio and Mossa (2006); Huang et al. (2009); Sumer et al. (2013), which also highlighted the differences between spilling and plunging breakers in terms of turbulence dynamics.

All the studies described above, except the field measurements of Ruessink (2010), were based on experiments involving breaking waves over a plane sloping beach. The case of a barred beach is more interesting since it frequently appears in nature, thus it provides an improved understanding of the hydrodynamics over real beaches.

Smith and Kraus (1991) showed that the macroscopic features of waves breaking over plane and barred beaches are substantially different. Scott et al. (2005) carried out experiments in a large-scale wave flume involving waves breaking on an artificial barred beach which reproduced one of the profiles detected during the DUCK1994 field experiments. In these experiments breaking wave turbulence was maximum at the bar crest. Onshore from the crest, turbulence was mainly confined to the free-surface. Yoon and Cox (2010) performed velocity measurements in a large-scale wave flume over an evolving sandy beach which developed a bar. The authors observed that for an equilibrium beach state, mean turbulent kinetic energy and dissipation at the bar trough were smaller than those in the surf zone. Govender et al. (2011) measured the velocity field produced by plunging waves

over a barred beach by means of a video-based digital correlation velocimeter. After plunging near the bar crest the waves transformed into a spilling breaker with turbulence confined in the upper part of the water column. Compared to spilling breakers on a plane beach the turbulence transfer towards the bed was significantly reduced.

Brinkkemper et al. (2017) studied the vertical structure of the turbulence in the surf and swash zones. In the surf zone they observed high turbulence levels during the phase at which the plunging jet hits the water surface. The process by which turbulence generated by wave breaking affects the boundary layer was studied by van der Zanden et al. (2016) who performed velocity measurements in the CIEM large-scale wave flume under plunging breaking waves propagating over a sandy, barred bed profile. In these experiments turbulence in the boundary layer showed peaks at two phases of the wave cycle: the first time when the wave plunges and the second time during the trough phase when turbulence is advected offshore by the wave and undertow velocities. Recently, Van Der A et al. (2017a) discussed measurements carried out in the same wave flume and with the same experimental conditions considered in van der Zanden et al. (2016), except that the bed which was fixed by applying a layer of concrete. High values of the mean turbulent kinetic energy were observed on the onshore side of the bar where the jet penetrates into the water column. A strong upward advection of turbulent kinetic energy was also observed due to the undertow. Measurements during the same experiment were used in Van Der Zanden et al. (2018) to systematically explore the turbulent kinetic energy budget near the bed at 12 cross-shore locations. The analysis showed that production, dissipation, and advection were the primary terms driving the spatial and temporal variation in turbulent kinetic energy. Turbulence production rates near the bed are much higher in the breaking region than in the shoaling zone, due to the strongly non-uniform flow across the bar in combination with the presence of large-scale breaking-generated vortices.

2.4 Wave-current interaction

Waves approaching the coast at an oblique angle of attack give rise to a current which, generally, induces non-linear modifications of phase speed and wavelength, a change in the structure of the bottom boundary layer, and, in turn, a consequent modification of the friction factors and bed shear stresses (Jonsson, 1966), with impacts on the longshore sediment transport (Bijker, 1969).

Surface waves of 5-15 s start to feel the influence of the bottom in approximately 20-180 m of water, respectively. As these waves approach shallower water, the associated values of the near-bottom orbital velocities are of the same magnitude as those of the stronger coastal currents expected. However, the boundary shear stress associated with the wave motion may be an order of magnitude larger than the shear stress associated with a current of comparable magnitude. Intuitively, this is easily pictured by considering the small scale of the wave boundary layer relative to that of the current boundary layer and comparing the respective vertical velocity gradients. Since the entrainment of sediment under flat-bed conditions can be related to the instantaneous shear stress, thus waves are capable of entraining significant amounts of sediment from the seabed when a current of comparable magnitude may be too weak even to initiate sediment motion. On the other hand, waves are an inefficient transporting mechanism, and to the first order, no net transport is associated with the wave motion over a wave period. However, the simultaneous presence of even a weak current will cause a net transport.

Therefore, conceptualizing and over-simplifying the process, waves acting as a stirring mechanism making sediment available for transport by a weak current. Indeed, in the immediate vicinity of the seabed, the wave and current motions cannot be treated separately and then superposed. Rather, there is a non-linear interaction between the two flows as a result of the presence of the bottom boundary. The fluid dynamics of the respective wave and current motions are altered from that expected for a pure wave motion or pure current because of the combined presence of each.

Although in near-shore zones waves and currents interact at a certain angle, for the sake of clarity, the interaction between co-directional and orthogonal wave and currents and their effects on both rough and rippled bed are examined separately.

2.4.1 Co-directional wave and currents

A theory for the combined interaction between waves and currents and its consequences on the sediment transport was developed by Smith (1975) for the co-directional flow case. Similarly, Grant and Madsen (1979) presented an analytical theory on the bottom friction under combined waves and currents at an arbitrary angle in the presence of a rough bottom. In particular, the latest predicted an increase in apparent bed roughness and shear stress when waves are superimposed on a current. However, authors did not validate these results with experimental data.

A similar theory was presented by Christoffersen (1980), using a modified eddy-viscosity distribution. Bakker and Van Doorn (1978) also found an increased apparent bed roughness for waves and currents combined. Changes in mean velocity profile were measured by Brevik and Bjørn (1979) and by Van Hoften and Karaki (1977), although near-bed velocities were not measured in either case. The results of Brevik and Bjørn (1979) indicate an overall reduction in mean velocity over depth when waves are superimposed on the current, although their outer flow measurements were not reliable. George and Sleath (1979) measured the flow over an oscillated bed of spheres with a weak current superimposed, and described the cycle of vortex formation and ejection around the roughness elements. The stronger downstream vortex was found to induce a weak reverse mean current just above the roughness elements. This is consistent with the observations of Inman and Bowen (1962) and Bijker et al. (1976), who both reported enhanced upstream sediment transport when a weak current was superimposed on waves. The latter paper also observes that insight into the vortex formation as a function of wave and flow parameters is essential for an understanding of sand transport by waves and currents.

Over smooth boundaries, Binder and Favre-Marinet (1979) have reported a delay in phase of wave-induced velocities near the bed, when currents are imposed on a pulsed duct flow, contrary to the phase advance that occurs for waves alone.

More recently, Kemp and Simons (1982) carried out an experimental investigation of the interaction between gravity waves and a turbulent current over rough and smooth beds. Superimposing waves propagating with a current they experienced that:

(a) the thickness of both the unidirectional turbulent boundary layer and sidewall boundary layers decreases over both rough and smooth beds leading to a redistribution of flow across the channel;

(b) a return (against the current) flow appears which decreased with increasing wave height H. This decrease was a consequence of the increased part of the wave cycle during which the flow above the bed was against the current. The duration of this reverse flow increases with H, thus allowing the formation of "upstream" vortices, which induce downstream velocities;

(c) mean velocities near the smooth bed increase, whereas near the rough bed they reduce due to a change in the vortex pattern formed between bed roughness elements;

(d) the logarithmic portion of the mean velocity profiles over the rough boundary indicated an increase in mean bed shear stress $\overline{\tau}$ and roughness length scale y_0 with wave height. For the larger waves tested, $\overline{\tau}$ and y_0 were approximately double of their values for current alone;

(e) over the smooth boundary, maximum horizontal turbulence intensity during the cycle, for combined wave and current tests, was 20% higher than for the current alone;

(f) within 2 roughness heights of the rough bed, the turbulence characteristics were dominated by the periodic formation of vortices at the bed. Maximum turbulence intensities and Reynolds stresses measured in the combined flow were up to three times their values for current alone, and they vary by over 50% of their mean values during a wave cycle;

(g) for the range of waves tested, turbulence parameters near the rough boundary increased more rapidly with wave height for tests on waves alone than for waves propagating on a following current.

Propagating waves against a current, Kemp and Simons (1983) found that far from the bed, mean velocities depend on the direction of wave propagation whereas near the bed, the relative directions of flow do not influence the wave-current interaction; in particular near a rough bed, mean velocities decrease by the presence of waves. Huang and Mei (2003) developed an analytical boundary layer theory to predict the wave effects on a turbulent current over a smooth or rough bed, finding that a wave following a current experiences a speed increase, while a wave opposing a current a decrease, and Guizien et al. (2003) proposed a 1DV k-ω turbulence closure model under adverse pressure gradient to predict sediment transport and concentration distribution.

Finally, Lodahl et al. (1998) analysing the flow generated by wave plus current over a rough bed in an oscillating tunnel, found that the shear stresses are strongly influenced by the ratio between the current velocity U_c and the wave orbital velocity U_0. If $U_c/U_0 > 1$ the flow is current-dominated whereas if $U_c/U_0 < 1$ the flow is wave-dominated. In a current-dominated flow, a linear interaction can occur between wave and current components; the wave boundary layer is laminar and stress remain constant. In a wave-dominated flow, if the oscillatory flow is laminar, shear stresses decrease; whereas if the wave boundary layer is turbulent, shear stresses increase.

Rippled beds Differently from a rough bed, the presence of relatively large and regular roughness elements produces in a ripple bed the entrainment into the main body of the water of regular, large-size vortices, in an organized fashion, both in space and in time.

Aydin (1987) conducted experiments in an air tunnel with asymmetric ripples in the case of a combined oscillatory flow and current, measuring the mean and turbulence at several stations over the length of the ripple. He also carried out a numerical simulation of the flow, using a discrete vortex model, and the $\kappa - \varepsilon$ model. Above a rippled bed, Kemp and Simons (1982) experienced that the shear stresses does not increase considerably due to the current superimposition, instead, the vortex dominated layer thickness grows from 4 to 6-7 roughness heights above the bed, (see also Tunstall and Inman, 1975). Thus, more sediments are picked up from the bed and diffused over the zone of the current-induced turbulence; this can result in significantly higher transport rates as long as the increased bed shear stress is not such as to prevent the formation of high bed ripples. Recently, Mathisen and Madsen (1996, 1997) conducted experiments in a wave tank with triangular bars as roughness elements. The height and spacing of these elements were chosen such that the bars simulated the ripples experienced in their movable-bed experiments. Their study essentially focuses on Nikuradse's equivalent sand roughness in the case of the combined flow. Thus, fixed ripples might have a different friction than "live" sand ripples. Morphological calculations with live ripples were performed by Andersen (1999), who found that the friction over live ripples, fixed asymmetric ripples and fixed symmetric ripples were similar.

Finally, Fredsøe et al. (1999) summarized the effects of superimposing waves on a co-linear current over a fixed rippled bed in few points:

1. the entire velocity profile is displaced to a higher elevation;

2. the semi-log graph of the mean velocities shows two "logarithmic layers", one related to the actual roughness produced by the ripple crests height, and the other to the higher apparent roughness induced by the wave motion;

3. the near-bed turbulence level increases due to the lee-wake vortex washing over the ripple crest before the near bottom flow reversal. Such an occurrence was measured both during only wave and wave plus current flow;

4. the ratio between the wave plus current friction factor and the steady current friction factor f_c/f_{c0} is a function of the ratio between the horizontal

component of the mean current velocity at the ripple crest section and the maximum horizontal orbital velocity at the bed U_c/U_m.

2.4.2 Wave and currents at a right angle

The interaction of waves and current at a right angle over a rough bed was examined by Visser (1986) which experienced that wave superimposition produces mean velocities higher than those measured in case of current only. Sleath (1991) through an oscillating plate inside a flume, observed negligible effects of the plate oscillation on the velocity profiles. Simons et al. (1993, 1995, 1997) found that, over a rough bed, waves affect the hydrodynamics generated by currents, significantly reducing the averaged velocities in the upper part of the water depth and often increasing the near-bed mean velocities. Instead, measuring the bed shear stress in a wave plus current environment over a smooth boundary, Arnskov et al. (1993) found that the maximum shear stress does not sensibly increase in the presence of the current.

Musumeci et al. (2005, 2006) found that if the bottom roughness is small enough to produce a laminar boundary layer, waves increase near-bed current velocities. Whereas if bottom roughness is high enough to produce a turbulent boundary layer, waves decrease the near-bed current velocity. Similarly, Lim and Madsen (2016) measured an increase in terms of near-bed roughness when orthogonal waves are superimposed to a current above a bed covered by ceramic marbles ($d_{50} = 12.5$ mm) and a reduction above a smooth bed. These results are in good agreement with the non-linear wave-current boundary layer model proposed by Grant and Madsen (1979, 1986).

Numerical models have to deal with difficulties in coupling waves and currents in a three-dimensional domain with a sandy bed evolving with time-scales very different from the hydrodynamic ones. Thus, not many studies concern the waves plus current flow at a right angle except Myrhaug et al. (2001) which analyses the bottom friction on the direction of maximum bed shear stress using a parametric representation based on experimental data (Simons et al., 1997).

Rippled beds The combined steady and oscillatory flows at a right angle over concrete ripples was studied by Ranasoma and Sleath (1994) which performed an experimental campaign aimed to measure the flow hydrodynamics. Khelifa and Ouellet (2000) proposed empirical relations to predict ripple geometry focusing on the reaction of a sandy bed to waves and currents.

Andersen and Faraci (2003) carried out an experimental investigation of ripple geometry in a combined wave plus current at a right angle flow, in order to find the conditions for regular ripple formation. Ripple crests appeared as straight lines if the current velocity was 20-60% of the wave orbital velocity. They also carried out numerical simulations changing the direction between the waves and the current from 0° to 90°, whose main results are summarized below.

(a) In the presence of both waves and currents close to the rippled bed, the wave effects dominate over the current, enhancing the bottom roughness.

(b) The roughness that was found from Nikuradse's formula predicts the roughness of the flow quite well.

(c) Close to the bed, the current is aligned parallel to the ripple crests. Thus, since the solid transport direction is governed by the direction of the current close to the bed, rather than by the mean current, the transport can be parallel to the ripple crests, i.e., orthogonal to the waves. Hence, in the presence of non-shore parallel ripples, the crest-aligned current close to the bed can have a component which is oriented away from the coast and the sediment transport can have a component directed away from the coast.

(d) The wave plus current friction factor normalized by the only current friction factor f_{wc}/f_{co} increases when the current decrease. In particular, it can be expressed as a power law depending on the ratio between the current strength and the wave orbital velocity U_c/U_w and parameterized in terms of the current angle independently on ripple geometry.

Furthermore, Faraci et al. (2008) observed the near-bed turbulence increasing with the macro-roughness induced by ripples. In particular, the laminar boundary layer which wakes above a flat rough bed induce a decrease in bottom shear stresses, whereas ripples make the bottom boundary layer turbulent increasing the bottom roughness. Such a phenomenon was not measured within the current-dominated regime due to the alignment of ripple crests with the current direction.

2.5 Velocity statistics

In Nature, the interaction between waves and current often occurs over an incoherent bed that can be mobilized by velocity fluctuations. Therefore the velocity statistics analysis concern both the hydrodynamics and the sediment transport.

In turbulent flows, velocity components, as well as other components, can be expressed as the sum of two terms. For example the velocity component in the direction of wave propagation U can be expressed as:

$$U = < U > + u', \tag{2.47}$$

being $< U >$ the ensemble averaged velocity, u' the turbulent fluctuating velocity. The ensemble average velocity can be further decomposed into the sum of the time average velocity $\overline{u}$ and the oscillating velocity $\tilde{u}$ which have a period equal to the wave period.

$$< U >= \overline{u} + \tilde{u}. \tag{2.48}$$

Faraci et al. (2018) analysed the influence in terms of velocity statistics of waves orthogonally superimposed to a current at a right angle over a bed covered by sand, gravel or ripples. They found that, in case of current only, the total near-bed velocity distribution looks like a Gaussian Probability Distribution Function (PDF). The velocity increasing produces an increased turbulence and a flatter and broader PDF as soon as the bed roughness increases. When waves are superimposed, the PDF shows two peaks around the maximum and the minimum velocity, i.e. the velocities measured below the wave crest and the wave trough, respectively. If waves are perfectly sinusoidal the two peaks show an equal magnitude. Moreover, peak visibility increases with the period increasing whereas the wave height does not play a significant role. Instead, moving from low to high roughness the turbulence becomes greater giving rise to a flatter PDF.

The turbulent fluctuations u' is generally not characterized by a double peak. Instead, assuming z as the vertical direction and W the velocity component in the vertical direction, further statistics should be taken into account: the Reynolds stress $\overline{u'w'}$, the skewness $s = u'^3/(\overline{u'^2})^{3/2}$ and the kurtosis $k = u'^4/(\overline{u'^2})^2$. In particular, this skewness is a measure of the asymmetry of the with respect to the average value $\overline{u}$. If the distribution is symmetric with respect to $\overline{u}$ the skewness vanishes whereas if the largest fluctuations of u' are positive the skewness is positive; the opposite occurs if the largest fluctuations are negative. Instead, the kurtosis assumes values bigger than 3 if the peak of the is more pronounced than the peak of the normal distribution.

2.6 Discussion

The hydrodynamics of a coastal environment is often regulated by the presence of wave and currents. While the waves are usually generated by the wind, the currents may be driven by the tides, the wind, the wave-seabed interaction. The mutual interference between waves and currents, co-linear or orthogonal to the direction of wave propagation, may induce a non-linear modification of phase averaged velocities and wavelength or change the structure of the boundary layer which affects both friction factor and bed shear stresses (Jonsson, 1966), with impacts on the longshore sediment transport (Bijker et al., 1974; Faraci et al., 2008).

Because of the complexity of the non-linear interaction between some of the analysed phenomena such as the Longuet-Higgins steady streaming, the wave asymmetry steady streaming and the undertow, laboratory models at an appropriate scale (micro, small, medium, large) are often realized in order to look into the coastal hydro-morphodynamics. In particular, within a wave flume, small changes in terms of wave height and period, depth beach profile steepness, and even ripple and breaking bar shape can produce the prevalence of the vorticity, the wave asymmetry or the mass balance among others. Such a situation gives rise to a flow that strongly influences the bed morphodynamics which, in turn, affects the hydrodynamics itself (Petrotta et al., 2017a,b, 2018).

During the small-scale experimental campaign, both regular and random waves were propagated above on a non-cohesive bed in order to analyse the effects of the flow on ripple shape, asymmetry and migration velocity. Then, a bed profile representative of the performed experiment was solidified in order to better clarify the effects of such a rippled beach on the inner and outer flow velocities. Moreover, a velocity statistics analysis was performed providing a new insight on the flow turbulence and its effects on the rippled bed by the vorticity dynamics.

The impacts of a small-scale model of the hydrodynamics above a fixed bar were compared with those of a large scale model.

Within a wave basin, the mutual influence between monochromatic waves and currents at a right angle was investigated throughout the water depth and, in particular, within the bottom boundary layer. In particular, the horizontal flat bed was covered by sand, gravels and artificial fixed ripples, respectively observing its influence on the hydrodynamics.

3 Instrumentation

The experimental campaign aimed to analyse the wave-current interaction was carried out within three facilities: the small scale wave flume of the Hydraulics Laboratory at the University of Messina (UM) (Italy); the large scale wave flume CIEM of the Universitat Politècnica de Catalunya (UPC) (Spain); the DHI Water and Environment Shallow Water Basin (Denmark). The access to the large infrastructures was granted by the HYDRALAB+ EU Project within respectively the Transnational Access HYBRID and WINGS.

The instruments deployed throughout the experimental campaigns in order to measure both the morphodynamics and the hydrodynamics are here described. Since they are functional for the different experimental campaigns, they are described apart from the facilities in which they are employed.

3.1 Acoustic Doppler Velocimeters

Vectrino Single Point The Vectrino Single Point (VSP) is a high-resolution acoustic velocimeter used to measure 3D water velocity fluctuations at sample rates from 25 to 200 Hz. The Vectrino uses the Doppler effect to measure current velocity by transmitting short pairs of sound pulses, listening to their echoes and, ultimately, measuring the change in pitch or frequency of the returned sound.

The probe consist of four receive transducers, each mounted inside the receiver arm, and a transmit transducer in the center. The sampling volume resembles, approximately, a cylinder with the z axis along the axis of the transmitter. It is placed 5 cm far from the transducer which could be down or side looking, see Figure 3.1, and it is characterized by a diameter of 6 mm.

Since the sound does not reflect from the water itself, it is necessary to scatter small suspended particles in the water (zooplankton or sediment). If the water is clear, the probe measurements could be considerably noisy. In such a circumstance, it is worthwhile to increase the suspended particle concentration by a seeding system.

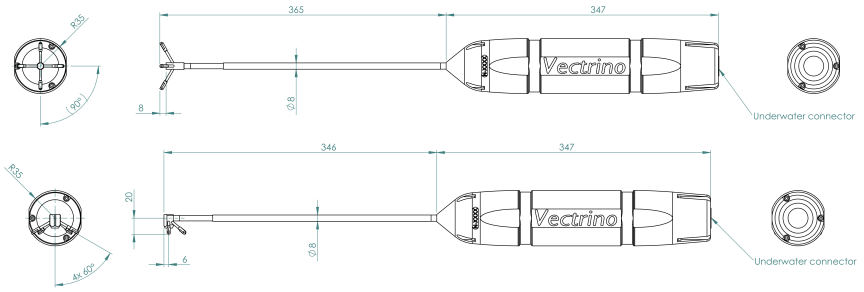

Figure 3.1: Sketch of the Vectrino Single Point, down-looking (above) and side-looking (below).

Furthermore, the down-looking probe measurements cloud be affected by the presence of a boundary close to their sampling volume. This is especially the case of an hard boundary (rocks, concrete, glass, etc.) and/or a weak water echo. For each velocity range, there are one or two distances that give rise to problems. The existence of these "weak spots" can be identified in the data record by a decrease in the correlation and an increase in the velocity variance. As recommended by Nortek AS, Table 3.1 summarize the distances to avoid from the sampling volume to the boundary.

Table 3.1: Vectrino Single Point "Weak Spots".

Range $[m \cdot s^{-1}]$	Distances [cm]	
4	2	5
2.5	3	10
1	5	12
0.3	10	23
0.1	23	45
0.03	38	75

However these distances are approximate. The vertical extent depends on the bottom composition and is about 0.5 cm for a flat bottom. However, by means of the acquisition software, the user could set the VSP in order to increase the quality

signal. In particular, since the problem is less acute at the lower velocity ranges, Nortek AS suggests to avoid to avoid the higher ranges unless needed.

The data acquisition software stores data in .vno extension files that could be converted in an ASCII $*$.txt file which includes four columns reporting the velocity components along x, y, $z1$ and $z2$ respectively. The two measured independent vertical velocities are redundant information and are typically used to assess data quality. Other columns report the Signal to Noise Ratio (SNR) and the Correlation for each of the components. Alternatively, data could be collected in three files whose extension are .hdr, .pck and .dat respectively. The first two of them include the instrument configuration, i.e. velocity range, sample rate together with the distance from the bottom to the transducer, whereas the third one contains the velocity measurement and some variables that convey the data quality, i.e. SNR and Correlation.

3.1.1 Vectrino Profiler

The Vectrino Profiler (VP) is an acoustic Doppler velocimeter able to profile three-component velocity over a vertical range of 3 cm, with a spatial resolution of 1 mm, and a sampling rate up to 100 Hz. Simultaneously, it can measure the distance to the bottom at a 10 Hz rate by interleaving bottom detection and velocity profiling.

The single central transceiver is in conjunction with four passive receivers angled at 30° towards the transceiver, see Figure 3.2a. Measurement range starts 40 mm down to 74 mm from the central transceiver divided into 34 measuring cells with 1 mm resolution. Moreover, the diameter of the control volume is 6 mm.

The geometrical arrangement of these components produces a focused intersection point approximately 50 mm below the transceiver. Far from such a "sweet spot", the signal divergence significantly reduces the size of the sampled area giving rise to a reduction in the data quality together with the noise parabolic increasing. Therefore, mean velocity magnitudes are biased by variable amounts in the proximal cells but are consistently underestimated in the distal cells. Thomas et al. (2017) state that the most reliable velocity data are normally collected within approximately 43 and 61 mm below the transceiver. Moreover, since the seeding concentration strongly impact on data reliability, they suggest an optimum acoustic seeding concentration of 3000-6000 mg l^{-1}.

Within the small scale wave flume, the Vectrino Profiler was fastened to a trolley which was able to move along the flume length, see Figure 3.2b. The

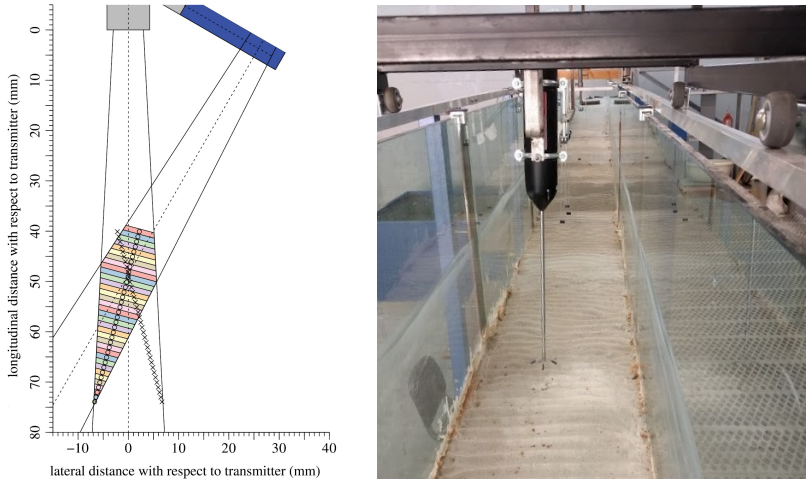

(a) (b)

Figure 3.2: Vectrino Profiler: (a) particular of transceiver and receiver signal overlapping (Thomas et al., 2017); (b) the probe deployed above the sandy bed.

vertical alignment of the probe was calibrated with a tubular spirit level. The bed-transceiver distance was regulated on a measuring rod by means of an adjustment screw.

3.2 Laser Doppler Anemometer

Laser Doppler Anemometry (LDA), also known as Laser Doppler Velocimetry (LDV), is an optical technique ideal for non-intrusive 1D, 2D and 3D point measurement of velocity and turbulence distribution in both free flows and internal flows.

The instrument deployed within the UPC flume consists of a DopplerLite laser with up to 300 mW per wavelength, a FiberFlow Transmitter and manipulators for optical fiber in-coupling and a 2D FiberFlow probe, see Figure 3.3a.

Throughout the HYBRID campaign two 27 mm diameter probes were deployed within the UPC wave flume, see Figure 3.3c. These two probes were able

to measure from 60 to 160 mm forward to their head if equipped with the standard front optics. In particular, Figure 3.3b shows that each probe has five exiting beams: the centre beam combined with the blue and green beams form two fringe patterns at an angle to each other. Two velocity components in the horizontal plane, u1 and u2 as showed in Figure 3.3b, are measured with this. The violet beam pair measures the vertical component.

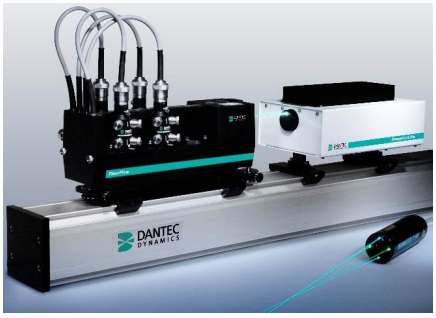

(a)

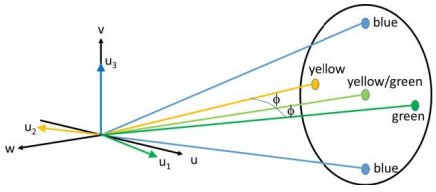

(b)

(c)

Figure 3.3: Laser Doppler Anemometer: (a) Dantec LDA, (b) LDAs probes, (c) reference system sketch.

3.3 Wave Gauges

3.3.1 Resistive wave gauges

A resistive wave gauge consists of a pair of parallel stainless steel wires (the absence of other support reduces the interaction between the measuring device and the incoming/reflected waves), see Figure 3.4. The current flowing between the probe wires is proportional to immersion depth and this current is converted into

an output voltage. The output circuitry is suitable for driving both a chart recorder and a data logger.

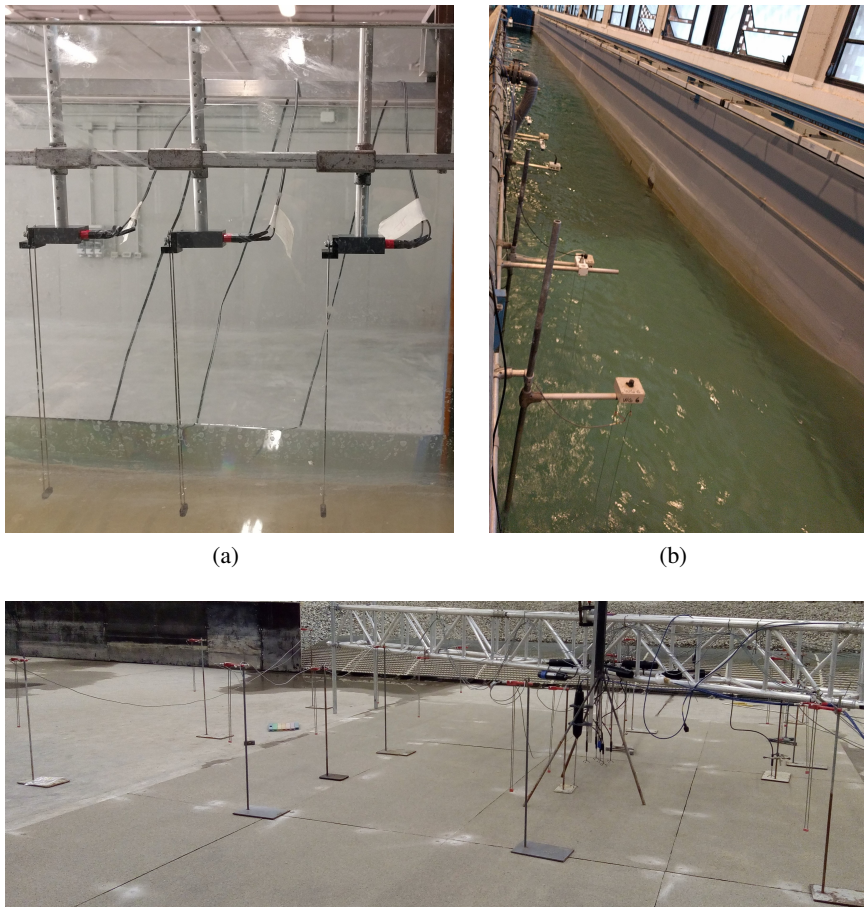

(a) (b)

(c)

Figure 3.4: Resistive wave gauges at: (a) University of Messina wave flume, (b) UPC wave flume, (c) DHI basin.

Wave gauges deployed within the three laboratories are slight different, in particular the University of Messina wave flume is equipped by gauges with sample frequency equal to 100 Hz (provided by Churchill Controls Ltd, see Figure 3.4a),

whereas both UPC wave flume's (provided by LIM-UPC, see Figure 3.4b) and DHI basin's (provided by DHI©, see Figure 3.4c) gauges sample frequency is 40 Hz.

The transformation function (from voltage to depth) must be calibrated due the possible changes in the water conductivity (temperature and salinity concentration effects). An overall calibration from output voltage to wave height can be performed by measuring the change in output voltage, while raising or lowering the mean water level of the flume or the gauge support. Data acquisitions voltages from the resistive wave gauges are captured on the laboratories' general data acquisition system.

3.3.2 Acoustic wave gauges

The UPC deployed 18 *mic*+130 from Microsonic acoustic sensor throughout the flume length, see Figure 3.5a. It emits ultrasound pulses that reflect on the scatters within the water and return an echo. Such a gauge is able to measure the thickness of the overtopped water layer within 0.20 m up to 1.7 m from its position with a resolution sampling rate up to 0.18 mm and a transducer frequency of 200 kHz.

The ultrasound measurement system outputs a voltage proportional to distance to the water surface varying between 0 and 10 V. A calibration straight line, previously done, is applied to the output voltage to transform the intensity signal to the proportional distance.

3.4 Pore Pressure Transducers

Fifteen ATM/N pressure sensors produced by STS are deployed along the UPC wave flume, see Figure 3.5b. Before the use, each probe required a calibration by which the signal intensity output could be related to water height with an accuracy smaller than 0.5.

The transducer uses a pressure sensitive diaphragm with a vibrating wire element attached to it. The diaphragm is welded to a capsule which is evacuated and hermetically sealed. Fluid pressures acting upon the outer face of the diaphragm cause deflections of the diaphragm and changes in tension and frequency of the vibrating wire. The changing frequency is sensed and transmitted to the readout device by an electrical coil acting through the walls of the capsule, for details see Stringer et al. (2014).

(a)

(b)

Figure 3.5: Non-resistive wave gauges: (d) acoustic wave gauge, (e) pore pressure transducer.

3.5 Main limits

Experimental campaigns have to deal with both model, scale and measurement effects which induce considerable differences between the up-scaled model and the prototype parameters. The incorrect reproduction of prototype features such as geometry (2D modelling or reflections), flow or wave generation techniques (turbulence intensity level or linear wave approximation) or fluid properties (fresh instead of sea water) generates the so-called model effects, as widely reported in literature (Yalin and Yalin, 1971; Kobus, 1980; Novák and Cabelka, 1981; Hughes, 1993; Heller, 2011). Instead, scale effects (Yalin and Yalin, 1971; Le Méhauté, 1990; Hughes, 1993; Martin and Pohl, 2000) arise due to the inability to keep each relevant force ratio constant between the scale model and its real-world prototype, particularly when the flow interaction with non-cohesive sediments is modelled. Measurement effects (Schüttrumpf and Oumeraci, 2005) include non-identical measurement techniques used for data sampling in the model and prototype (intruding vs. non-intruding measurement system or different probe sizes).

Throughout the performed experimentation, it was necessary to manage a wide

range of constraints like the reflection generated by wavemaker motion. Within the small-scale wave flume, the reflection was limited placing, at the back of the wavemaker, some mattresses of creased pipe piece. Within the shallow water basin, the reflection was partially absorbed placing parabolic absorbers and a coarse beach in front of the wavemaker. Moreover, the residual effects of reflection on waves were evaluated and taken into account.

Furthermore, several boundary conditions were adopted.

- Models were assumed to be two-dimensional, i.e. wavefronts were cylindrical and were propagated orthogonally to cylindrical beaches.
- Throughout the fixed bed experiment the flow was not able to affect the bottom roughness both in terms of bedform shape and sand stratification. Thus, although bedform dimensions were compatible with the whole set of the hydrodynamic conditions object of study, they were generated by propagating just one of the examined waves. In particular, the wave which gave rise to the most frequent bedform shape.
- Throughout shallow water basin experiments artificial fixed ripples were deployed. Such ripples were cylindrical, with constant wavelength and height and their shape cannot be affected by near-bed hydrodynamics.
- Fixed bedforms could not migrate.
- Particle-size distribution did not change during each experimental campaign.

As concerns the measurement effects, they affect both morphodynamic and hydrodynamic measurements, i.e. water surface elevation and velocities, because of the error due to the instruments. Morphodynamics was measured by optical systems whose reliability is related to the laser light brightness, the camera resolution, by the distortions caused by the central projection due to the the camera location with respect to the bedforms.

Water surface elevation was measured by wave gauges which were periodically calibrated. Such an operation often required a long time, therefore it occurred once or twice a day. However, changes in water temperature might cause calibration errors whose identification is rather difficult. Whereas, velocities were measured by both acoustic and laser Doppler velocimeters, ADVs and LDVs respectively. Many factors affected ADVs' reliability: bottom reflection, suspended sediment concentration, ambiguity in zero up-crossing determination, sync and connection problems. Moreover, turbulence may cause bias in LDVs' velocity measurements

(Roesler et al., 1980; Zhang, 2002). Chapters 4, 5, 6 describe the experimental procedures carried out to avoid some of these negative effects and to filter out others during the signal processing.

Nevertheless, some effects could not be removed. In particular, ADVs' sampling volume consists of one or more cells whose dimensions are finite. Thus, the velocity measured at any given point is an averaged velocity. Furthermore, although LDVs' sampling volumes are considerably smaller, they are not infinitesimal as well.

4 Small scale wave flume experiments

The wave flume of the Hydraulics Laboratory at the University of Messina (UM) (Italy) is 18 m long, 0.40 m wide and 0.80 m high with flat stainless steel bottom and glass walls (Figure 4.1a).

Waves are generated within the flume by means of a flap type wavemaker which is able to reproduce both regular and random waves characterized by wave heights up to 0.12 m and wave periods between 0.5 and 2 s. The wavemaker is driven by a pneumatic system and is electronically controlled.

At the back of the wavemaker, some mattresses of creased pipe pieces are placed to absorb any spurious reflection caused by the flap motion. The facility was also used in other campaigns, such as Liu and Faraci (2014) and Faraci (2018).

Starting 8 m away from the wavemaker and for the remaining flume length, the bottom is covered with a layer 0.2 m thick of uniform sand, characterized by a median grain size $d_{50} = 0.25$ mm. Farther, a plane beach 3.5 m long with a slope of 1:10 is built oppositely to the wavemaker in order to minimize reflection. Moreover, the plane beach has the role of triggering the asymmetry of the waves propagating along the flume.

4.1 Experimental procedure

Each test required some preliminary operations, i.e. the definition of the control parameters to be provided to the wavemaker in order to generate the desired waves, the choice of the Vectrino Profiler software configuration, the calibration of the optical system. However, the procedure adopted in case of fixed bed slight differs from that adopted in case of moveable bed, therefore they are described separately.

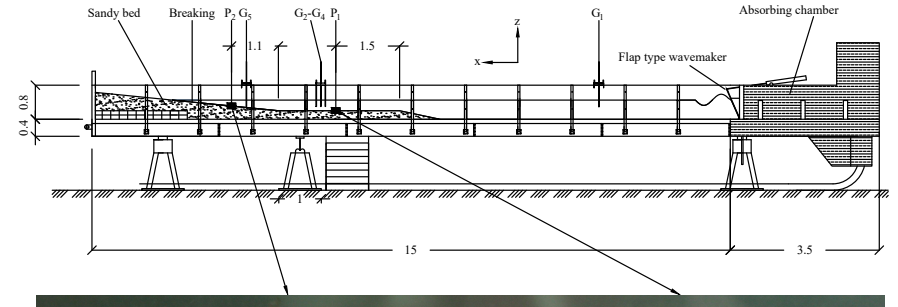

(a)

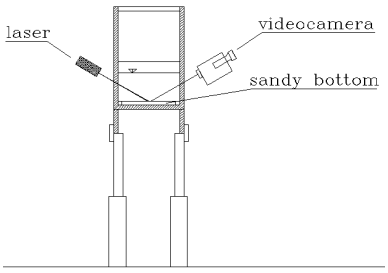

(b)

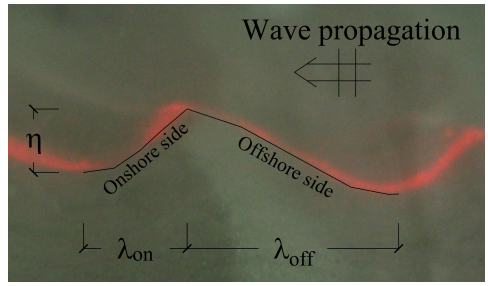

(c)

Figure 4.1: Experimental set up adopted in the present experimental campaign at UM: (a) wave flume together with a rippled bed overview; (b) sketch of the optical structured light technique; (c) laser light on the sandy bottom showing the two half-wavelengths λ_{on} and λ_{off} and the height η; (d) ripples picture.

4.1.1 The moveable bed case

Each test started with the sandy bed levelling. This last task had to be carefully performed in order to remove any ripple mark from the sandy bed and to start each experiment from an initially flat condition.

Hydrodynamic and morphodynamic measurements had to be acquired separately. Indeed, the flow measurements required a sufficiently large concentration of particles in suspension in order to allow the acoustic signal to be reflected by the suspended particles. The morphodynamic measurements instead had to be performed in perfectly clear water to make the image formation possible on the camcorder lenses. The experimental procedure of mobile bed tests followed such a schedule:

- In the presence of clear water and starting from an initially flat bed, the waves were propagated on the sandy bottom and triggered the formation of ripple bedforms. At the same time, the structured light approach was used to acquire the rippled bed images by means of a camera. The morphodynamic acquisition ended once the equilibrium was achieved, which generally occurred within 15 minutes.

- Once the morphodynamic measurements were performed, the water was seeded by means of talc powder and two vertical profiles were acquired, the first one located on the horizontal sandy bottom (P_1), the other one on the sloping bed (P_2). The origin of the vertical axis was placed in correspondence to the ripple trough at the two positions P_1 or P_2. The choice of the trough was carried out in order to minimize the effects of ripple migration on the Vectrino's bottom distance. In addition, velocities were measured after the reaching of the ripples equilibrium configuration, when ripple migration reached a steady state.

4.1.2 The fixed bed case

The fixed rippled bed was recreated by the propagation of a monochromatic wave characterized by a height $H = 8$cm and a period $T = 1$s. The equilibrium condition was reached propagating about 1800 waves, see Figure 4.2a. Later on, the fume was dried and the bed was solidified covering the wet sand with two layers of concrete (Figure 4.2b), sifted in order not to alter the sand granulometry and the ripple profiles.

Once the concrete had hardened, several vertical profiles were acquired to describe the hydrodynamics above two pretty cylindrical ripple wavelengths named

P_1 and P_2. The first one was placed 1.5 m further the beginning of the horizontal sandy bottom (section P_1), 2.45 m, whereas the second one was placed 2.45 m forward, i.e. 1.1 m further from the beginning of the slope (section P_2), see Figure 4.1a. Ripple P_1 length λ was about 4.2 cm and the height η was 0.6 cm whereas ripple P_2 length was about 6.1 cm and height 0.9 cm. Ripple P_1 is symmetrical and, although the offshore flank of the ripple P_2 is steeper than its onshore flank, its half-wavelengths are similar. Indeed, because of the high near bed turbulence, it was necessary to thicken the concrete layer in proximity to the breaking zone. Such a circumstance subtracted some degree of asymmetry from ripple P_2. In uniform flow conditions, Raudkivi (1997, 1998) considered that the transition from rolling grain to vortex ripples occurs when the parameter $\sigma = 0.074 d_{50}^{-0.253}$ is equal to 0.10, being d_{50} in millimeters. Moreover Dingler and Inman (1976) indicated that transition ripples occur for $\eta/\lambda = 0.15$. Since, in the present experiments, $\sigma = 0.105$ and ripples P_1 and P_2 were characterized by η/λ equal to 0.144 and 0.148 respectively, both ripples are close to the vortex ripple condition.

In the present experiments, nine equally spaced measuring locations (L_1-L_9) were placed along each of the two ripples P_1 and P_2 (see Figure 4.2c).

4.2 Measurements

4.2.1 Water surface elevation

Measurements of wave characteristics throughout the wave flume were performed by means of five resistive wave gauges, see Paragraph 3.3.1. The first one (G_1) was located 3.25 m off the wavemaker in order to measure fully developed waves, three of them (G_2, G_3, G_4) were placed on the horizontal sand layer and spaced in such a way to allow the wave reflection along the flume to be evaluated by means of Mansard and Funke (1980) method. In particular, wave reflection along the flume was always comprised between 15 and 20% of the incident wave. Only for largest wave periods reflection grew up to 30%. The last gauge (G_5) was located on the sloping beach where the waves shoal.

4.2.2 Morphodynamics

The bed morphology was acquired by means of a structured light optical system (Faraci and Foti, 2002; Faraci et al., 2012, for details on the technique). A Canon EOS 450D camera with a 6.4 MP resolution and a ± 1 mm accuracy was used.

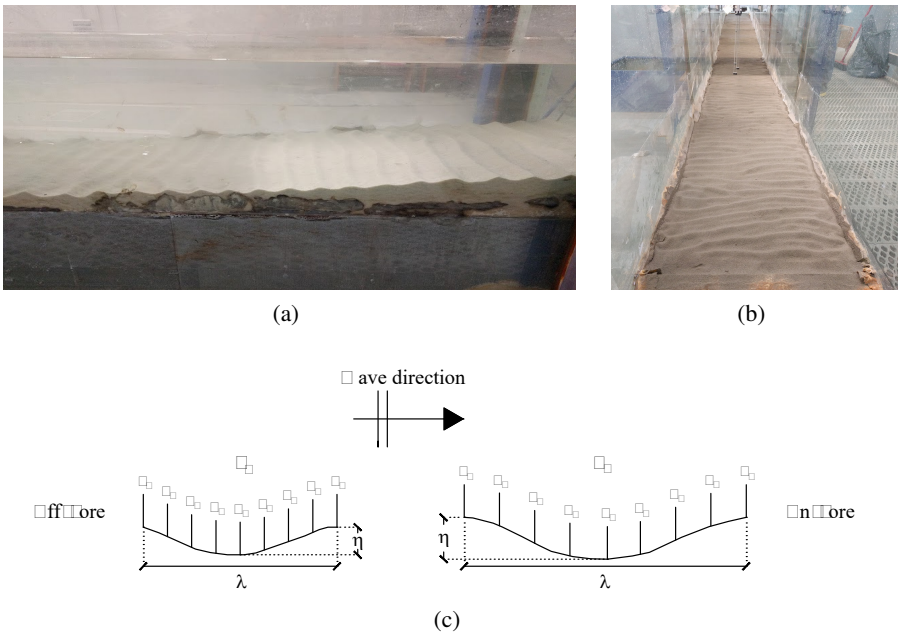

Figure 4.2: The rippled bed: (a) picture of the bed at the equilibrium condition, (b) picture of the fixed bed, (c) ripples P_1 and P_2.

The light sheet optically slices the measured body creating a cross-sectional image that can be observed and recorded through a video camera and then analysed to obtain the ripple dimensions (Figure 4.1b, 4.1c). Once the image (Figure 4.1a) was gathered by the video camera, suitable image processing procedures were adopted, in particular, the correspondence between the image units, given in pixels, and the object dimensions was determined. This task was accomplished by acquiring the image of a known object and deriving the coefficients which give the unit dimension of one pixel in both horizontal and vertical directions. Moreover, in few experiments, the accuracy of the system was compared with measurements taken by means of a graduated rod.

4.2.3 Hydrodynamics

Velocity profiles were acquired by means of a Vectrino Profiler (Nortek As.), see Paragraph 3.1.1 for details. In particular, Velocity profiles were acquired at two positions, the first one located 1.5 m far from the beginning of the sandy bed (position P_1) and the second one located 1.1 m after the beginning of the slope (position P_2), see Figure 4.1a.

Profiles were obtained by vertically overlapping each measurement station by a certain amount. This was necessary in order to be able to remove the lower part of the sampling volume data, characterized by low SNR because of sound reflection from the bottom, without producing any gap in the profiles. When vertically moving from a position to another along the profile, the sensor position is shifted up by an amount Δz every two minutes, i.e. after about 100 wave periods. In order to get the proper overlap between two successive stations, in most of the tests, Δz was kept equal to 2 cm in order to reconstruct the entire velocity profile. According to Thomas et al. (2017), throughout the remaining tests, data collected outside the region between approximately 43 and 61 mm below the transceiver were marked as not sufficiently reliable and thrown out. This occurrence required to reduce the overlap Δz to 1 cm during *Reg*1-*Reg*3 and $T1$-$T9$ tests and to 0.5 cm during *Reg*4 and *Reg*9 tests, see Table 4.1 for details on the parameters of these experiments. Finally, due to the near bed acoustic interference together with the high near bed suspended sediments concentration, (see Thomas et al., 2017), data within 2 mm from the bottom were discarded, (see Koca et al., 2017; Wengrove and Foster, 2014).

Velocities were measured throughout the water column, i.e. from the bottom to about 4 cm below the wave through, at P_1. Analogously, profiles at P_2 were measured up to an elevation of about 10 cm. Measurements started three minutes after the wavemeaker launch in order to reach a stable flow condition. Then the flow field at each position was acquired. This operation took about twenty minutes ($\Delta z = 1$ cm) on the sloping bed, where the water depth was 0.145 m, and forty on the horizontal plane, where the water depth was 0.245 m. In the end, the wavemaker was stopped.

During the fixed bed T_9 test, Vectrino Profiler acquired data for 10 minutes at each measuring station in order to check the velocity statistics convergence. Moreover, the Vectrino Profiler started measuring on sync with the wavemaker launch. In this case, the transient condition had to be filtered out during the signal processing, thus data collected throughout the first three minutes were not analysed.

Since the reliability of the measured velocities is related to Correlation and SNR, (see e.g. Van Der A et al., 2017b; Yoon and Cox, 2010), two acceptance thresholds were adopted: $COR \geq 90$ and $SNR \geq 30$ near the sweet spot, i.e. from 50 to 65 mm below the transceiver, or $SNR \geq 20$ elsewhere. Non-reliable data were replaced by a linear interpolation. Finally, data were despiked by means of the Goring and Nikora (2002) method and replaced by a linear interpolation. To improve data integrity the Power Level was set on High value and some talc powder was dispersed near the probe head to increase the number of scatters in the sampling volume. Moreover, in one of the performed tests (Reg_2), the velocity profiles were acquired once with a cell size parameter equal to 1 mm and a second time with a cell size of 2 mm. However, important differences were not observed comparing the two obtained profiles, hence a cell size equal to 1 mm was adopted for the remaining tests.

A zero up-crossing method was adopted to split the cleaned signal and to calculate the ensemble averaged velocities. Throughout both the moveable bed and the fixed bed campaign zeros were identified within the velocity signal except during the $T9$ test where zeros were determined from the elevation measured by the resistive wave gauge closest to the Vectrino, i.e. $G4$. Finally, a matrix containing in each column a velocity fluctuation throughout a period and in each row a phase was arranged. Periods longer than 1.03 T or shorter than 0.97 T, where T is the reference period, (generally 2-5 %) were rejected.

4.3 Experiments

4.3.1 The moveable bed case

Fifteen experiments were performed. Twelve of these experiments used regular waves, and three used random waves characterized by TMA peak period $T_p = 1.2$, mean period $T_m = 0.95 - 1.10$s and peak enhancement factor $\gamma = 3.3$. Velocity statistics were computed only for regular wave tests.

In Table 4.1 the experimental parameters of each test are reported; the last three rows refer to random waves. In particular the first column indicates the test name; the second column reports the water depth along the sloping bottom at the same position where ripple characteristics were measured that sometimes slightly differed from the designed $d = 0.145$ m depth value; the two following columns show the wave height or the significant wave height in the case of random waves and the mean period measured by the offshore wave gauge G_1. Finally, the

last two columns report the test duration and the measurement type indicating if throughout the test hydrodynamic (*hydr.*) and/or morphodynamics (*morph.*) measurements were carried out. To verify that 15-minute test length was sufficient to reach the morphodynamic equilibrium, two tests, namely Reg_5 and Reg_{11}, were repeated by performing the measurements for 30 minutes (Reg_4 and Reg_{10}). The results showed no appreciable differences in terms of ripple shape between these longer tests and the corresponding 15-minute tests, therefore the other measurements were not repeated.

Table 4.1: Hydraulic characteristics of the performed experiments at the small scale wave flume of the University of Messina.

Test name		d [m]	H, H_s [m]	T, T_m [s]	Duration [min]	Measurement Type
REGULAR WAVES	Reg_1	0.145	0.067	1.23	15	hydr.+morph.
	Reg_2	0.145	0.069	1.22	15	hydr.+morph.
	Reg_3	0.145	0.071	1.01	15	hydr.+morph.
	Reg_4	0.145	0.083	1.01	30	morph.
	Reg_5	0.145	0.083	1.01	15	hydr.+morph.
	Reg_6	0.145	0.157	1.01	15	hydr.+morph.
	Reg_7	0.145	0.057	0.84	15	hydr.+morph.
	Reg_8	0.145	0.096	0.84	15	hydr.+morph.
	Reg_9	0.145	0.091	0.84	15	hydr.+morph.
	Reg_{10}	0.145	0.132	0.84	30	morph.
	Reg_{11}	0.147	0.127	0.84	15	hydr.+morph.
	Reg_{12}	0.145	0.122	0.84	15	hydr.+morph.
RAN	Ran_1	0.136	0.085	0.90	15	morph.
	Ran_2	0.138	0.062	0.79	15	morph.
	Ran_3	0.134	0.057	0.90	15	morph.

During every test, water elevation was measured for two minutes after the beginning of the wave propagation by all the five resistive wave gauges, as described in Chapter 4.2. The five signals were phase averaged to obtain the ensemble wave at the five locations. In Figure 4.3 an example of the water elevation η, as recorded by the wave gauge G_5 located on the sloping bed, is reported for two regular wave tests Reg_5 ($H = 0.0825$ m; $T = 1.01$ s) and Reg_9 ($H = 0.0911$ m; $T = 0.84$ s). Due to the partial breaking observed in the horizontal bed, the wave height of Reg_5 test

was higher than wave height of Reg_9 test, however the caption shows that Reg_5 is smaller than Reg_9.

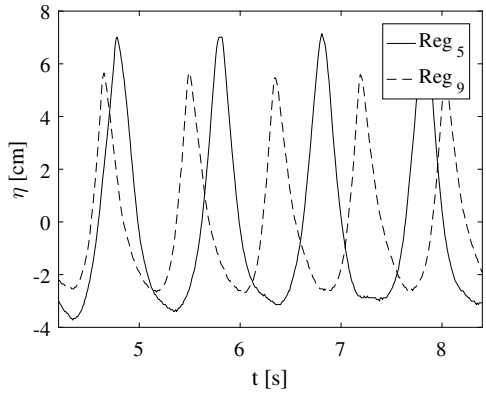

Figure 4.3: Water elevation for two regular wave tests measured by wave gauge G_5 (solid line: test Reg_5: $H = 0.0825$ m; $T = 1.01$ s; dashed line: test Reg_9: $H = 0.0911$ m; $T = 0.84$ s).

Figures 4.4a and 4.4b show the shoaling of water waves propagated during the tests Reg_5 and Reg_9. During Reg_5 test, waves grow and partially lose their symmetry due to the interaction with the horizontal plane bed. Then, in proximity of the breaking zone, waves become considerably skewed and asymmetric. Instead, during Reg_9, a partial wave breaking occurs above the plane bed, therefore wave height at G_2 is smaller than at G_1. Above the sloping beach, waves become skewed and asymmetric. This is also confirmed by the water surface elevation shown in Figure 4.3, where Reg_9 wave height appears to be sensibly smaller whit respect to the value acquired by gauge G_1 and reported in Table 4.1.

Hydro-morphodynamics parameters The dimensionless parameters usually employed in the analysis of ripple dynamics are:

- the relative density of sediments:

$$s = \frac{\rho_s}{\rho} \tag{4.1}$$

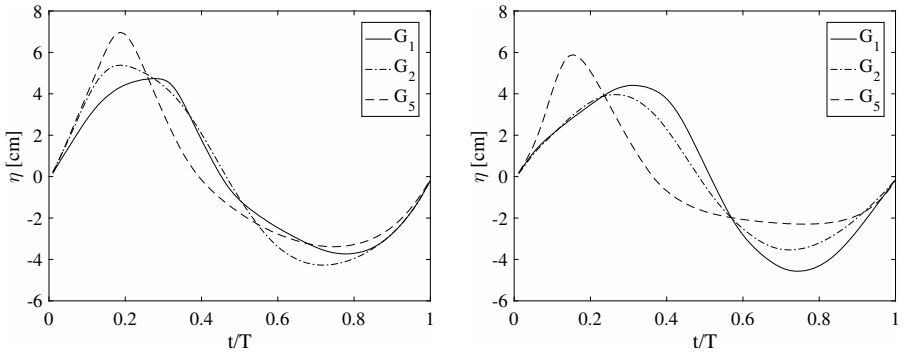

Figure 4.4: Ensemble water surface elevation measured offshore (wave gauge G_1), above the plane sandy bed (wave gauge G_2) and above the sloping bed (wave gauge G_5): (a) Test Reg_5 ($H = 0.0825$ m; $T = 1.01$ s); (b) Test Reg_9 ($H = 0.0911$ m; $T = 0.84$ s).

- the flow Reynolds number:

$$Re = \frac{U_0 A}{\nu} \tag{4.2}$$

- the sediment Reynolds number:

$$Re_d = \frac{U_0 d_{50}}{\nu} \tag{4.3}$$

- the mobility number:

$$\psi = \frac{U_0^2}{(s-1)\, g d_{50}} \tag{4.4}$$

- the Shields parameter:

$$\theta = \frac{1}{2} f_w \frac{U_0^2}{(s-1)\, g d_{50}} \tag{4.5}$$

- the grain roughness Shields parameter:

$$\theta_{2.5} = \frac{1}{2} f_{2.5} \psi \tag{4.6}$$

Where:

- ρ_s is the sediment density;
- ρ is the water density;
- U_0 is the orbital velocity amplitude;
- A is the orbital displacement amplitude;
- ν is the kinematic water viscosity;
- d_{50} is the median grain size;
- f_w is the friction factor defined as $\frac{2}{\sqrt{Re}}$ for smooth laminar flow, i.e. $Re < 3 \cdot 10^5$ and as $\exp[5.213(r/A)^{0.194} - 5.977]$ for the turbulent flows;
- $f_{2.5}$ is the grain roughness friction factor, as defined by Swart (1974).

In Table 4.2 the ripple characteristics at equilibrium, namely the ripple wavelength $\lambda_{eq} = \lambda_{off} + \lambda_{on}$, being λ_{off} and λ_{on} the half-wavelengths in the offshore and onshore direction respectively, as shown in Figure 4.1c, the ripple height η_{eq} averaged over 3-6 ripples and time averaged at the equilibrium, i.e. for the final 3 minutes of each test, are reported. The variable v_{15} in Table 4.2 is the migration velocity obtained taking the value at t=15 min of the line fitting the ripple crest migration velocity v_0. The latter was obtained as the displacement observed in two successive frames, divided by the elapsed time interval. Table 4.2 also reports the main previously mentioned hydrodynamic parameters and in particular, the orbital velocity amplitude U_0 just above the bottom boundary layer measured by a Vectrino Profiler together with the orbital displacement amplitude A. Finally, the non dimensional parameters, i.e. the flow Reynolds number, the sediment Reynolds number, the mobility number, the Shields parameter and the grain roughness Shields parameter, respectively are reported. The sediment relative density is constant and equal to $s = 2.65$ and the critical Shields parameter is equal to $\theta_{crit} = 0.0415$ (Soulsby et al., 1997) throughout the experimental campaign thus it was not included in the table. Based on the Shields parameter, being $\theta > \theta_{crit}$, the sediment are mobilized and vortex ripples appears. Sheet flows do not occur as $\theta < 0.8$, see Dingler and Inman (1976).

Table 4.2: Hydro-morphodynamic characteristics of the performed experiments at the small scale wave flume of the University of Messina.

Test name	λ_{eq} [cm]	η_{eq} [cm]	v_{15} [cm·min^{-1}]	U_0 [cm·s^{-1}]	A [cm]	Re [-]	Re_d [-]	ψ [-]	θ [-]	$\theta_{2.5}$ [-]
Reg_1	6.11	1.49	0.07	38.9	7.6	29711	97	37	0.22	0.37
Reg_2	5.07	1.05	0.08	31.9	6.2	19694	80	25	0.18	0.27
Reg_3	5.22	0.89	0.04	35.1	5.6	19759	88	30	0.22	0.34
$Reg_4(P_1)$	4.20	0.60	0.04	32.4	5.2	16916	81	26	0.20	0.30
$Reg_4(P_2)$	5.11	0.68	-0.32	41.6	6.7	27832	104	43	0.26	0.45
Reg_5	5.71	0.84	0.03	45.2	7.3	32798	113	50	0.28	0.51
Reg_6	6.14	0.75	-0.54	52.1	8.4	43671	130	67	0.32	0.64
Reg_7	3.34	0.44	-0.17	30.9	4.1	12816	77	24	0.21	0.30
Reg_8	3.91	0.78	0.00	33.6	4.5	15079	84	28	0.23	0.34
Reg_9	4.40	0.74	-0.20	44.2	5.9	26118	111	48	0.30	0.53
$Reg_{10}(P_1)$	3.53	0.77	0.08	32.7	4.4	14264	82	26	0.22	0.33
$Reg_{10}(P_2)$	5.03	0.73	-0.80	42.9	5.7	24607	107	46	0.29	0.51
Reg_{11}	5.31	0.69	-0.82	42.9	5.7	24613	107	46	0.29	0.51
Reg_{12}	4.04	0.59	-0.43	40.0	5.3	21369	100	40	0.27	0.45
Ran_1	6.12	0.68	-0.30	33.4	4.9	16284	84	28	0.22	0.33
Ran_2	4.28	0.62	-0.05	24.1	3.1	7442	60	14	0.17	0.21
Ran_3	5.42	0.81	0.04	25.3	3.7	9252	63	16	0.16	0.21

4.3.2 The fixed bed case

The experimental campaign consisted of the nine tests $T1 - T9$ during which the hydrodynamics on a fixed rippled bed was investigated. In particular, velocities were measured along the two ripples P_1 and P_2 (see Chapter 4.1.2) placed respectively on the horizontal bed and on the sloping bed. Thus, velocities measured at the two positions were compared in order to investigate the offshore-directed steady current triggered by the presence of the sloping bed.

In Table 4.3 a summary of the experimental conditions and of the main hydrodynamics parameters is reported. In particular, the first column indicates the test name, the second and third columns report the wave characteristics, namely the wave height H and period T, finally columns from the fourth to the seventh report the value of the semi-orbital amplitude and the Reynolds wave number, measured at both P_1 and P_2.

Table 4.3: Experimental conditions and main Hydrodynamics parameters. Experiments were carried out at the small scale wave flume of the University of Messina.

Test name	H [cm]	T [s]	A [cm/s^2]		Re [-]	
			P_1	P_2	P_1	P_2
$T1$	2.54	1.26	1.27	1.82	808	1655
$T2$	8.13	1.01	2.78	4.34	4825	11692
$T3$	6.27	0.84	1.42	2.48	1504	4611
$T4$	4.36	1.26	2.19	3.15	2381	4948
$T5$	8.70	1.01	2.98	4.64	5525	13389
$T6$	9.05	0.84	2.05	3.58	3133	9607
$T7$	13.05	0.84	2.95	5.17	6515	19977
$T8$	8.67	1.01	2.97	4.62	5487	13297
$T9$	5.86	1.26	2.94	4.23	4302	8939

The water depth d was kept fixed and equal to 0.245 m at section S_1 ($d = 0.145$ m at S_2).

The main hydrodynamics parameters employed in the present campaign are:

- the semi-orbital amplitude of the fluid outside the boundary layer:

$$A = \frac{U_\infty}{\omega} \tag{4.7}$$

- the wave induced velocity just above the bottom boundary layer:

$$U_\infty = \frac{H\omega}{2sinh(kd)} \tag{4.8}$$

- the wavenumber:

$$k = \frac{2\pi}{L} \tag{4.9}$$

- the flow Reynolds number:

$$Re = \frac{U_\infty A}{\nu} \tag{4.10}$$

4.4 Moveable bed

The hydrodynamics together with the morphodynamics of a moveable rippled beach is discussed in the present section. In particular, this chapter focus on the effects of a sloping beach on both velocity profiles and morphodynamics in terms of ripple shape and migration.

Moreover, a discussion on the main ripple predictors is here reported.

4.4.1 Analysis of the hydrodynamics

In order to understand the effects of the sloping beach on the hydrodynamics and, in turn, on the morphodynamic processes described afterwards, an analysis of the velocity data acquired by the Vectrino Profiler at the two positions P_1 and P_2 (see Figure 4.1a) was performed. More in detail, velocities were measured above the rippled bed generated by the propagation of regular or random waves after the achievement of the equilibrium configuration in terms of ripple geometry. During the tests, velocities were acquired at one vertical section, located at the ripple trough in order to reduce uncertainties in terms of bottom distance of measured velocities. Indeed, even when the equilibrium condition was reached, ripples continued oscillating around the equilibrium position throughout the test length. Hence, the distance of the transducer from the bed within a wave cycle could vary more above the ripple crest than on the trough because the last one is flatter.

In Figure 4.5a the cross-shore velocities at an elevation of 1.5 cm above the bed measured during experiment Reg_5 are shown along with the moving averaged velocity U_{MA} determined by averaging over ten periods. In fact, the wave propagation gives rise to an onshore directed mass transport between wave crest and trough

that in a two-dimensional situation must be compensated by a negative (offshore-directed) steady current, that can be here observed throughout the duration of the tests. Here, for the sake of clarity, only a short part of Reg_5 test is represented in the figure. Similar results were achieved throughout the other tests. The steady current U_{AVG}, averaged over the whole test duration, measured in all the performed regular wave experiments above the sloping bed, just outside the bottom boundary layer is summarized in Figure 4.5b. All the analysed wave conditions produce offshore directed averaged velocities. In particular, the highest negative velocities occurred for Reg_{10} and Reg_{11} tests. These tests are characterized by the highest values of the parameter H^2/T which is related to the mass transport (Dean and Dalrymple, 1991), together with the highest negative migration velocities, see Table 4.2.

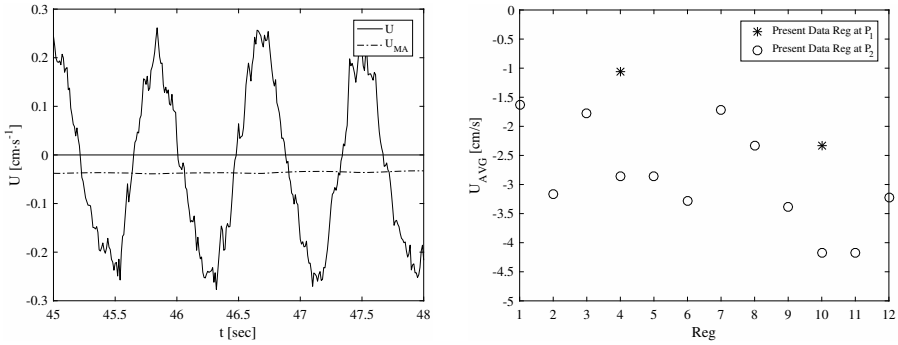

(a) (b)

Figure 4.5: (a) Cross-shore velocities measured at position P_1, Test Reg_5 ($H = 0.0825$ m; $T = 1.01$ s), U indicates the instantaneous velocity measured by the Vectrino profiler at the elevation of 1.5 cm centimetres from the bed, U_{MA} indicates the moving averaged velocity over a ten period time span; (b) Outer flow averaged velocities measured at position P_1 and P_2 throughout regular wave tests.

The signal acquired by each cell of the Vectrino Profiler was analyzed by a zero up-crossing method to obtain the phase-averaged velocity profiles.

For sake of brevity few tests were selected in order to provide an overview of the observed features. In particular, Figures 4.6 – 4.8 depict the velocity profiles of the experiments Reg_3, Reg_5, Reg_{11}, respectively at the positions P_1 (plane bed) and P_2 (sloping bed). The velocity profiles are shown at four phases: $1/2\ \pi$, π,

$3\pi/2$, 2π on the plane bed, and at two more phases, namely the ones at which the maximum and the minimum velocities are observed, at P_2 position. Indeed, on the sloping bed, due to wave asymmetry the positive peak occurs at $\phi = 14/32\ \pi$, $14/32\ \pi$, $12/32\ \pi$ and the negative peak at $\phi = 42/32\ \pi$, $44/32\ \pi$, $46/32\ \pi$ during Reg_3, Reg_5 and Reg_{11} test, respectively. Thus, an anticipation of both velocity maxima and minima occurs on the sloping bed with respect to the horizontal bed case. Moreover, the velocity profile averaged over the entire wave period is also shown. Because of the wave asymmetry, zero down-crossing is reached before the π phase therefore at π the velocities are already negative.

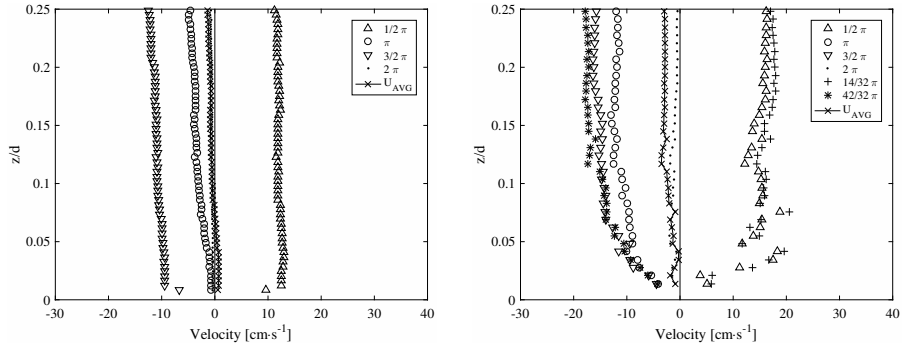

Figure 4.6: Phase averaged velocity profiles during test Reg_3 ($H = 0.0713$ m; $T = 1.01$ s): (a) position P_1; (b) position P_2. Onshore directed velocities are assumed positive.

Velocity profiles are rather symmetrical on the horizontal plane bed whereas they are strongly asymmetrical over the sloping bed. Indeed, at P_1 velocities at $1/2\ \pi$ are slightly smaller than velocities at $3\pi/2$. Averaged velocities are slightly negative throughout the profile, except close to the bottom for Reg_3 test where average velocity shows a small onshore directed steady streaming, see Longuet-Higgins (1953). Here this phenomenon is not visible due to the discarding of the data within 2 mm from the bed. At P_2 the average velocity is considerably negative to compensate the onshore wave drift whereas the maximum velocities are larger than the minimum ones throughout the water column. The velocity asymmetry is coherent with the asymmetry of the ensemble averaged waves shown in Figure 4.4, that exhibit higher and more peaked crests with smaller and broader

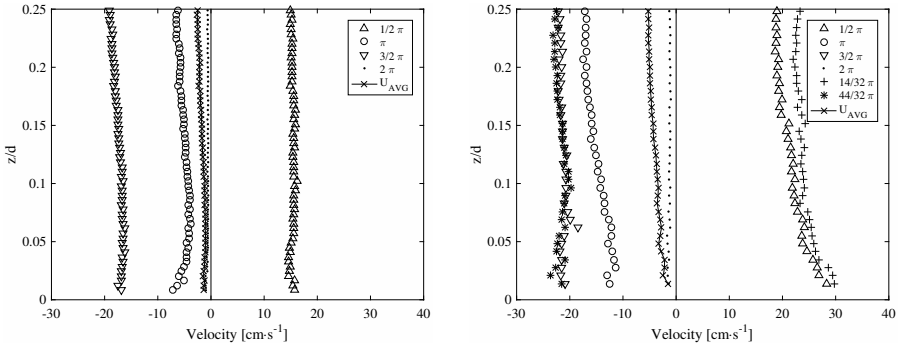

Figure 4.7: Phase averaged velocity profiles during test Reg_5 ($H = 0.0825$ m; $T = 1.01$ s): (a) position P_1; (b) position P_2. Onshore directed velocities are assumed positive.

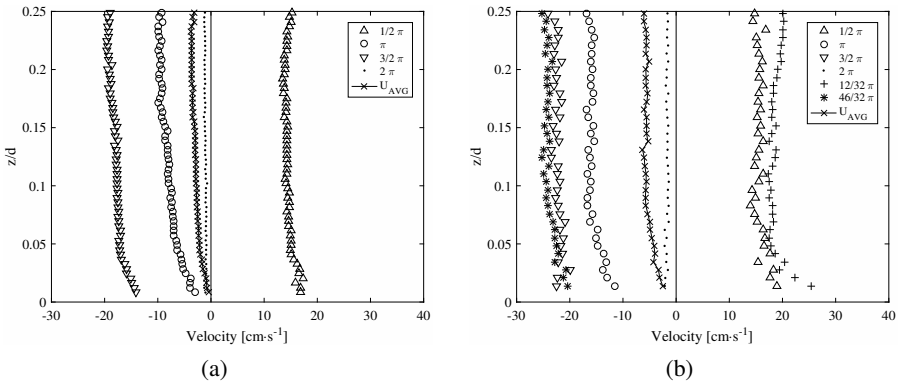

Figure 4.8: Phase averaged velocity profiles during test Reg_{11} ($H = 0.1270$ m; $T = 0.84$ s): (a) position P_1; (b) position P_2. Onshore directed velocities are assumed positive.

troughs. Following the results of Scandura et al. (2016), a greater acceleration skewness parameter $\beta = \frac{\dot{u}_{max}}{\dot{u}_{max} - \dot{u}_{min}}$, $\dot{u}_{max}$ and $\dot{u}_{min}$ being the maximum and minimum accelerations during the cycle respectively, explains the higher offshore directed average velocities achieved during Reg_{11} test ($\beta = 0.62$) when compared with Reg_5 ($\beta = 0.61$) and Reg_3 ($\beta = 0.58$). Such evidence occurred, as it can be observed in Figures 4.6, 4.7 and 4.8, where a negative period averaged velocity is present at all the elevations. This phenomenon is due to a mechanism similar to that described in Scandura (2007); Cavallaro et al. (2011) and Scandura et al. (2016). Due to the large wave asymmetry (see Figure 4.4) the intensity of turbulence is different in the two half-cycles. Therefore, the time average of the Reynolds stresses do not vanish. The mean Reynolds stresses are balanced by the mean viscous stresses due to an offshore steady current. Finally, velocity profiles acquired at position P_2 show larger velocities than those measured at position P_1, where the water is deeper. This also depends on the shoaling process that concentrates the energy flux on a smaller water depth, see Petrotta et al. (2017a,b). Velocity increase causes the growth of the turbulence intensity that, in turn, produces the thickening of the boundary layer which is clearly visible in Figure 4.6b.

4.4.2 Analysis of the morphodynamics

Bedform characteristics were also investigated starting from their first appearance to the reaching of an equilibrium condition. In this section, both the evolution and the equilibrium conditions are discussed.

Bedform evolution The ripple morphodynamics was measured both on the plane bed (position P_1) and on the sloping bed (position P_2) throughout the 30 minutes long tests Reg_4 and Reg_{10}; in all the other tests the morphodynamics was acquired only at position P_2.

As an example, results of Reg_{10} test are summarized in Figure 4.9. Ripple marks appeared after the propagation of few tens of waves and almost simultaneously on the horizontal and on the sloping bed. Within five minutes ripple length and height reached the equilibrium condition both along the plane and the sloping bed (Figure 4.9a and 4.9b respectively). The discontinuity in ripple length diagram together with the growth of mean height (25 min., position P_1) were produced by the merging of two adjacent ripples. Because of higher near bed velocities measured above the sloping bed, ripples were longer and flatter at position P_2

($\lambda_{eq} \approx 5$cm, $\eta_{eq} \approx 0.7$cm) than at position P_1 ($\lambda_{eq} \approx 3.5$cm, $\eta_{eq} \approx 0.8$ cm). At location P_1, regular waves generated symmetric ripples whose half-wavelengths did not change considerably throughout the test, see Figure 4.9c. Instead, because of wave asymmetry, after approximately 8 minutes from the start of the experiment, ripples above the sloping bed (Figure 4.9d) became asymmetric. Indeed, the offshore half-wavelength λ_{off} started growing while the onshore half wavelength λ_{on} decreased (see Figure 4.1c). Such a phenomenon led ripple onshore flanks to become steeper than offshore flanks. Notwithstanding the ripple wavelength reaches a constant value after the first minutes, the semi-half lengths tend to diverge, with λ_{on} becoming shorter and λ_{off} larger. Since the shape of the ripple profile continues to change even after the reaching of equilibrium conditions, this phenomenon has repercussion on the migration velocity.

Figures 4.9e and 4.9f show the migration velocities measured at the two test positions. As before mentioned, migration velocity was obtained as the ratio between the ripple crest displacement, recorded during each time interval, and the elapsed time interval, i.e. 1 minute. During the first 5 min. of tests, this time lapse was halved in order to better describe the ripple growth from the flat bed. At the very beginning of some tests, e.g. Reg_{10} (position P_1), ripple crests migrated alternately onshore and offshore, see Figure 4.9e, reaching the equilibrium condition after about 10 minutes from the beginning of the test. Instead, along the sloping bed, these velocities were offshore directed throughout the test and did not converge to a fixed value, see Figure 4.9f.

In most of the morphodynamic tests on the sloping bed, as a consequence of the dominant offshore steady current discussed in the previous section, the migration velocity shows negative values that decrease in time with a regular trend (Figure 4.9). More specifically, superimposing the migration velocities obtained with the same hydrodynamic conditions respectively for Reg_5 and Reg_{11}, lasting 15 minutes, to those of $Reg_4(P_2)$ and $Reg_{10}(P_2)$, lasting 30 minutes, it is possible to observe that: i) each of the two couples of curves are superimposable, thus assessing the repeatability of the experiment; ii) there is not asymptotycal tendency leading to a constant value, at least within the investigated time span (see in Figure 4.10a and 4.10b). As mentioned before, throughout the tests duration, ripples reached the equilibrium value both in terms of wavelength and height but not in terms of ripple asymmetry ($\lambda_{off}/\lambda_{on}$); the migration velocity (v_0) is naturally affected by the change of the shape of the ripple profile, preventing the reach of an asymptotical value.

In order to make the data homogeneous, a trend curve interpolating the v_0

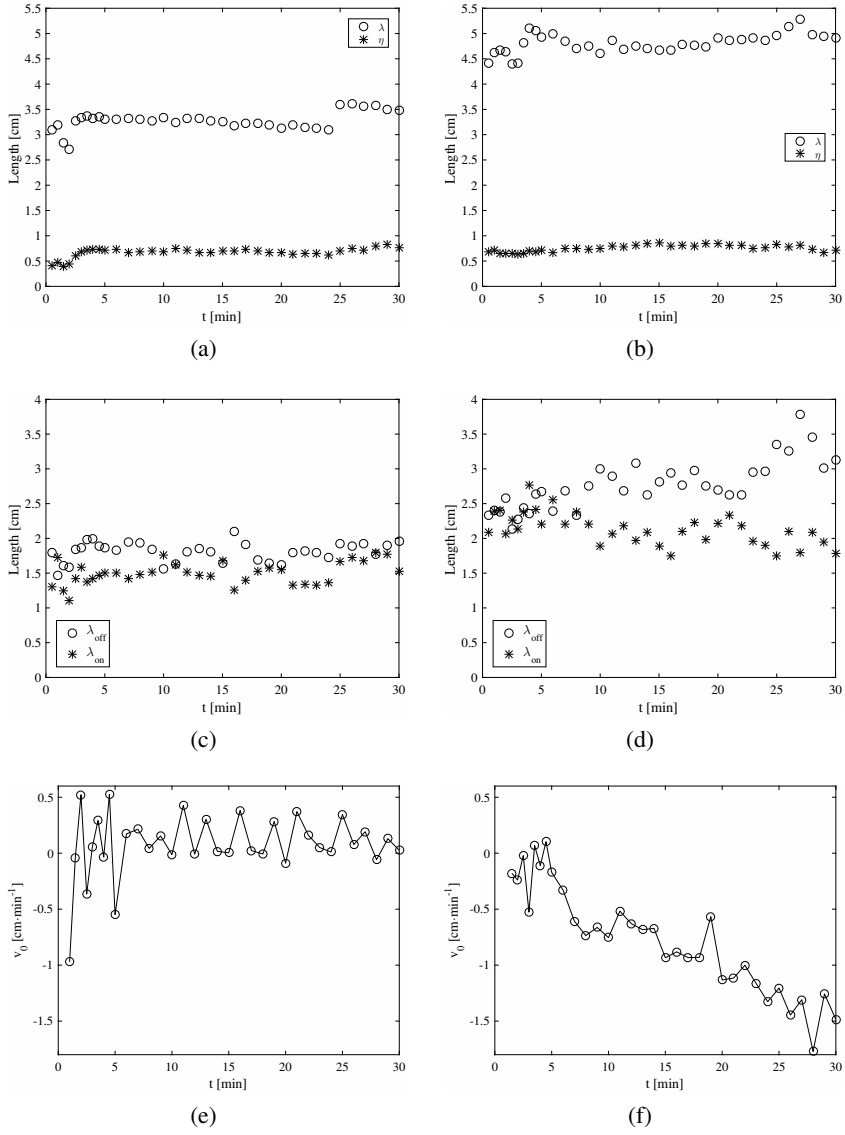

Figure 4.9: Reg_{10} test morphodynamic at P_1 (left panel) and P_2 (right panel): (a), (b) Wavelength λ and height η time evolution; (c), (d) Half-wavelengths λ_{on} and λ_{off} time evolution, see sketch in Figure 4.1c; (e), (f) Ripple crests migration velocity v_0 time.

data was superimposed, where the already mentioned quantity v_{15} indicates the estimated value at 15 minutes. In the following section these quantities, observed after 15 minutes of experiment, are referred to as equilibrium conditions and are discussed as a function of the main hydrodynamic characteristics.

It is worth recalling that Doucette and O'Donoghue (2006) analysed the evolution of a flat bed covered by coarse sand ($d_{50} = 0.44$mm) and proposed the following equation to estimate the number of flow cycles needed to reach the equilibrium n_e:

$$n_e = \exp(0.036\psi + 7.44). \tag{4.11}$$

According to the previous relation, the mobility numbers measured throughout this experimental campaign would lead to the equilibrium in time intervals of about 1-2 hours; however, during the present tests, ripple wavelength and height reached the equilibrium condition in about 10 minutes. Indeed, after such time interval, no appreciable variation of these measured quantities was observed. On the contrary, the migrating velocities showed a linear trend at least during the investigated time span.

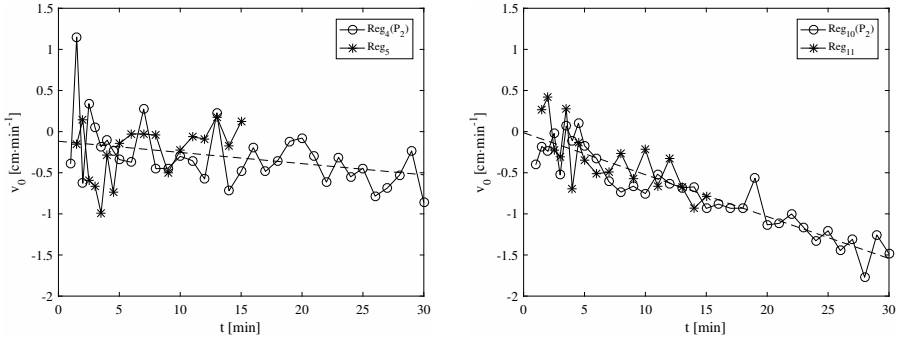

(a) (b)

Figure 4.10: Comparison between the migration velocity of ripples v_0 at position P_2: (a) Reg_4 and Reg_5 tests ($H = 0.0825$ m; $T = 1.01$ s); (b) Reg_{10} and Reg_{11} tests ($H = 0.1270$ m; $T = 0.84$ s).

The negative ripple migration is caused by a net suspended load flux that, in turn, follows the offshore directed flow (undertow), (see Fuhrman et al., 2009) which balances the onshore flux of water generated between the trough and the

crest of the asymmetric and/or skewed waves. The migration is more pronounced above the sloping bed than above the horizontal bed due to greater negative period averaged velocities. Moreover, the measured skewed and asymmetric waves lead to asymmetric bedforms.

Finally, the morphodynamic response of the sloping bed induced by the random waves propagated during Ran_2 test ($H_s = 0.063$m, $T_m = 0.8041$s) was compared to the one induced by the regular waves propagated during Reg_7 test ($H = 0.0573$m, $T = 0.8412$s), see Figure 4.11. These results are in agreement with O'Donoghue et al. (2006) who observed that, at low mobility number, dimensions of ripples triggered by regular and random waves with comparable flow orbital amplitude are similar. Neglecting local effects such as the ripple merging (at 6 min. and 8 min. after the beginning of respectively Reg_7 and Ran_2) and split (at 3 min. 30 sec. after the beginning of Reg_7) ripple wavelength and height were comparable throughout the tests, see Figure 4.11a, even though the regular wave wavelength is slightly smaller than the random wave one. At the very beginning of both tests ripples were symmetric; indeed, ripple half-wavelengths shown in Figure 4.11b were about 2 cm long for both tests. After 4 min., ripple onshore half wavelength started decreasing in Reg_7 whereas it does not change significantly in Ran_2; the offshore half wavelength slightly increase both in Ran_2 and Reg_7 tests. Such an asymmetry agrees with migration velocities plotted in Figure 4.11c. Ripples migrated mainly offshore from 1 min. up to 6 min. and became almost stable after 7 min. from the beginning of both tests.

Equilibrium conditions In Figure 4.12 the ripple characteristics at the equilibrium obtained in the present campaign, i.e. at both positions P_1 and P_2, are plotted as a function of the orbital displacement amplitude A. In particular, ripple wavelength increases for higher values of A, as the bed is subject to a larger excursion and thus the fluid particles tend to stretch the ripple wavelengths. On the other hand, ripple height does not seem to sensibly change with A.

The measured equilibrium characteristics of ripples, for the case of both regular and random waves, were compared with the results provided by some literature ripple predictors. Ripple geometry was measured both above the sloping bed (position P_2) and, in the case of few regular wave tests, also above the horizontal bed (position P_1).

More in detail, ripple wavelength, height and steepness at equilibrium were compared with the predictor models of Nielsen (1981); Van Rijn (1993); Grasmeijer and Kleinhans (2004) in Figures 4.13 and 4.14.

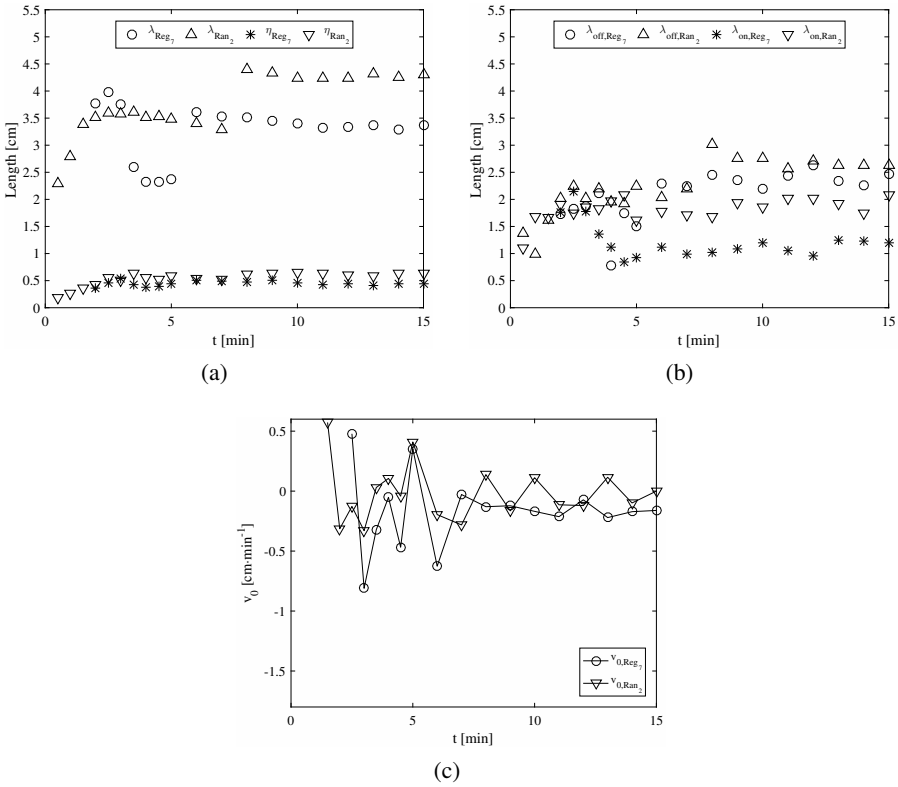

Figure 4.11: Comparison between Reg_7 test ($H = 0.0573$m, $T = 0.8412$s) and Ran_2 test ($H_s = 0.063$m, $T_m = 0.8041$s) at P_2: (a) Ripple wavelength λ and height η time evolution; (b) Ripple half-wavelengths $\lambda_{\text{on}}$and λ_{off} time evolution, see picture in Figure 4.1c; (c) Ripple crests migration velocity v_0 time evolution.

The non dimensional regular wave ripple length, reported in Figure 4.13a, is adequately estimated by the regular wave Nielsen (1981) predictor, even though with a slight overprediction providing the lowest root mean squared error ($RMSE = 0.25$) among the considered ripple predictors. Moreover, the regular wave Nielsen (1981) model fit accurately the ripple height data showed in Figure 4.13b with a $RMSE = 0.03$.

In agreement with O'Donoghue et al. (2006) and Faraci and Foti (2002), in

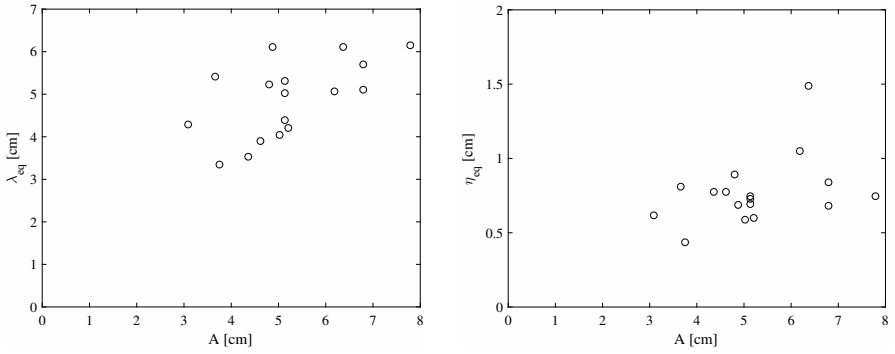

(a) (b)

Figure 4.12: Ripple wavelength λ_{eq} (a) and height η_{eq} (b) behaviour versus orbital displacement amplitude A. Data from both positions P_1 and P_2 were showed.

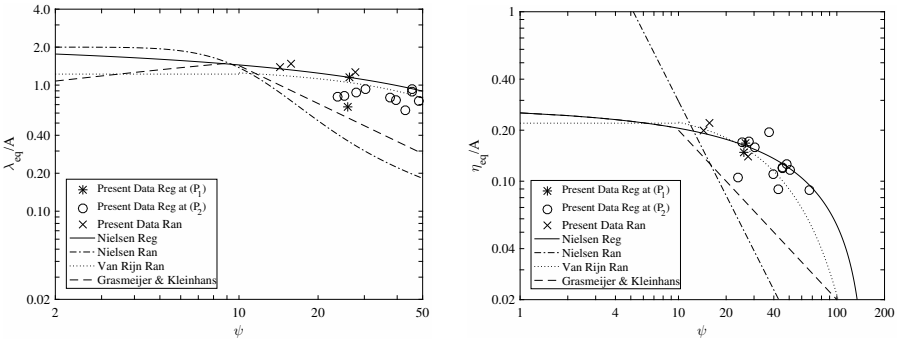

(a) (b)

Figure 4.13: Comparison of non dimensional ripple geometry data with ripple predictor models: (a) Ripple wavelength λ; (b) Ripple height η_{eq}.

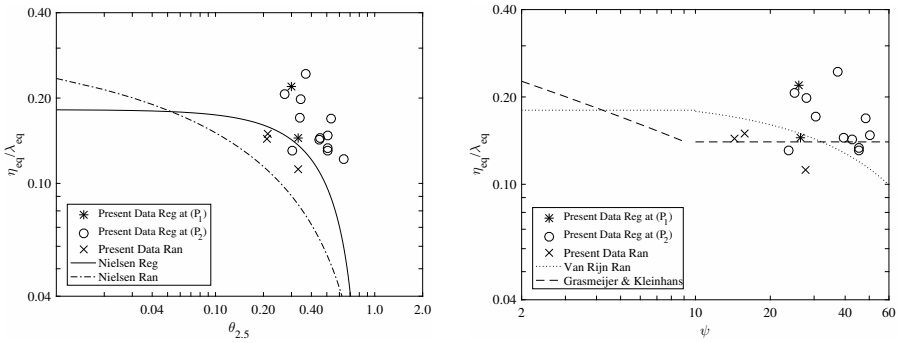

(a) (b)

Figure 4.14: Ripple steepness predictor models: (a) comparison with Nielsen (1981); (b) comparison with Grasmeijer and Kleinhans (2004) and Van Rijn (1993).

random wave cases the Nielsen (1981) model is in poor agreement with measured wavelength. Instead, the Van Rijn (1993) model predicts accurately both the non dimensional ripple length ($RMSE = 0.24$) and height ($RMSE = 0.02$).

The non dimensional ripple wavelength overestimation of the Nielsen (1981) model has an effect in ripple steepness prediction under regular waves showed in Figure 4.14a as a function of the grain roughness Shield's parameter. Indeed it is observed in general that the dimensionless steepness is underpredicted. Also the equation proposed by Grasmeijer and Kleinhans (2004) and based on the Nielsen (1981) predictor underestimates the ripple steepness in terms of the mobility number, see Figure 4.14b.

As shown in section 4.1, the sloping beach induces negative averaged velocities throughout the water depth. Such an offshore directed current makes the ripples asymmetric with the offshore half wavelength larger than the onshore one. Following Blondeaux et al. (2015), such a phenomenon can be observed relating the asymmetry index $\lambda_{\text{off}}/\lambda_{\text{on}}$ to the ratio between the averaged current velocity U_{AVG} and the near-bed orbital velocity U_0, both measured directly above the bottom boundary layer. In Figure 4.15a, data measured throughout the regular wave tests are compared with data collected by Blondeaux et al. (2015) showing the crucial role exerted by the sloping bed in ripple asymmetry. Indeed, although the

mass transport velocity did not vary considerably throughout the experiments, ripples measured above the sloping bed are noticeably asymmetric ($1.25 < \frac{\lambda_{off}}{\lambda_{on}} < 2.8$) in comparison to those in the horizontal bottom ($\frac{\lambda_{off}}{\lambda_{on}} \sim 1$). In Figure 4.15b, it is however possible to observe that $\lambda_{off}/\lambda_{on}$ shows a tendency to increase as far as the relative difference of U_{max} on U_{min} increases as well. Indeed, even though the steady drift is offshore directed and drives the ripples to migrate offshore, however, as shown in the previous section, the maximum onshore velocity is higher than the minimum one and it leads the offshore flank to increase at the expenses of the onshore one.

Finally, the migration velocity expressed in terms of the variable v_{15} is affected by the undertow. Indeed, a strong offshore directed mean velocity produces a noticeable negative migration velocity, see Figure 4.15c. In Figure 4.15c the line fitting migration velocities at position P_2 is also reported, showing a reasonable agreement with the measured data. The undertow current, which is proportional to H^2/T (Dean and Dalrymple, 1991) can induce significant migration velocities.

4.5 Fixed rippled bed

The hydrodynamics induced by waves propagating over a fixed rippled bed is discussed in the present section where the velocities measured throughout $T1$-$T9$ tests are shown.

It appears worthwhile remembering that the experimental procedure adopted throughout $T9$ test was slightly different from the one carried out during $T1$-$T8$ tests (see Chapter 4.2). Indeed, for the T_9 test, the acquisition time span was increased from 3 to 10 minutes in order to check the time convergence of both the velocity statistics, i.e. phase average, period average, standard deviation, skewness and kurtosis, and the turbulence in terms of the turbulent kinetic energy, tke, and the Reynolds stress to be analysed.

4.5.1 Analysis of the velocity data

Figure 4.16 shows the velocity measured by the third cell from the top of the control volume of the Vectrino Profiler during $T9$ test at the location L_2, $x/\lambda = 1/8$, (see Figure 4.2c). More in details, the plotted velocity correspond to an elevation of about 2.5 cm ($z/d = 0.10$).

Figure 4.16a shows the velocity acquired after 3 minutes from the wavemaker launch (see Chapter 4.2 for details on the measurements procedure) for a time span

of about 1 T. The four beams of the Vectrino Profiler measured the velocity components U, V, $W1$ and $W2$ along the direction of wave propagation x, the transverse direction y and the vertical direction z, respectively (Figure 4.1a). Throughout the experimental campaign, the velocity was analysed in order to obtain the ensemble averaged velocities showed in Figure 4.16b. The two vertical velocities $W1$ and $W2$ measured along the z direction were in good agreement throughout the test, thus, in the following, it is assumed that $W = W1$.

Figure 4.16c reports the velocity acquired within the aforementioned time span along the sloping bed and Figure 4.16d the ensemble averaged velocity. At P_2, wave shape become skewed and asymmetric and this, in turn, affects the velocity. Thus, (as shown in Figures 4.16c and 4.16d) velocity becomes asymmetric at P_2, with sharp crests and broad troughs. Moreover, it was skewed because the negative half wavelength was wider than the positive one. Note that the position along the ripple profile and the elevation from the bed were the same in both cases.

4.5.2 Convergence

As mentioned before, during experiment $T9$ the acquisition time was set to 10 minutes to analyse the velocity convergence, see Figures from 4.17 to 4.19. However, the first 3 minutes of the measured velocity were thrown out and not further examined to cut the transient condition (see Chapter 4.2). Thus, each plot illustrates by means of different markers the statistics at 1, 3, 5, 7 minutes from the beginning of the time interval considered in the analysis.

Velocities The convergence of the period averaged velocity profiles measured during $T9$ test both above the horizontal bed (ripple P_1) and the sloping bed (ripple P_2) was here analysed. In particular, Figures 4.17 and 4.18 show respectively the velocity component U in the direction of the wave propagation x and the velocity component W in the vertical direction z. Velocities were measured at nine equally spaced locations along both ripples as represented in Figure 4.2c. Nevertheless, for the sake of brevity, only the two locations L_2 ($x/\lambda = 1/8$), along the lee offshore flank, and L_8 ($x/\lambda = 7/8$), along the stoss onshore flank, were reported.

Period averaged velocities quickly reached a stable condition. Indeed, velocity profiles measured after 3, 5 and 7 minutes clearly overlap. Only profiles at 1 minute slight differ from others, particularly at low velocities. In the author's opinion, such a phenomenon was partially caused by the probe measurement errors. Indeed, before each test, it was necessary to calibrate the Vectrino Profiler velocity

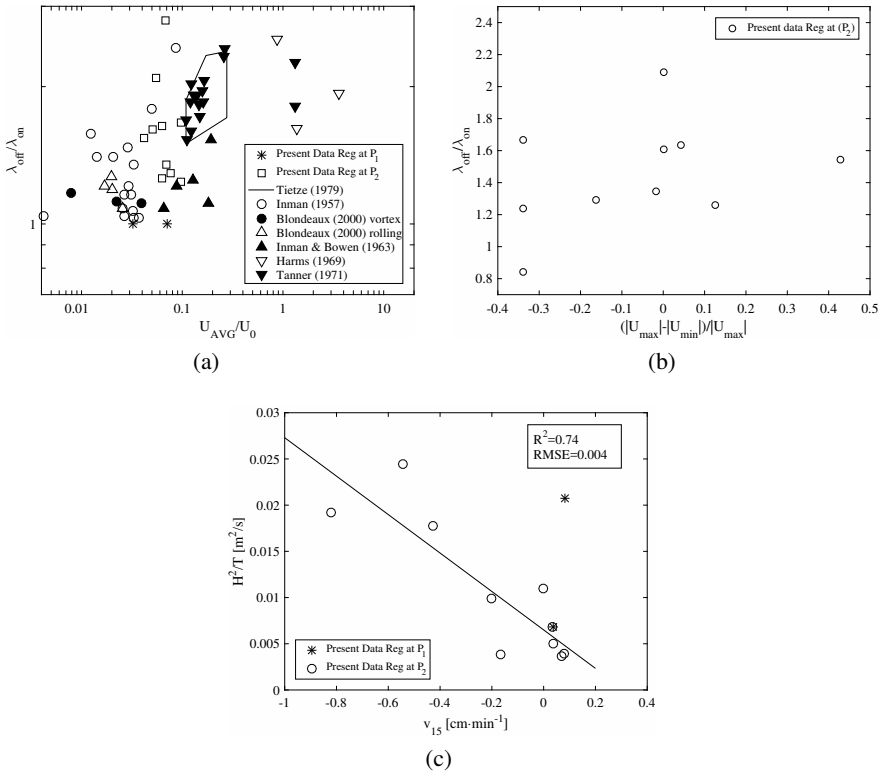

Figure 4.15: Relationship between ripple morphodynamics and flow hydrodynamics: (a) Ripple symmetry index plotted versus the ratio between outer flow averaged velocity and maximum near-bed orbital velocity; (b) Ripple symmetry index plotted versus the ratio between outer flow maximum minus minimum velocity and maximum outer flow velocity; (c) Ripple migration velocity v_{15} and H^2/T.

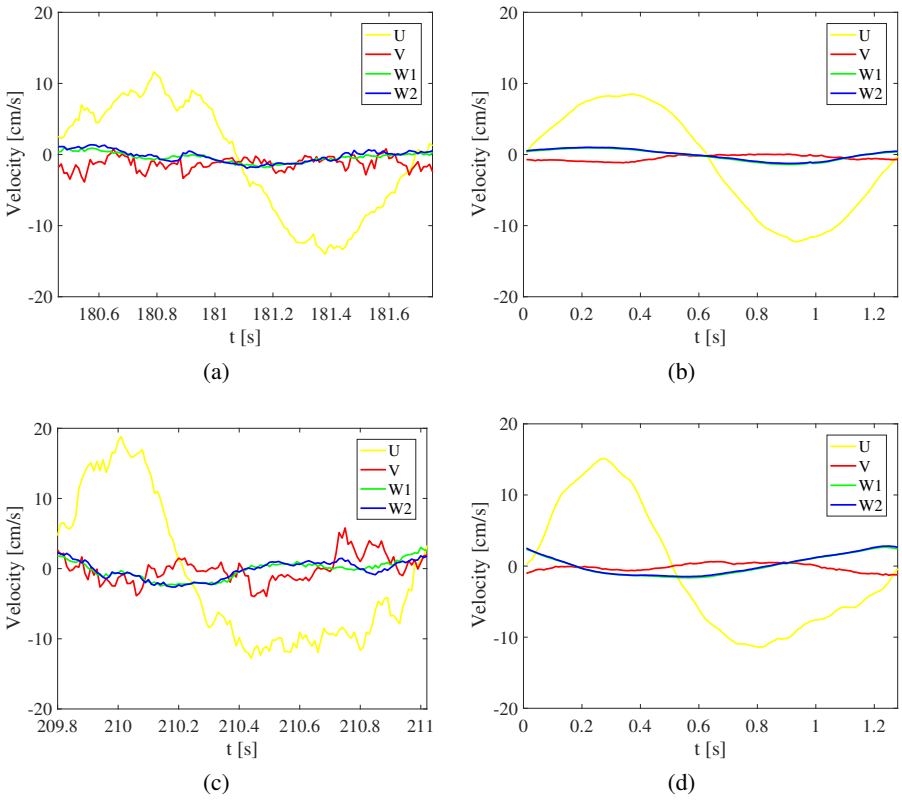

Figure 4.16: $T9$ test (H=5.86 m, T=1.26 s), velocities measured at location L_2, at the elevation $z/d = 0.10$: a) Vectrino Profiler velocity just after the transient condition (see section 4.2) at P_1; b) time averaged velocity at P_1; c) Vectrino Profiler velocity at P_2; d) time averaged velocity at P_2.

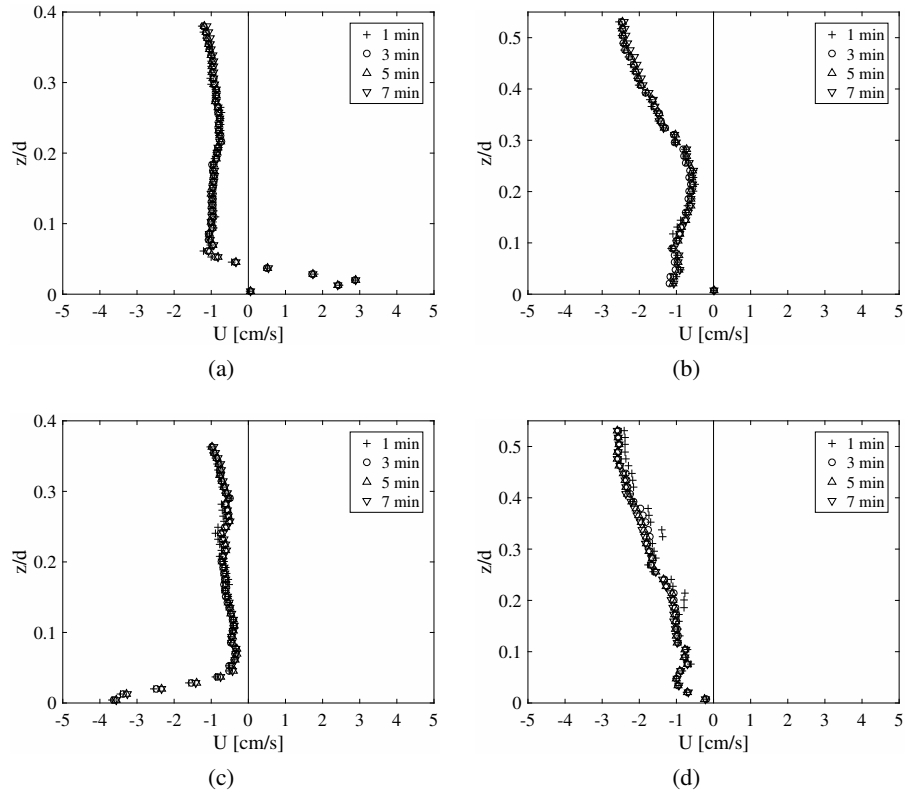

Figure 4.17: $T9$ test (H=5.86 m, T=1.26 s), period averaged U velocity profiles convergence: a) P_1, L_2; b) P_2, L_2; c) P_1, L_8; b) P_2, L_8; (see Figure 4.2c).

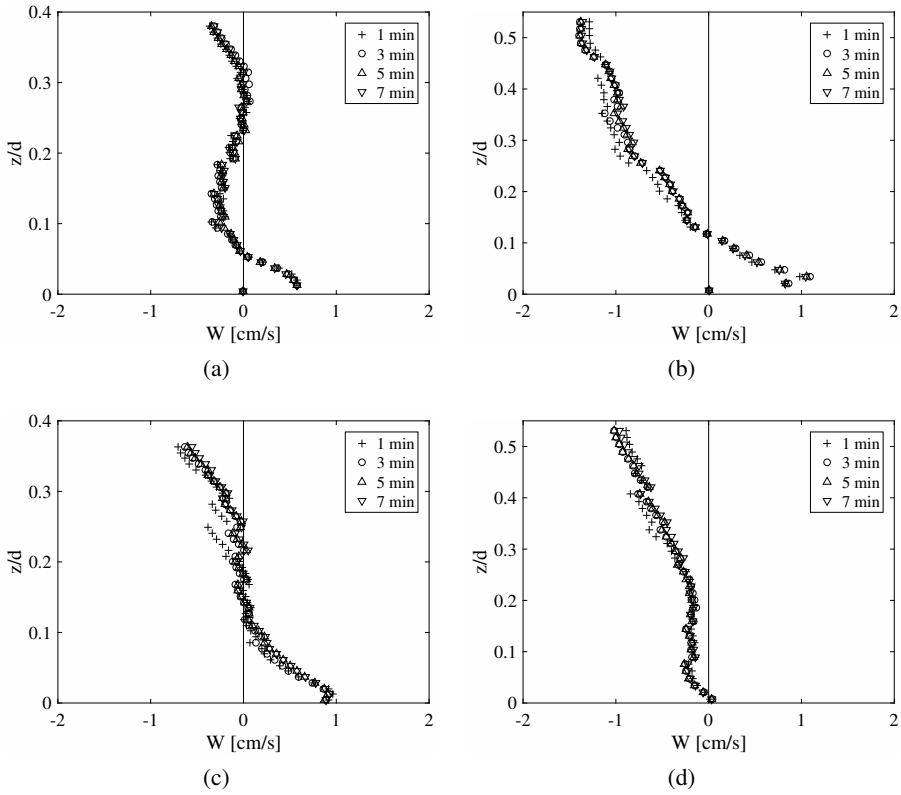

Figure 4.18: $T9$ test (H=5.86 m, T=1.26 s), period averaged W velocity profiles convergence: a) P_1, L_2; b) P_2, L_2; c) P_1, L_8; b) P_2, L_8; (see Figure 4.2c).

range parameter. In particular, throughout $T9$ test, the instrument was calibrated to accurately measure velocities of about 0.1-0.2 m/s. Nevertheless, close to the zero crossing, velocities were ten or more times smaller (see Figure 4.17d, 4.18b, 4.18c and 4.18d), thus decreasing the Vectrino Profiler reliability. In such conditions, some the random measurement errors can appear within the measured velocities. The influence of these spikes on the phase averaged velocity can be considerably reduced by increasing the acquisition time interval to at least 2 minutes.

Above the ripple offshore flank L_2, outer flow velocities ($z/d > 0.05$) in the direction of the wave propagation x were slightly negative ($U < 1$ cm/s) at both P_1, L_2 and P_1, L_8, Figures 4.17a and 4.17c. It could be observed that the rippled bottom caused the appearance of recirculating cells which affected considerably the near-bed hydrodynamics. These, together with the Longuet-Higgins steady streaming (Longuet-Higgins, 1953) and the asymmetry steady streaming (Scandura, 2007), caused near-bed velocities to be onshore directed above the ripple offshore flank L_2 and offshore directed above ripple onshore flank L_8.

Moving to the sloping bed, an undertow current could be observed both near bed, where a velocity overshoot occurred above ripple onshore flank (Figure 4.17d), and above $z/d > 0.25$ at both locations, Figures 4.17b and 4.17d). Such a return current extended to the horizontal bed and caused the period averaged outer flow velocities to become negative, as previously observed.

The presence of recirculating cells at P_1 was confirmed by the velocity profiles in the vertical direction z. At both locations, close to the bottom, velocities were considerably positive, i.e directed upward. Moving away from the bottom, velocities decreased. More in detail, above the ripple offshore flank, at the elevation $z/d = 0.05$, the centre of the recirculating cell, where both U and W were close to zero, presumably occurred. The cell extended up to $z/d = 0.25$ where vertical velocities become negligible and horizontal velocities were offshore directed due to the undertow, Figures 4.17a and 4.18a. At L_8 only the lower part of the recirculating cell is clearly visible. Indeed above $z/d = 0.1$ $W \simeq 0$, Figure 4.18c. At P_2, W velocities were strongly affected by the downward flux which did not allow velocities to become positive above the offshore flank, Figure 4.18d. The downward flux had to turn upward due to the effect of the ripple offshore flank which vanished at $z/d > 0.1$, Figure 4.18b.

Velocity statistics Figure 4.19 shows standard deviation S, skewness s and kurtosis k of the velocity profiles at both positions P_1 and P_2. The standard deviation

quantify the amount of dispersion of velocities around their mean value. The standard deviation for a standard normal distribution is one. The skewness is a measure of the symmetry of the velocity distribution. The skewness for a normal distribution is zero; negative values indicate that the left tail is longer than the right tail, finally, positive values indicate that the right tail is longer than the left tail. Kurtosis is a measure of whether the data are heavy-tailed or light-tailed relative to a normal distribution. That is, data sets with high kurtosis tend to have heavy tails, or outliers. Data sets with low kurtosis tend to have light tails, or lack of outliers. The kurtosis for a standard normal distribution is equal to three.

Given u_i the observed velocity and $\overline{u}$ its period averaged value, the aforementioned statistics could be expressed as:

$$S = \sqrt{\frac{1}{n-1}\sum_{i=1}^{n}(u_i-\overline{u})^2} \tag{4.12}$$

$$s = \frac{\frac{1}{n}\sum_{i=1}^{n}(u_i-\overline{u})^3}{\left(\sqrt{\frac{1}{n}\sum_{i=1}^{n}(u_i-\overline{u})^2}\right)^3} \tag{4.13}$$

$$k = \frac{\frac{1}{n}\sum_{i=1}^{n}(u_i-\overline{u})^4}{\left(\frac{1}{n}\sum_{i=1}^{n}(u_i-\overline{u})^2\right)^2} \tag{4.14}$$

The standard deviation converged to a stable value in less than 3 minutes almost throughout the investigated water depth both along the horizontal bed (Figure 4.19a) and on the sloping bed (Figure 4.19b). At both positions, the standard deviation of the outer flow velocities was pretty constant between $z/d = 0.4$ and $z/d = 0.1$ where velocities started to increase due to the undertow. Moreover, standard deviation increased near the bottom ($z/d < 0.1$) due to the velocity overshoot related to the Longuet-Higgins steady streaming measured above the ripple stoss flank.

In the central part of the profiles, the standard deviation was smaller at P_1 than at P_2 where the orbital velocity increased due to the wave asymmetry. However, the steady offshore directed currents increased wave skewness, thus the negative half-period became considerably longer than the positive one and, in turn, the period

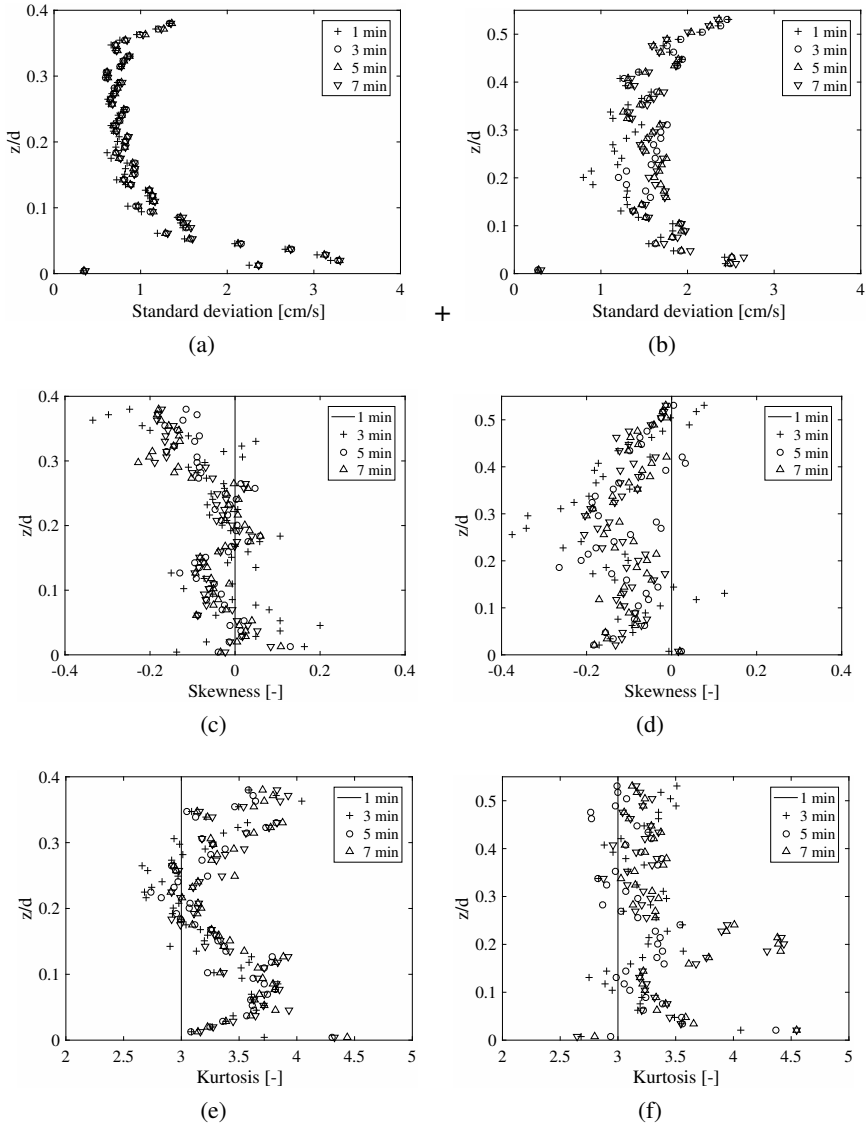

Figure 4.19: $T9$ test (H=5.86 m, T=1.26 s), velocity statistics profiles convergence: a) standard deviation at P_1, L_2; b) standard deviation at P_2, L_2; c) skewness at P_1, L_2; d) skewness at P_2, L_2; e) kurtosis at P_1, L_2; f) kurtosis at P_2, L_2.

averaged velocity $\overline{u}$ became negative. Since the negative half-period was considerably longer than the positive one the dispersion of the velocities from their mean value decreased.

Both skewness and kurtosis required 5 minutes to reach a stable condition. The depth averaged value of the skewness profiles was about zero along the horizontal bed (Figure 4.19c) and about -0.1 along the sloping bed (Figure 4.19d). This occurrence confirms that ensemble averaged velocity was rather symmetric at P_1, whereas it became asymmetric at P_2. There, the velocity distribution has a long negative tail, throughout the water depth, whereas at P_1 this phenomenon occurs only above $z/d > 0.3$ due to the undertow.

Any univariate normal distribution has its kurtosis equal to three, Figure 4.19e shows that the kurtosis varies between 3 and 3.5 thus it take values of k close to those of a normal distribution. At P_1 a value of 3 was reached at the bottom and at $z/d \sim 0.2$. Elsewhere, kurtosis was higher, thus higher velocities (in modulus) were reached more frequently due to the asymmetry steady streaming at the bottom and the undertow at higher elevation along the water column. At P_2, the skewed and asymmetric wave produced the increase the high velocities recurrence throughout the water depth, thus, kurtosis was almost constantly equal to 3.3, see Figure 4.19f. Furthermore, few peaks appeared within kurtosis profiles, particularly at P_2. This occurrence was probably caused by the presence of few outliers in the Vectrino Profiler data which were not successfully thrown out within data processing.

4.5.3 Phase analysis

Figures 4.20 and 4.21 show the phase averaged velocity U and W profiles above the two ripples P_1 and P_2, respectively. Nine equally spaced locations were examined, but for the sake of brevity, only profiles at the aforementioned L_2 and L_8 locations were here reported. Figures 4.22 and 4.23 show the phase averaged turbulent kinetic energy $tke = (u'^2 + v'^2 + w'^2)/2$ and the phase averaged Reynolds stress $\overline{u'v'}$ profiles above the two ripple flanks, being u', v' and w' the turbulent velocities respectively along x, y and z. Turbulent fluctuations were measured along the two ripples P_1 and P_2 during the experiment T_9. Sixty-four equally spaced phases per period were identified but only six phases were sketched, namely $1/2\ \pi$, π, $3\pi/2$ and 2π, together with the phases where the depth-averaged velocity or fluctuation reached its maximum and its minimum. The period-averaged profile is also plotted.

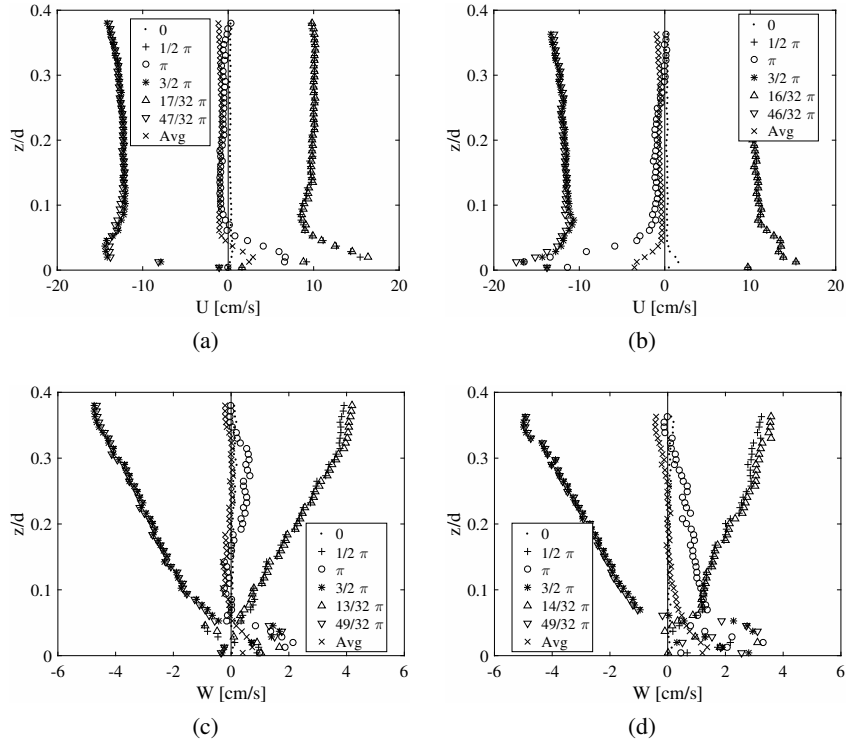

Figure 4.20: $T9$ test (H=5.86 m, T=1.26 s), velocity phase analysis at P_1: a) U velocity profile at L_2; b) U velocity profile at L_8; c) W velocity profile at L_2; d) W velocity profile at L_8.

U and W velocity profiles are rather symmetrical above the horizontal bed both at L_2 and at L_8. Looking at P_1 profiles, Figures 4.20 (a-d), it could be observed that the modulus of the velocity at $1/2\ \pi$ phase was similar to the modulus of the velocity at $3/2\ \pi$ phase throughout the water depth. Moreover, the U depth-averaged velocity reached its maximum at $1/2\ \pi$ phase (Figure 4.20b) or slight after (Figure 4.20a) and its minimum slight before $3/2\ \pi$ phase. The W depth-averaged velocity reached its maximum slight before $1/2\ \pi$ phase and its minimum slight after $3/2\ \pi$ phase, Figures 4.20c and 4.20d. The vertical component of the velocity was slight more asymmetrical than the horizontal component. The profile symmetry was confirmed by looking at the velocities measured at 0 and at

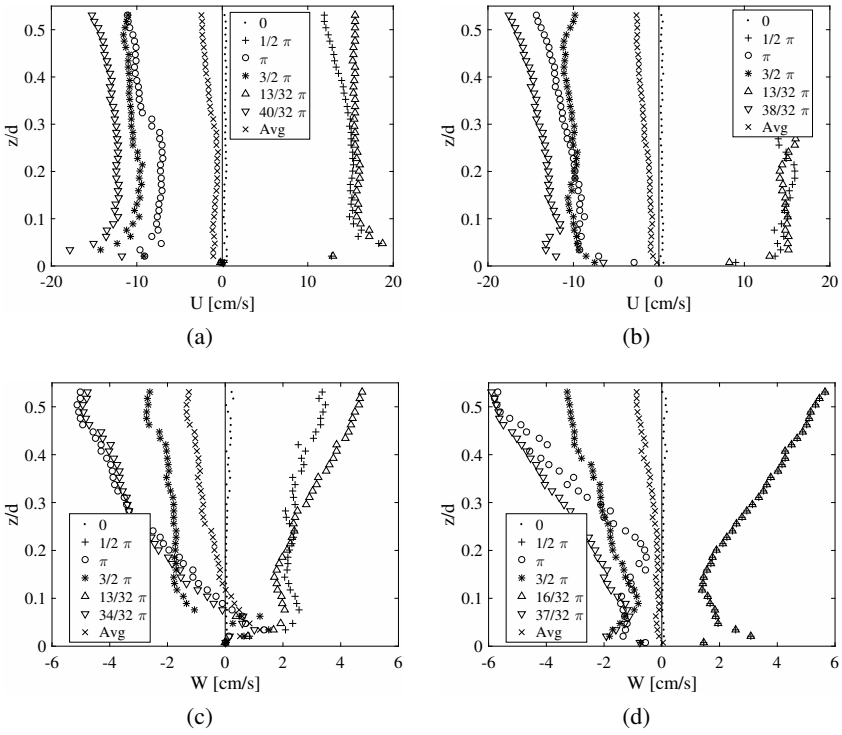

Figure 4.21: $T9$ test (H=5.86 m, T=1.26 s), velocity phase analysis at P_2: a) U velocity profile at L_2; b) U velocity profile at L_8; c) W velocity profile at L_2; d) W velocity profile at L_8.

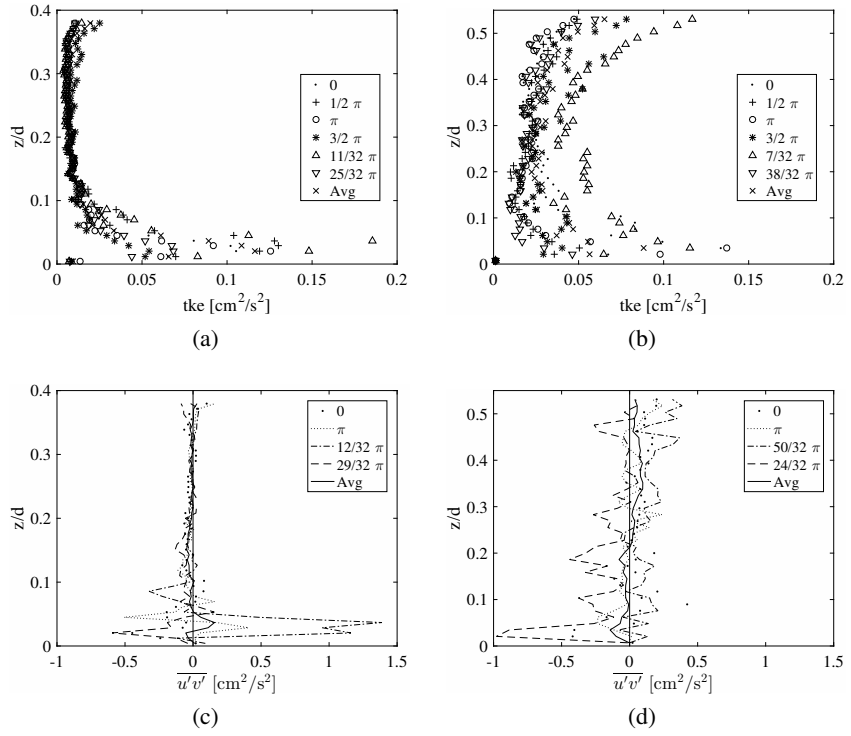

Figure 4.22: $T9$ test (H=5.86 m, T=1.26 s), turbulence phase analysis: a) tke profile at P_1, L_2; b) tke profile at P_2, L_2; c) Reynolds stress profile at P_1, L_2; d) Reynolds stress profile at P_2, L_2.

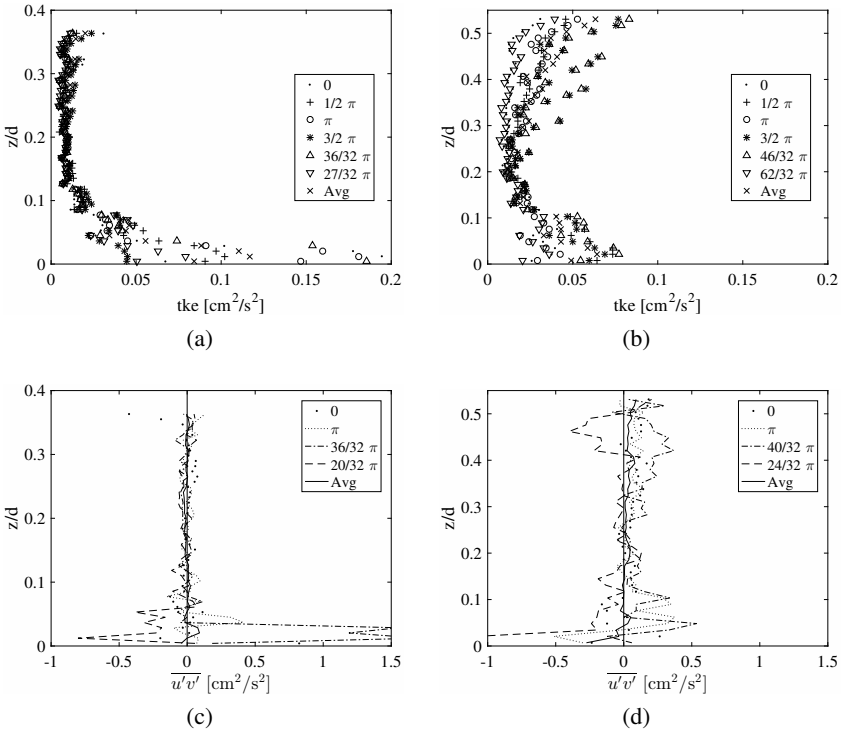

Figure 4.23: $T9$ test (H=5.86 m, T=1.26 s), turbulence phase analysis: a) tke profile at P_1, L_8; b) tke profile at P_2, L_8; c) Reynolds stress profile at P_1, L_8; d) Reynolds stress profile at P_2, L_8.

π phases. Except near the bottom where ripple shape made flow asymmetric, both U and W velocity profiles were negligible at 0 phase and smaller than 1 cm/s at π phase throughout the water depth.

At the bottom ($z/d < 0.1$), U velocity profiles at π phase exhibit a positive overshoot above ripple offshore side and a negative overshoot above ripple onshore side. Near the bottom, the upward directed W velocities caused the sediment lifting up to the aforementioned recirculating cells, Section 4.5.2. Moreover, these velocities approach to zero at the bottom due to the no-slip boundary condition which does not allow the flow separation.

According to the continuity principle, the onshore directed velocities decreased moving along the ripple lee flank, and increased, moving along the ripple stoss flank. Thus, velocities at phase $1/2\ \pi$ were bigger at L_8 than at L_2; analogously, velocities at phase $3/2\ \pi$ were bigger at L_2 than at L_8, Figures 4.20a and 4.20b.

Above the sloping bed, Figures 4.21 (a-d), U and W velocity profiles were skewed at both locations L_2 and L_8. The highest positive depth averaged U velocities were early reached, i.e. at $13/32\ \pi$ phase, at both locations (Figures 4.21a and 4.21b). As well, the highest negative depth averaged U velocities were early reached respectively at $40/32\ \pi$ and at $38/32\ \pi$. The vertical velocity component early showed both the maximum and the minimum depth averaged velocity profiles (Figures 4.20d and 4.21d); only above the onshore ripple flank, the maximum depth averaged velocity was reached exactly at $1/2\ \pi$, Figure 4.21d.

Nevertheless, the positive half period of the ensemble averaged velocity was considerably shorter than the negative half period throughout the water depth. Indeed, at P_2 both U and W velocity profiles were considerably negative at π phase, Figures 4.21 (a-d). However, at L_2, the recirculating cells produced an upward velocity component throughout the period close to the bottom, Figure 4.20d. Finally, the wave asymmetry triggered by the sloping bed, made the onshore directed U component bigger in modulus at the phase of the maximum depth averaged velocity than the one at the phase of the minimum depth averaged velocity. Thus, producing a higher boundary layer within the accelerating phase than within the decelerating phase.

The turbulent kinetic energy varied from 0 to 0.2 cm^2/s^2 above the offshore flank (L_2 location) of both ripples (Figures 4.22a and 4.22b). Turbulence was negligible at the bottom due to the no-slip condition then it increased due to the vorticity generated by the rippled bed. Moving away from the bottom, turbulence decreased. More in detail, at P_1 turbulence reached values close to zero moving

upward from $z/d = 0.1$; at P_2, the flow was more turbulent due to the wave breaking which occurred just up ahead in the channel. Thus, turbulence profiles exhibit a positive gradient at $z/d = 0.55$. Turbulence generated by wave breaking can also explain why in P_2 there was a greater difference between the tke profiles in different phases than in P_1. Furthermore, at both positions, tke reached its maximum when the flow was onshore directed, i.e. at $11/32\ \pi$ and at $7/32\ \pi$, respectively. Such a phenomenon is one of the reasons why an offshore directed asymmetry steady streaming can be generated (Scandura, 2007).

The Reynolds stresses measured at both positions P_1 and P_2 (L_2 location) were respectively reported in Figures 4.22c and 4.22d. Above the horizontal bed, Reynolds stresses at the bottom varied from -0.5 to 1.4 cm^2/s^2. As expected, the phase averaged Reynolds stress was negative when the velocity gradient was positive and vice-versa. At distances from the bottom larger than 3 cm approximately ($z/d > 0.1$) $\overline{u'v'}$ became negligible at P_1. Instead, at the sloping bed Reynolds stresses varied from -1 to 0.4 cm^2/s^2 and did not approach zero throughout the investigated water depth. Such phenomenon occurred because of the higher velocities caused by the decreasing of the water depth (according to the mass conservation law).

Looking at both tke and Reynolds stress profiles, it is easy to see that the sloping bed did not cause an increase of the near bed turbulence. Instead, turbulence extended throughout the water depth, thus, producing a considerable flow stirring. Such a phenomenon could explain the ripple offshore migration observed during the moveable bed experiment, see Chapter 4.4.1. Turbulence produced the flow stirring which, in turn, raised the suspended sediment far from the bottom. Then, because of the undertow, an offshore sediment transport was generated which was higher than the onshore directed transport at the bottom and caused the measured ripple offshore migration.

The turbulent kinetic energy together with the Reynolds stress measured at location L_8 were respectively reported in Figures 4.23a, 4.23b and 4.23c, 4.23d. No considerable differences could be observed with respect to the offshore ripple flank.

4.5.4 Spatial analysis

Figures 4.24 and 4.25 show the velocity field between two adjacent ripple crests, measured throughout experiment $T3$. Both U and W velocity components are here considered. Positive, onshore flow is directed to the right. The stoss slope of the

ripple is the onshore slope (i.e., the right side of the image) and the lee slope is the offshore slope.

Following Van der Werf et al. (2007), eight phases per period were plotted in Figures 4.24 (a–h) and 4.25 (a–h):

- (a), phase 0: this phase is close to the off-onshore flow reversal, thus the free-stream velocities were close to zero.

- (b), phase $1/4\ \pi$: free stream was accelerating onshore, thus velocities were onshore directed throughout the water column. Ripple shape affected near bed velocities. More in detail, moving from the ripple offshore crest to the ripple trough (locations from L_1 to L_5) near bed velocities decreased whereas, moving from the ripple trough to the ripple onshore crest (locations from L_5 to L_9) near bed velocities increased, see Figures 4.24 (a–h). At the sloping bed, this phenomenon can be distinguished only above the ripple stoss side, see Figures 4.25 (a–h).

- (c), phase $1/2\ \pi$: the horizontal component of the free stream velocity is close to its onshore maximum. More specifically, at P_2 maximum horizontal velocities occurred few instants before phase $1/2\ \pi$ due to the wave asymmetry. At both positions, the highest velocities were measured at about 1-2 cm from the bottom where a velocity overshooting occurred. Moreover, the vertical component of the velocity often showed its maximum from $2/32\pi$ to $3/32\pi$ phases before.

- (d), phase $3/4\ \pi$: free-stream velocity is decelerating. At P_2 due to the velocity skewness, velocity profiles were close to the flow reversal.

- (e), phase π: this phase is close to on-offshore flow reversal. The free-stream velocity was weak, instead, near the bottom the velocities exhibit a considerable overshooting which was directed to the ripple trough above both flanks in accordance with the recirculating cells observed throughout the Paragraph 4.5.3. The return current made the velocity profiles at P_2 offshore directed at all the inspected locations.

- (f), phase $5/4\ \pi$: the free stream was accelerating offshore. Near the bed, the offshore directed velocities decreased moving from the ripple P_2 onshore crest (from $x/\lambda = 7/8$ at P_1) to the ripple trough and increased moving from the ripple trough to the ripple offshore crest.

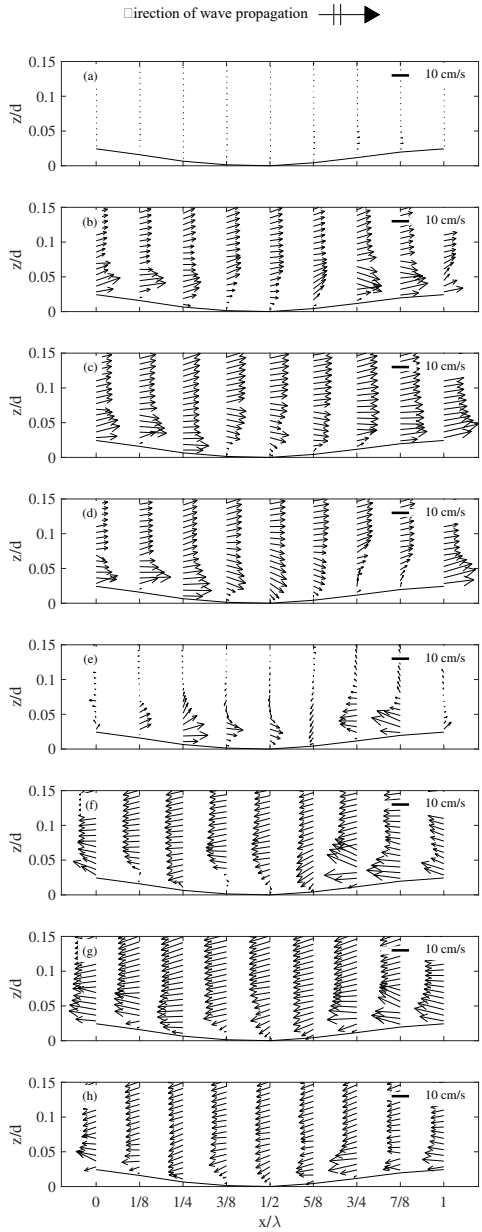

Figure 4.24: $T9$ test (H=5.86 m, T=1.26 s), velocity field along ripple P_1 at eight phases: a) 0; b) $1/4\ \pi$; c) $1/2\ \pi$; d) $3/4\ \pi$; e) π; f) $5/4\ \pi$; g) $3/2\ \pi$; h) $7/4\ \pi$.

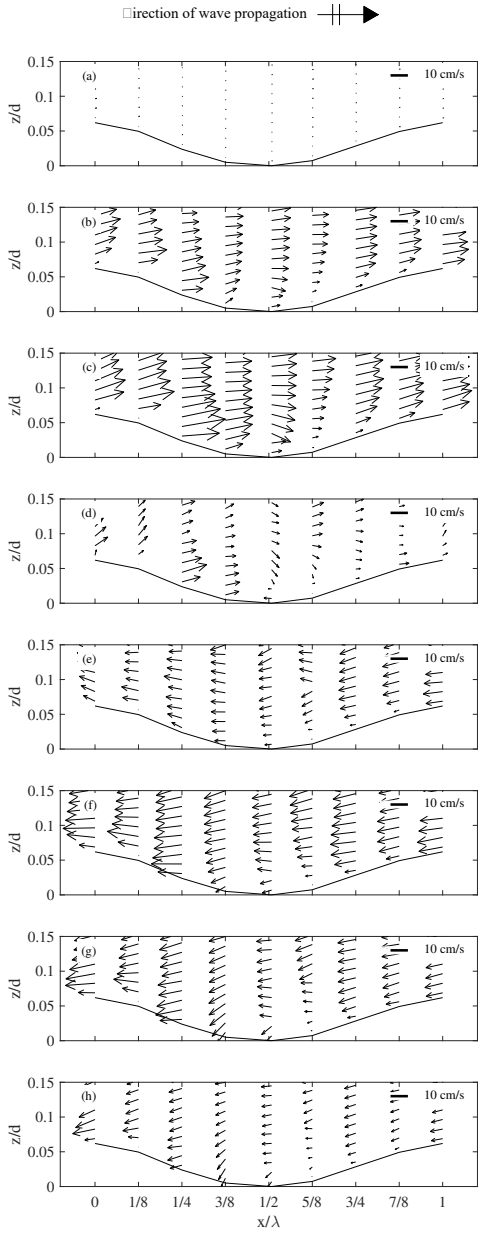

Figure 4.25: $T9$ test (H=5.86 m, T=1.26 s), velocity field along ripple P_2 at eight phases: a) 0; b) $1/4\ \pi$; c) $1/2\ \pi$; d) $3/4\ \pi$; e) π; f) $5/4\ \pi$; g) $3/2\ \pi$; h) $7/4\ \pi$.

- (g), phase $3/2\ \pi$: the free stream velocity is close to its offshore maximum. More specifically it occurred few instants before for the U component and few instants after for the W component. At P_2, both components reached the minimum several phases before.
- (h), phase $7/4\ \pi$: offshore free-stream velocity started decelerating.

4.6 Discussion

An experimental campaign was performed in order to investigate the hydrodynamics induced by sea waves propagating over a sloping sandy beach.

The campaign consisted of two parts. Throughout the first part, the morphodynamic evolution of the bed was examined by means of a structured light technique which allowed to determine the time development of the ripple height, wavelength and migration rate. Both the morphodynamic and hydrodynamics were measured at two sections, the first one located above the horizontal bed and the second one above the sloping bed. The second part of the campaign aimed to look into the near bottom flow field and its modifications induced by ripples. Bedforms were preliminarily fixed by a thin layer of concrete and inhibited to migrate, thus allowing detailed velocity measurements along the two ripples wavelengths. Throughout the campaign, approaching to the sloping bottom, waves become strongly asymmetrical, with flat, wide troughs and sharp crests as measured by the resistive wave gauges deployed into the flume.

Throughout the moveable bed experiments, ripples started to appear after few wave cycles from the beginning of tests. The sloping bed strongly affected both the ripple shape and the migration velocity. Indeed, ripples measured at the sloping bed were strongly asymmetric with offshore half-wavelengths often larger than onshore ones; in addition, ripples were longer and flatter than the ones measured above the horizontal plane bed. The ripple asymmetry, that makes bedforms to lean towards the beach, was driven by the higher value of U_{max} with respect to U_{min} as measured during both parts of the campaign. Moreover, after a brief transient where ripples migrate alternatively in both directions, ripples measured on the horizontal plane bed quickly converged at an equilibrium value, where the migration velocity was negligible. Instead, the migration velocity of ripples measured above the sloping bed was usually offshore directed throughout the duration of the tests and did not reach an equilibrium value in the investigated time span. This occurred because, as soon as ripples start to migrate, the steady component originated

by recirculation cells was added to the offshore directed mass transport velocity, giving rise to an increase in the migration velocity itself. The ripple shape and migration velocities generated by random waves propagating on the sloping beach were similar to the ones triggered by regular waves energetically equivalent to the significant random waves.

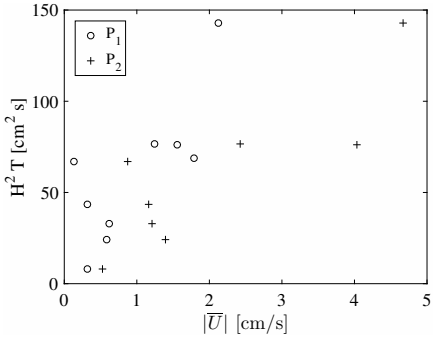

Figure 4.26: Mass transport velocity as a function of the depth and period averaged velocity at location L_5.

Finally, the effects of the sloping beach on the ripple half-wavelengths and asymmetry are in a fairly good agreement with several ripple predictors. In particular, at the equilibrium, the ripple predictors developed for horizontal beds well describe the sloping bed morphodynamics; thus, they correctly predict the ripple height, slightly overestimate the ripple wavelength triggered by regular waves and accurately describe the random wave wavelength.

Measurements carried out throughout the second part of the campaign could shed a light on the bedforms morphodynamics. Above the horizontal bed, ripples considerably affected the phase averaged velocity profiles. Indeed, velocities measured far from the bottom, where the flow approaches the irrotational condition, were close to zero at both 0 and π phases. Instead, near the bottom, ripple lee side triggered the appearance of the onshore directed Longuet-Higgins steady streaming, whereas ripple stoss side gave rise to an offshore directed steady streaming. These two opposite fluxes were balanced, thus producing symmetric ripples which quickly reached an equilibrium position.

Instead, the sloping bed caused the appearance of a strong return current which, interacting with the rippled bottom, made the flow turbulence non-negligible within the investigated water depth, particularly when velocities were onshore directed. Turbulence caused a considerable flow stirring which, above a non-cohesive bed,

could lift the sediment up in the water column. Then, sediments were driven offshore by the undertow current which caused the observed offshore directed ripple migration.

At the sloping bed, the presence of the return current was observed throughout the experimental campaign. More in detail, Figure 4.26 shows the mass transport velocity, which is proportional to H^2T (see Dean and Dalrymple, 1991), as a function of the depth and period averaged velocity measured above the ripple trough (location L_5). As expected, velocities measured above the sloping bed P_2 were everywhere bigger than velocities measured above the horizontal bed P_1.

5 Large scale wave flume experiments

The *Canal d'Invesitgació I Experimentació Marítima* - Maritime Research and Experimentation Wave Flume (ICTS-CIEM) of the Laboratori d'Enginyeria Marítima (LIM) of the Universitat Politècnica de Catalunya (UPC) in Barcelona is 100 m long, 3 m wide, and 4.5 m deep, see Figure 5.1. Within the wave flume, waves are generated by means of a wedge-type wave paddle with a maximum stroke of 2 m. There are five 0.9 m wide glass windows fitted at regular intervals along the flume test section and one 5 m wide glass window near the onshore end of the flume allowing for visual observations and non-intrusive optical measurement techniques. The water depth at the wave paddle can be varied between 2 and 3 m.

The adopted reference system lies on the still water level (swl), 2.65 m above the bottom of the flume: the origin is at the wave paddle in rest position; the x-axis is directed along the flume and positive when going towards the shoreline; whereas the z axis is directed vertically and positive upwards; the y coordinate has its origin on the right side wall of the flume when facing the beach and is positive toward the center of the flume.

The beach profile for the fixed bed was created by running a regular wave ($H = 0.85$ m $T = 4.0$ s) for 3 h over a mobile sand bed profile (sand grain diameter $d_{50} = 0.25$ mm), which initially consisted of a 1:10 offshore slope raised to 1.35 m above the flume floor, followed by a 18 m long horizontal bed, and terminated by a nonmobile straight sloping beach, (see van der Zanden, 2016). The rather long horizontal section was chosen in order to ensure that bed slope effects in the inner surf zone or swash zone processes did not affect the hydrodynamics around the bar. After 3 h of waves a breaker bar was created that was sufficiently high to ensure a strongly plunging wave. The resulting fixed bed profile consisted of a 1:12 offshore slope, which begins at x=34.2 m and ends near the bar crest at x=54.3 m, a 0.6 m high breaker bar (measured from crest to trough), with a lee-side slope of approximately 1:4, followed by a 10 m long 1:125 slope and terminated by a fixed

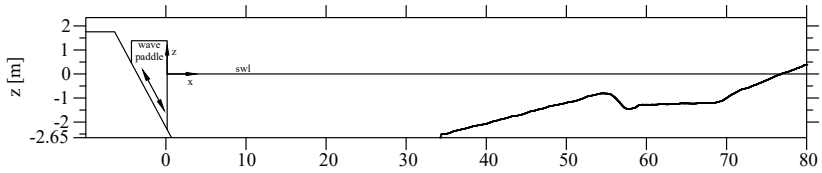

(a)

(b)

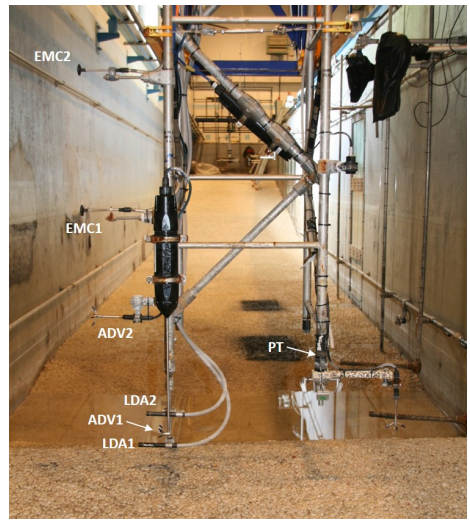

(c)

Figure 5.1: Wave flume of Polytechnic University of Catalunya: (a) sketch of the bed profile, (b) photo of the bed roughness, (c) photo of the mobile frame positioned above the bar crest including the measurement instruments.

1:7 sloping profile. The concrete surface was covered by a layer of gravel with $d_{50} = 9 \cdot 10^{-3}$ m glued onto the surface to increase and homogenize the roughness, see Figure 4.2b.

5.1 Measurements

The flow field above the bar was measured by two Vectrino acoustic velocimeters (ADV), two laser anemometers (LDA), one acoustic Doppler velocity Profiler (ADVP, described fully in Hurther et al. (2011)) and a Vectrino Profiler (VP). The results here presented are based on measurements obtained using LDAs and ADVs. Data measured by means of ADVP were used to replace some missing data from LDAs and ADVs. The LDAs measured the u and the w velocity components at a sampling frequency of 300 Hz on average. These rates varied depending on the concentration of seeding particles and on the fluid velocity. The ADVs and the ADVP measured the three velocity components at a sampling frequency of 100 Hz and 25 Hz respectively. These instruments were deployed from a frame attached to a carriage placed on tracks at the top of the wave flume (see Figure 5.1c). By moving the carriage along the horizontal direction and the frame along the vertical it was possible to obtain measurements at any positions along the profile.

5.1.1 Experimental procedure

The flow velocity was measured at 22 cross-shore locations in the range x=49-64 m. For each cross-shore position, the frame was positioned at three different elevations, yielding velocity measurements by the LDAs and ADVs at 12 elevations, in addition to the ADVP measurements which covered a 0.15 m profile above the bed with 1.5 mm vertical bin size resolution. Additional detailed measurements of the wave boundary layer flow were obtained at x=50.78 m. These velocities were measured with the LDA at 16 vertical positions, starting from 0.005 m up to 0.125 m from the top of the bed roughness and logarithmically spaced to capture the velocity distribution within the boundary layer. At each cross-shore position of the frame, waves were generated for approximately 45 minutes. Measurements were obtained for a duration of 12 min at each elevation, corresponding to approximately 120 waves.

The water surface elevation was measured at 12 cross-shore locations by means of resistive wave gauges (WG) and at 52 locations by means of acoustic wave gauges (AWG). In addition, 15 pressure transducers (PPT) were used to determine

the water surface elevation with linear wave theory; one of them was fastened to the carriage in order to measure the water surface oscillation in proximity of ADVs and LDAs. All these instruments measured the water surface elevation at a frequency of 40 Hz.

5.1.2 Organization of data files and data processing

Data were collected in a binary file, except LDA velocity measurements that were collected in specialised text files. Hereinafter, the procedure followed to process regular waves data, measured by above-mentioned probes, was described.

Processing ADVs Two Vectrino (Nortek As.) ADVs were employed during the experiment: ADV_4 ($ADV336$ according to $test.serialADV$ variable in the binary file) coming from Twente University (TU) and side looking ADV_5 ($ADV376$) property of the Universitat Politècnica de Catalunya (UPC), see Figure 5.1c. ADV_5 was closer to the bed throughout the experiments, indeed, it measured velocities at the elevations $z = 0.11, 0.28, 0.48$ m with respect to the bed, whereas ADV_4 measured at $z = 0.42, 0.60, 0.80$ m.

The signal was acquired continuously throughout each run, both when the carriage was stable and when it was moving. Such a signal had to be divided into intervals in order to analyse only data measured when the probe was at a stable position; other data were discarded. The boundaries of these intervals were evaluated by the variables $sync.lda1$ and $time\_sync$ of the run binary file. The first one is close to 5 V when the LDA is measuring (i.e. when it is fixed) whereas is close to zero when it is moving. The second one collected time series; indeed, the LDA sample rate is not constant but it varies according to the measured velocities.

These three significant signal sections were analysed separately.

Measurements carried out with ADVs are often affected by spurious data which appears in the form of spikes. When few, isolated spikes are present, the time series can be corrected using a despiking routine based on phase-space and replaced through interpolation using cubic polynomial (Goring and Nikora, 2002). On the other hand, when the spikes appear continuously during certain range of time the entire measurement must be rejected. The last condition occurred in some cases in the present experiments, due to significant air bubble presence and probe emergence. These spurious measurements as well as intervals of ADV probe emergence from the water could be well identified on the basis of a signal to noise ratio below 7 or a correlation value below 50%. Spurious data records due to isolated

spikes were removed using a despiking routine based on phase-space and replaced through interpolation using cubic polynomial. Spurious velocity measurements above wave trough level were detected on the basis of signal to noise ratio and correlation and set to NaN. Thus, mean velocities above to the trough level were computed over the full wave period.

It should be observed that, just after the despiking routine, a high pass filter was applied to remove the low frequency wave generated within the flume. The low frequency wave period, $T_{lf} \simeq 18.2$ s, was identified using Welch's estimator, (see Welch, 1967). The cut-off threshold was $f_c = 0.5/T$. Such a filter affected the velocities of the first two waves that, for this reason, were cut out.

A zero up-crossing method was adopted to split the cleaned signal and to calculate the ensemble averaged velocities. Zeros were identified from the elevation measured by the resistive wave gauge closest to the paddle in order to show the wave propagation within the flume. Such a procedure was implemented hereinafter for each velocity or elevation signal. The latter also allowed to break free from the turbulence measured by velocimeters minimizing the offset in timing between the waves in the ensemble. Finally, a matrix containing in each column a velocity fluctuation throughout a period and in each row a phase was arranged. Since the ADVs sample frequency was 100 Hz, the matrix had about 600 rows. The phase mean was replaced by a NaN every time that the ADV recorded less than 25 waves.

Processing LDAs Two LDAs were employed during the experiment: LDA_1 coming from the University of Aberdeen (UA) and LDA_2 coming from the University of Catania (UC). Unfortunately, some troubles conditioned one of the processors, therefore LDA_2 recorded data only during runs 70-76, 78 whereas LDA_1 worked throughout the experiment.

The LDA signal analysis is considerably similar to the ADV ones. However, LDA signal is not affected by spikes and its reliability is not related to the SNR or Correlation. Therefore, it had not to be cleaned. Since LDA sample frequency is not a constant data were split in several bins wide 40^{-1} s, to agree with wave gauges sample frequency. The median m and the standard deviation std of each bin were calculated. Data outside the threshold of $m \pm 3std$ were marked as outliers and discarded. Remaining data were averaged.

Processing wave gauges The x position of all WGs and PPTs from 2 to 14 were not modified throughout experiments whereas starting from run 94 several AWGs

$(1-5, 8, 13, 14, 16-18)$ were redeployed, see Table 5.1. PPT_1 was redeployed starting from run 89, whereas PPT_{15} was fastened to the carriage throughout the campaign: only data recorded at the first elevation (the closest to the bed) were analysed. Sea surface time-series recorded by PPTs had to be detrended by the mean water level (average of data recorded during the first 10 seconds) and corrected for depth attenuation of pressure by the linear wave theory.

Data recorded during the transient regime (0-300 s) were cut from the water surface elevation. Then, low frequency waves were subtracted and the signal was split and averaged by the zero up-crossing method above mentioned. Data outside the threshold of $m \pm 3std$ were omitted from the average of each phase.

5.2 Experiments

HYBRID experiment involved both regular ($T = 6$s, $H = 0.55$m) and bichromatic waves ($T_m = 4.2$s, $T_{gr} = 31.5$ s, $H_{max} = 0.69$ m).

All the results presented in this thesis concern a monochromatic wave regime with period T=6 s and wave height H=0.55 m propagated throughout runs 19-26 (wave boundary layer measurements) and 70-76, 78, 79, 83, 89-99, 101, as reported in Table 5.1. In particular, Table 5.1 shows the measurement position within the flume in terms of the x coordinate of the frame and the z coordinate of $LDA1$ and $ADV5$, wave height and period measured by $PPT15$. Finally, the water depth in the deeper part of the wave flume, that was equal to 2.65 m throughout the experiment and the test duration.

The experiments were conducted at large scale to generate a boundary layer flow with a Reynolds number that is similar to field conditions. As a result, scale effects on the bottom boundary layer flow, which are inherent to small-scale laboratory experiments, are minimized in the present study.

The velocity components along the x, y and z directions are denoted as U, V and W respectively.

Within the wave flume statistically steady conditions were generally established approximately 300 s after the wave paddle started. This time was evaluated by analyzing the temporal developments of the water surface elevations and the velocity at different cross-shore and vertical positions. After discarding the first 300 s the remaining time series were used to compute the velocity and water surface statistics. In all the cases the statistics were computed on the basis of no less than 100 waves. The ensemble average was determined as follows:

Table 5.1: Characteristics of the performed experiments involving monochromatic waves at the UPC large scale wave flume.

Run name	x [m]	z_{LDA} [mm]	z_{VP} [mm]	H [m]	T [min]	d [m]	duration [s]
19	50.77	0	7.1	0.55	6.00	2.65	45
20	50.77	1	7.2	0.55	6.00	2.65	45
21	50.77	3	7.4	0.55	6.00	2.65	45
22	50.77	7	7.8	0.55	6.00	2.65	45
23	50.77	19	9.0	0.55	6.00	2.65	45
24	50.77	37	10.8	0.55	6.00	2.65	45
25	50.77	67	13.8	0.55	6.00	2.65	45
26	50.77	125		0.55	6.00	2.65	39
70	64.00	25.0	8.0	0.55	6.00	2.65	20
	64.00	200.1	25.5	0.55	6.00	2.65	12
	64.00	400.0	45.5	0.55	6.00	2.65	12
71	63.00	25.0	8.0	0.55	6.00	2.65	20
	63.00	200.0	25.5	0.55	6.00	2.65	12
	63.00	399.9	45.5	0.55	6.00	2.65	12
72	62.00	25.0	8.0	0.55	6.00	2.65	20
	62.00	200.0	25.5	0.55	6.00	2.65	12
	62.00	400.0	45.5	0.55	6.00	2.65	12
73	61.00	25.1	8.0	0.55	6.00	2.65	20
	61.00	200.0	25.5	0.55	6.00	2.65	12
	61.00	400.0	45.5	0.55	6.00	2.65	12
74	60.00	25.0	8.0	0.55	6.00	2.65	20
	60.00	200.0	25.5	0.55	6.00	2.65	12
	60.00	400.0	45.5	0.55	6.00	2.65	12
75	59.00	25.0	8.0	0.55	6.00	2.65	20
	59.00	200.0	25.5	0.55	6.00	2.65	12
	59.00	400.0	45.5	0.55	6.00	2.65	12
76	58.50	25.0	8.0	0.55	6.00	2.65	20
	58.50	200.0	25.5	0.55	6.00	2.65	12
	58.50	399.9	45.5	0.55	6.00	2.65	12

Run name	x [m]	z_{LDA} [mm]	z_{VP} [mm]	H [m]	T [min]	d [m]	duration [s]
78	58.00	25.0	8.0	0.55	6.00	2.65	20
	58.00	200.1	25.5	0.55	6.00	2.65	12
	58.00	400.1	45.5	0.55	6.00	2.65	12
79	57.50	25.1	8.0	0.55	6.00	2.65	20
	57.50	200.0	25.5	0.55	6.00	2.65	12
	57.50	400.0	45.5	0.55	6.00	2.65	12
83	52.00	25.1	8.0	0.55	6.00	2.65	20
	52.00	200.0	25.5	0.55	6.00	2.65	12
	52.00	400.0	45.5	0.55	6.00	2.65	12
89	57.00	25.2	8.0	0.55	6.00	2.65	48
	57.00	200.1	25.5	0.55	6.00	2.65	48
	57.00	400.0	45.5	0.55	6.00	2.65	48
90	56.50	25.0	8.0	0.55	6.00	2.65	48
	56.50	200.0	25.5	0.55	6.00	2.65	48
	56.50	399.9	45.5	0.55	6.00	2.65	48
91	56.00	25.1	8.0	0.55	6.00	2.65	48
	6.70	200.0	25.5	0.55	6.00	2.65	48
	6.70	400.0	45.5	0.55	6.00	2.65	48
92	55.50	24.9	8.0	0.55	6.00	2.65	48
	6.70	74.9	13.0	0.55	6.00	2.65	48
	6.70	200.0	25.5	0.55	6.00	2.65	48
93	55.00	25.0	8.0	0.55	6.00	2.65	48
	6.70	75.0	13.0	0.55	6.00	2.65	48
	6.70	195.0	25.0	0.55	6.00	2.65	48
94	54.50	24.8	8.0	0.55	6.00	2.65	48
	6.70	75.0	13.0	0.55	6.00	2.65	48
	6.70	200.0	25.5	0.55	6.00	2.65	48
95	54.00	25.0	8.0	0.55	6.00	2.65	48
	6.70	75.0	13.0	0.55	6.00	2.65	48
	6.70	200.0	25.5	0.55	6.00	2.65	48
96	53.50	25.0	8.0	0.55	6.00	2.65	48
	6.70	75.0	13.0	0.55	6.00	2.65	48
	6.70	200.0	25.5	0.55	6.00	2.65	48
	6.70	75.0	13.0	0.55	6.00	2.65	48

Run name	x [m]	z_{LDA} [mm]	z_{VP} [mm]	H [m]	T [min]	d [m]	duration [s]
97	53.00	25.0	8.0	0.55	6.00	2.65	48
	53.00	199.9	25.5	0.55	6.00	2.65	48
	53.00	400.0	45.5	0.55	6.00	2.65	48
98	50.77	25.0	8.0	0.55	6.00	2.65	48
	50.77	200.0	25.5	0.55	6.00	2.65	48
	50.77	400.0	45.5	0.55	6.00	2.65	48
99	49.00	25.0	8.0	0.55	6.00	2.65	48
	49.00	200.0	25.5	0.55	6.00	2.65	48
	49.00	400.0	45.5	0.55	6.00	2.65	48
101	59.50	25.0	8.0	0.55	6.00	2.65	48
	59.50	200.0	25.5	0.55	6.00	2.65	48
	59.50	400.0	45.5	0.55	6.00	2.65	48

$$\langle U \rangle = \frac{1}{N} \sum_{n=0}^{N-1} U(t+nT) \tag{5.1}$$

where T is the wave period, and N the number of waves included in the computation of the ensemble average. The wave period was evaluated from the water surface elevations measured with the resistive wave gauge located at x=50.85 m. The wave period T was computed as the arithmetic average of the periods of about 100 waves obtained by applying the zero up-crossing technique to the water surface elevation time series. In all the runs the standard deviation of T was approximately $6 \cdot 10^{-3}$ s, thus confirming that the periods exhibits only a very small wave-to-wave variation, which allows using a constant value for T in the averaging procedure. Expressions analogous to Equation 5.1 were used to compute the ensemble average of the other velocity components and for the free surface elevation.

The non-equidistant sampled LDA measurements were phase-averaged, accounting for particle residence time to prevent velocity bias. The instantaneous velocity U can be written as follows:

$$U = \overline{u} + \tilde{u} + u' \tag{5.2}$$

where the bar denotes a time average, the tilde denotes the periodic fluctuating

term of the ensemble average $\langle U \rangle$ and the prime denotes the turbulent component ($\langle U \rangle = \overline{u} + \tilde{u}$).

5.3 Analysis of results

Moving from the shoaling zone to the surf zone, over a non-cohesive bed, a breaker bar parallel to the shoreline appears. There, waves break reducing the level of wave energy reaching the shore, in this way acting as a natural breakwater. The hydrodynamics generated by a breaking plunging wave are here described on the basis of results of a series of large scale flume experiments. These results were early described by Scandura et al. (2018).

5.3.1 Water surface elevation

Figure 5.2 shows the bed profile, wave height, the mean water surface elevation (set-up/set-down) and the root-mean-square (rms) of the water surface elevations along the wave flume. The wave overturning which leads to breaking begins at x=53.50 m approximately (see 'breaking point' in Figure 5.2a). At x=55.50 m the wave overturning is completed (see 'plunging point' in Figure 5.2a) and the plunging jet hits the free surface causing a localized transfer of momentum to the water column. As a consequence a new wave is generated which very rapidly becomes a stable roller that propagates towards the beach.

The wave height measured by AWGs is close to 0.55 m in the horizontal part of the wave flume but Figure 5.2b shows that it oscillates along x. A rough estimate of amplitude and wavelength of these oscillations shows that they are approximately 0.12 m and 15 m respectively. These oscillations are likely due to wave reflection from the beach, which generates partial standing waves whose envelop of wave heights has a wavelength equal to half the wavelength of the incident progressive wave. This explanation is consistent with the estimated wavelength of the progressive waves, which is equal to 30 m approximately. However, the reflection does not have a significant effect on the processes that occur in the surf zone which are characterized by intense energy dissipation.

The mean water level (Figure 5.2c) is approximately equal to zero up to x=40 m. Then a set-down begins which lasts up to x=55.50 m approximately. Although within the range x=40-55.50 m the data are rather scattered, it can be appreciated that the set-down is about -0.01 m on average. The mean water level $\overline{\eta}$ starts to increase near x=55.5 m, which is the location where the plunging jet hits the water

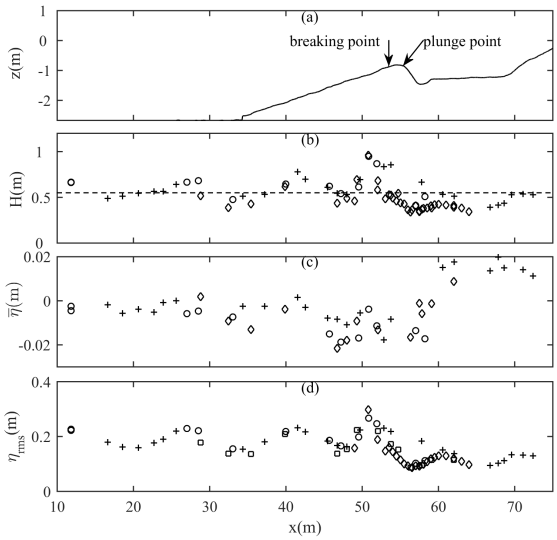

Figure 5.2: Wave characteristics along the wave flume measured by resistive and acoustic wave gauges and pressure transducers: (a) Bed profile of the wave-flume, (b) wave height, (c) mean water level, (d) rms of the free surface elevation. Symbols: ∘ Resistive wave gauges, + acoustic wave gauges, ◇ pressure transducers.

surface. This increase in mean water level is a result of the decrease of the onshore momentum flux due to the wave energy dissipation, which must be balanced by a positive cross-shore gradient in $\overline{\eta}$. The rms of the free surface elevation (Figure 5.2d) is about 0.2 m in the horizontal part and exhibits oscillations analogous to those observed for the wave height.

5.3.2 Time-averaged outer flow

The velocities used for the spatial representation of the time-averaged cross-shore velocity $\overline{u}$ and vertical velocity $\overline{w}$ within the measurement region are those measured by LDA_1, LDA_2 and ADV_2 which showed reasonable agreement among themselves. The data from ADV_1 were discarded because, from the most offshore measurement location up to the bar trough, they showed a slight yet constant disagreement with those provided by the other instruments. This discrepancy can be attributed to the fact that the x position of ADV_1 was about 0.17 m offshore with respect to that of the other instruments.

In the two-dimensional plots presented in the figures below, nine measurements points distributed over the depth were used at each of the 22 cross-shore positions. These points were obtained by measuring the velocity at three different positions by means of LDA_1, LDA_2 and ADV_2, with three different elevations of the frame at each cross-shore location. From the 198 measurement points, 10 data records were discarded because of instrument malfunctioning or poor data quality. To enable a constant number of points to be plotted along each vertical, these missing recordings were replaced by ADVP data or by means of interpolation from adjacent data. Replacing data by interpolation did not alter the main trend of the velocity distribution, since it was used only where the velocity was not subject to rapid changes, moreover the missing data records were few in comparison to the total number of recordings.

Figures 5.3, 5.4 show the spatial distribution of the mean velocity in the x- and z-direction, respectively. At the most offshore shoaling zone locations, the mean velocity is small and almost constant with depth. At x=49 m for example, the velocity shows only small variations along z and takes values of -0.05 ms^{-1} approximately. This velocity is seaward directed in order to balance the landward mass transport near the water surface induced by the progressive wave. This onshore flux contribution is present in Figure 5.3 only at a few locations as measurements were mainly obtained in the lower part of the water column. The negative velocities increase further shorewards reaching values of -0.20 ms^{-1} around the bar crest at x=53.5 m, where the overturning process begins. The mean vertical velocity (shown in Figure 5.4) is rather small at these locations. From this point up to x=57.5 m the mean horizontal velocity slightly decreases in magnitude. At x=55.5 m the plunging jet hits the free surface and subsequently penetrates obliquely into the mass of water, transferring a large amount of momentum. Figure 5.4 shows that this momentum transfer gives rise to large negative mean velocities which reach the bed at x=58-60 m. The largest mean velocities in Figure 5.3 occur where

the mean vertical velocity vanishes (Figure 5.4). This shows that in this region the offshore current grows in magnitude as long as there is a downward flux that feeds it. The upward flux close to the shoreward face of the bar balances this downward flux plus the undertow coming from the inner surf zone. Thus, it contributes to the establishment of a large scale circulation which allows landward mass transport to take place without violating mass conservation. Part of the fluid however remains trapped in a recirculation cell just above the bar trough. The maximum of both the mean cross-shore and vertical velocities are attained within this cell and are approximately 0.40 and 0.15 ms^{-1} respectively. In the inner surf zone (x >60 m) the offshore velocity is mostly constant and approximately 0.2 ms^{-1} even close to the bed, indicating that here the undertow has a strong impact on the boundary layer. In contrast, in the inner surf zone the mean vertical velocity is small (Figure 5.4), with magnitudes comparable to those in the shoaling region.

Figure 5.3 shows that over the onshore face of the bar (x=55.5 to 57.0 m) a small near-bed area is present where the mean velocity is positive while the velocity is negative at adjacent locations. The dynamic mechanism responsible for this positive mean velocity is not clear yet. From a kinematical point of view this positive velocity is due to the negative vertical velocity occurring offshore which extends up to the onshore face of the bar where, due to the inclination of the bottom, a positive u velocity component is generated. Continuity is satisfied since the upward current that occurs at x=57 m which brings the water towards the surface.

In Figure 5.5 the time-averaged rms of the cross-shore velocity fluctuations $\overline{u'_{rms}} = \overline{\langle u'^2 \rangle^{1/2}}$ is shown. In the shoaling region (x=49 m) $\overline{u'_{rms}} \approx 0.02$ ms^{-1} and it is rather constant over depth, except close to the bed where the contribution from bed generated turbulence is important. On the bar, turbulence intensity increases up to 0.055 ms^{-1} on average. Here $\overline{u'_{rms}}$ attains the minimum in the middle of the water column at z=-0.6 m approximately. This is due to the coexistence of two main sources of turbulence: the boundary layer and the free surface. The highest measured values of $\overline{u'_{rms}} \approx 0.25$ ms^{-1} and occurs at the highest measurement point at x=58.50 m, because of the direct impact of the plunging jet. The rms of u' is also large near the bed at x=57.5 m where it takes values of ≈ 0.15 ms^{-1}, but here turbulent fluctuations are mainly generated by boundary layer processes rather than the direct effect of wave breaking.

The time-averaged rms of the vertical velocity fluctuations $\overline{w'_{rms}} = \overline{\langle w'^2 \rangle^{1/2}}$, shown in Figure 5.6, is generally only slightly smaller than $\overline{u'_{rms}}$. For example, in the inner surf zone the maximum measured values of $\overline{u'_{rms}}$ and $\overline{w'_{rms}}$ are 0.15

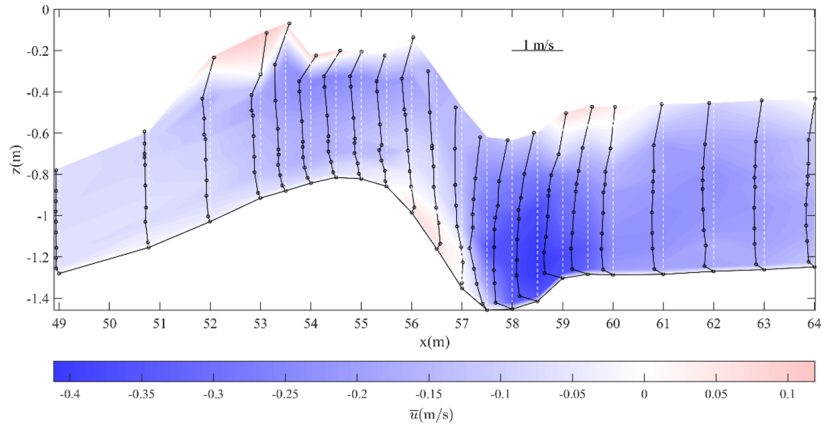

Figure 5.3: Time-averaged cross-shore velocity $\overline{u}$.

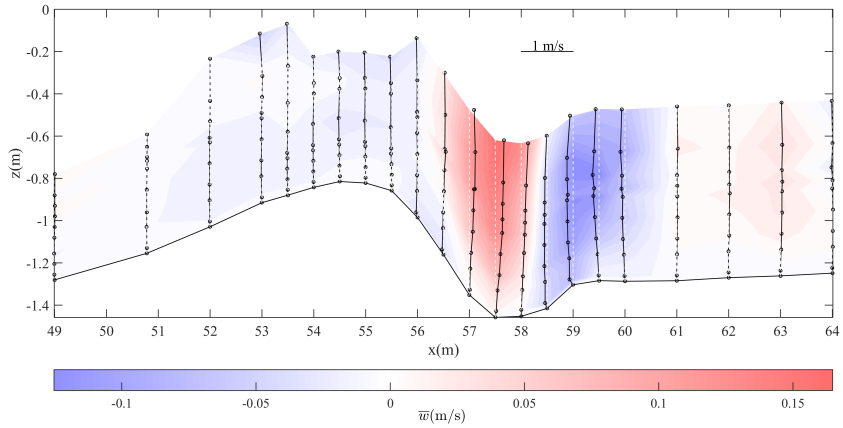

Figure 5.4: Time-averaged vertical velocity $\overline{w}$.

and 0.12 ms^{-1} approximately. This result implies a certain degree of turbulence isotropy which certainly does not occur in the boundary layer. Similar to $\overline{u'_{rms}}$, $\overline{w'_{rms}}$ is very large above the trough of the bar with values of 0.22 ms^{-1}.

Another similar characteristic is the trend of the vertical profile on the bar crest which show a minimum close to z=-0.6 m. The main difference between $\overline{u'_{rms}}$ and $\overline{w'_{rms}}$ occurs near the bed. Indeed, the high values of $\overline{u'_{rms}}$ detected near the bed at x=57-58 m in Figure 5.5 are not observed for $\overline{w'_{rms}}$ in Figure 5.6 because of the near bed turbulence anisotropy.

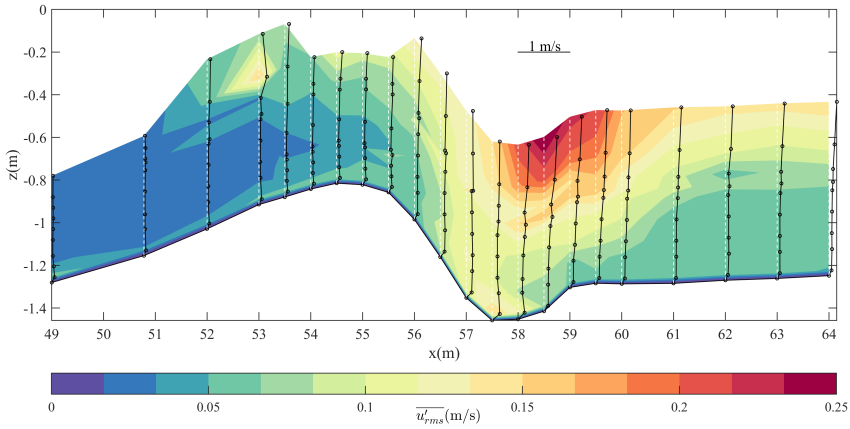

Figure 5.5: Time-averaged root mean square cross-shore turbulent velocity.

5.3.3 Boundary layer flow

The boundary layer flow was measured by means of LDA and ADVP, however only at x=50.78 m detailed measurements within the boundary layer carried out by means of LDA are available. This section is devoted to the analysis of the boundary layer measurements by LDA at x=50.78 m.

Location x=50.78 m is in the shoaling region, 4 m offshore away from the bar crest, thus at this location only an indirect effect of the breaking processes that occur further onshore may be detected. Figure 5.7a shows the time development of the free stream velocity measured at z'=0.125 m (z' is the distance from the top of the bed roughness). It can be observed that the free stream velocity has a large

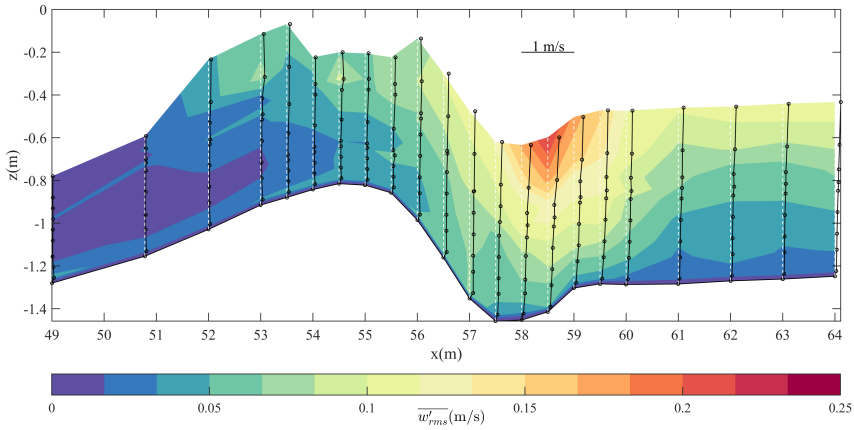

Figure 5.6: Time-averaged root mean square vertical turbulent velocity.

wave induced velocity skewness and acceleration asymmetry Scandura et al. (see 2016). The skewness *Sk* and the asymmetry *Asy* measure the departure of the free stream velocity from a sinusoidal function and are given as follows:

$$Sk = \frac{\overline{\tilde{u}^3}}{\overline{\tilde{u}^2}^{3/2}}, \quad Asy = \frac{\overline{\dot{\tilde{u}}^3}}{\overline{\dot{\tilde{u}}^2}^{3/2}} \tag{5.3}$$

where a dot denotes a time derivative. Wave induced skewness and asymmetry of the free stream velocity shown in Figure 5.6a are equal to 0.93 and 1.45 respectively, due to the strong prevalence of positive velocities and accelerations compared to the negative ones. The Reynolds number R_δ of the boundary layer based on the maximum of the free stream velocity and on the thickness of the Stokes layer $\delta = \sqrt{\nu T/\pi}$ (ν is the kinematic viscosity) is equal to 1000 approximately. It decreases to 800 approximately if the Reynolds number is evaluated by means of the arithmetic average of the positive and negative velocity peaks. Considering that the roughness is made up by gravel with $d_{50} = 9 \cdot 10^{-3}$ m, in all the cases the flow falls in the rough turbulent regime according to the classification of Jonsson (1980).

Figure 5.7 shows the free-stream velocity (plot a) and the vertical distributions of the time-averaged horizontal velocity at 7 stages of the wave cycle (plot b).

The variability in the vertical profiles appears to be due to offsets in synchronization between the different acquisitions. Figure 5.7 shows that at t=0 the velocity rapidly increases and attains the maximum at t=0.5 s. At this phase there is a well-defined overshoot in the velocity profile at z'= 0.02 m, probably enhanced by the convergence effect of the bed geometry. The Reynolds stress (Figure 5.8), which was positive everywhere at t=0 s, becomes negative near the bed at t=0.5 s and remains positive far from the bed. The positive Reynolds stress is due to the negative velocity gradient that occurs above the point of the velocity maximum while the negative part is due to the positive velocity gradient near the bed ($z' < 0.02$ m). After t = 0.5 s the velocity decreases but at t=1 s the Reynolds stress is larger than at t=0.5 s. At t=1.9 s the velocity is small and the Reynolds stress is reduced substantially near the bed. An increase of the velocity in the negative direction (t=2.5 s) causes an increase of the Reynolds stress which finally becomes positive at t=4.5 s when the maximum negative velocity is attained. Because of skewness and asymmetry, and because of the undertow, the mean velocity and the Reynolds stress do not vanish in the boundary layer. The mean velocity is negative at z'=0.12 m where it reaches its outer flow value of -0.05 ms^{-1} approximately. The mean Reynolds stress has a more intricate trend: below z'=0.007 m it is positive, then it becomes negative up to 0.025 m, at higher elevations it becomes positive again and finally tends asymptotically to zero far from the bed.

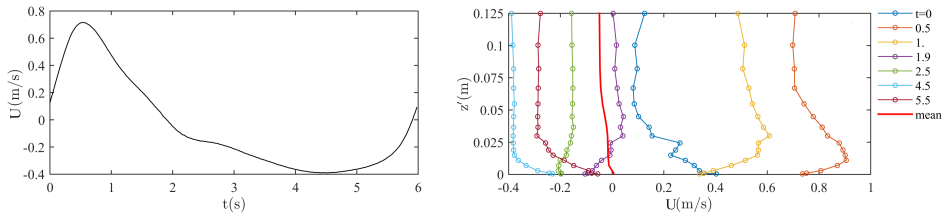

(a) (b)

Figure 5.7: (a) Free stream velocity; (b) velocity profiles. x=50.78 m.

Figure 5.9 shows the rms of the cross-shore and vertical turbulent velocity fluctuations in the boundary layer. First of all it can be observed that in the boundary layer the cross-shore turbulent intensity is larger than the vertical turbulent intensity at all the phases. The turbulent intensities increase during the accelerating

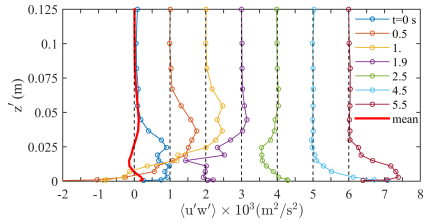

Figure 5.8: Reynolds stress at x=50.78 m. For clarity, the data of each phase are shifted forward by $10^{-3}m^2/s^2$ with respect to those of the previous phase.

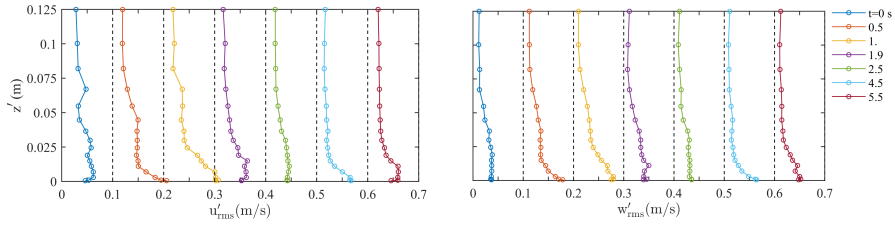

(a) (b)

Figure 5.9: Turbulent intensities at x=50.78 m. (a) Cross-shore turbulent intensity; (b) Vertical turbulent intensity. The data of each phase are shifted forward by 0.1 ms^{-1} compared to those of the previous phase.

phase and become large at the peak of the free stream velocity (t=0.5 s). However, as already observed for the Reynolds stress, the turbulent intensities continue to increase during the decelerating phase and at t=1 s they attain values larger than those at the peak of the free stream velocity. Turbulent intensities during the on-shore flow half-cycle are higher than those of the offshore flow half-cycle because of the flow skewness and asymmetry. The increase in turbulent intensity during the decelerating phase is analysed in Figure 5.10 which shows the temporal development of u'_{rms} at three different elevations, with the free stream velocity given as reference.

It can be seen that very close to the bed the first peak of u'_{rms} (red line) has a small delay with respect to the peak of U_0. It can be observed that because of this

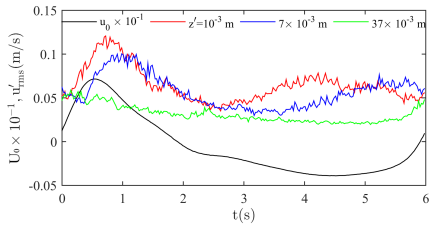

Figure 5.10: Time variation of u'_{rms} at three different elevations. The free stream velocity U_0 is shown as reference. x=50.78 m.

delay u'_{rms} at t=0.5 s is slightly smaller than at t=1 s. The difference between the two phases increases at higher elevation. Indeed at $z' = 7 \cdot 10^{-3}$ m (blue line) the delay of the first peak increases and u'_{rms} at t=0.5 s further decreases significantly. Such a forward shift of the phase of u'_{rms} with z' is mainly due to turbulent diffusion and it was observed also in numerical simulations (Scandura et al., 2016). At higher distance from the bed ($z' = 37 \cdot 10^{-3}$ m) only one main peak is detected.

5.4 Discussion

The flow velocity was measured with high spatial and temporal resolution under monochromatic waves plunging on a fixed barred beach in a large-scale wave flume. In the shoaling region the undertow velocity is small, while its magnitude increases on the bar crest where a velocity of -0.2 ms^{-1} is detected approximately 0.32 m below the still water level. On the bar crest the mean vertical velocity is small and does not exceed values of 10^{-2} ms^{-1}. Shoreward from the bar crest the mean horizontal offshore directed velocity slightly decreases in magnitude up to the trough of the bar where it suddenly increases in the lower part of the water column. At the same location, the mean vertical velocity component increases to allow the strong offshore fluid flux to be directed upward. This fluid flowing offshore comes mainly from the inner surf zone and when it is pushed up, near the shoreward face of the bar, it feeds the onshore mass transport that in turn feeds the undertow current. Part of the fluid however remains trapped in a recirculation cell located above the trough of the bar. Within this flow recirculation zone the mean velocities attain the largest values. In magnitude the maximum mean velocities are 0.4 ms^{-1} for the horizontal component and 0.15 ms^{-1} for the vertical. Where the

plunged wave propagates in the form of a bore, the mean velocity is mostly constant along the cross-shore x direction and takes values of approximately 0.2 ms^{-1} until near to the bed, thus the boundary layer is strongly affected by the undertow.

The time-averaged cross-shore and vertical turbulent intensities are considerable within the recirculation cell above the bar trough, where they take maximum values of 0.25 and 0.22 ms^{-1} respectively. Generally, the two turbulent intensities differ only slightly; in the inner surf zone, for example, maximum measured values of $\overline{u'_{rms}}$ and $\overline{w'_{rms}}$ are approximately 0.15 and 0.12 ms^{-1} respectively.

Specific results concerning the boundary layer were reported for a location corresponding to the shoaling region where detailed LDA measurements are available. The free stream velocity has a large velocity skewness and acceleration asymmetry. These characteristics combined with the flow convergence effect due to the bed slope result in a much more prominent overshoot in the onshore half-cycle velocity profiles compared to that in the offshore half-cycle. The Reynolds stress shows trends that are expected based on the velocity profiles: it is negative when the velocity gradient is positive and vice-versa, and it is very small outside the wave boundary layer. Near the bed, the Reynolds stress and the rms of the velocity fluctuations increase during the first part of the decelerating phase. The turbulence intensities show two peaks during the wave cycle, characterized by a depth-dependent time lag with respect to the free-stream velocity due to turbulent diffusion.

6 Shallow water basin experiments

The DHI Water and Environment Shallow Water Basin allows the propagation of combined waves and currents at angles ranging from 30° to 90°. It is 35 m long and 25 m wide with an overall depth of 0.8 m. The basin is ideal for model testing when the effects of combined waves and current are of major importance, as it happens in coastal regions. The wavemaker front is 18 m wide, and it is obtained by means of an array of 36 piston-type wave paddles, 1.2 m high and 0.5 m wide each. Each paddle is controlled by an electric-servo motor through software *WSProject*, allowing the wave type (regular or random), the water depth, the wave characteristics and the test duration to be set up. In Figure 6.1 a sketch of the shallow water tank is reported. The origin of the reference system is located in the upper left corner of the basin and it is identified in Figure 6.1 with O; the x-axis follows the current direction, while the y-axis is directed as the wave propagation direction. z-axis has the origin at the bottom and points upward.

The 3D wave generator is designed to operate at water depths d between 0.2 m and 0.8 m. The wave generator is equipped with Active Wave Absorption Control System (*AWACS*) in order to deal with undesired reflection of waves to the wave generator, and to allow full control of the incident waves. The latter however was not used in the present campaign. A C-shaped gravel beach with a slope of 1/5.6, coupled with passive parabolic wave absorbers, provides energy absorption at the opposite end of the wave basin.

The shallow water basin is also equipped by a three-pump system able to supply a discharge of 1 m^3/s. In order to get the desired current velocity, the inlet width was reduced from 25 to 12 m, and at the end of the inlet a series of panels were placed along the current direction to direct and straighten the flow up to the gravel beach.

Within the experimental campaign, two different water depths were considered, 0.4 and 0.6 m. In this way two different current conditions were generated

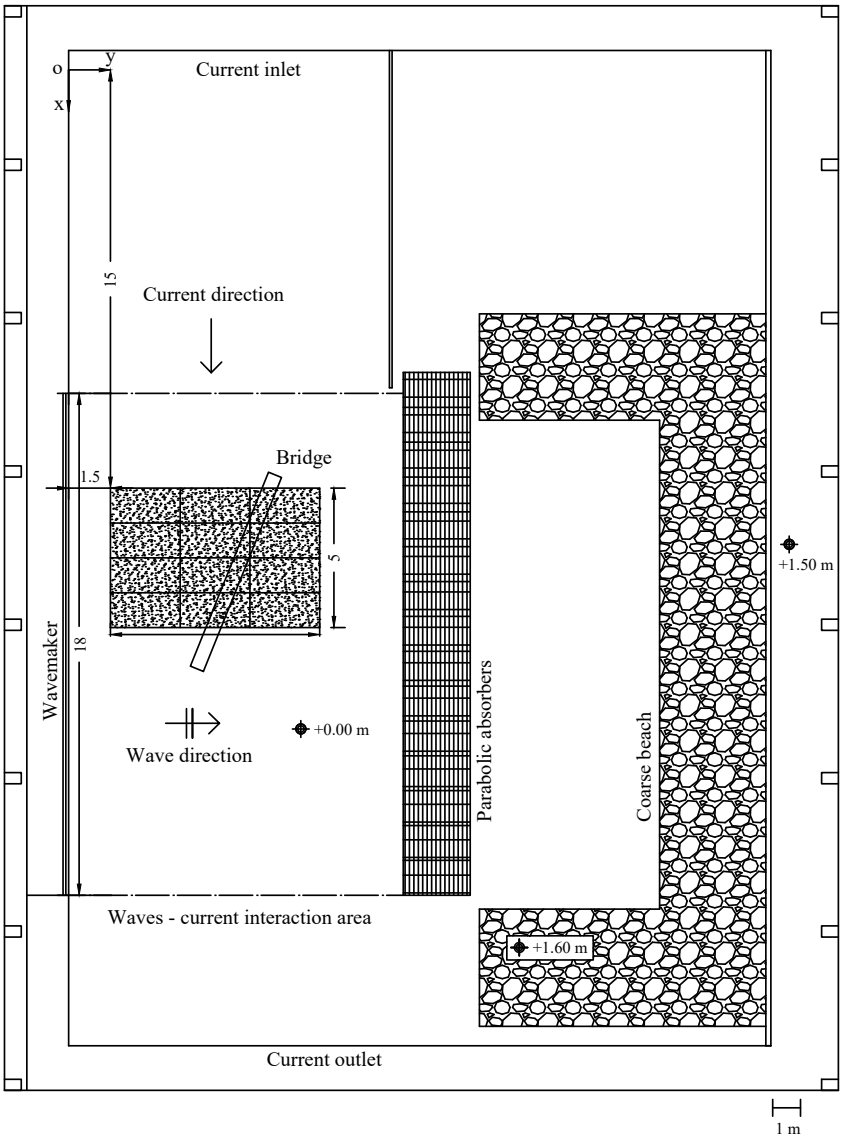

Figure 6.1: Sketch of the DHI shallow water basin.

within the flume. Indeed, the combination of the wave and the current conditions led to reproduce both wave and current dominated regimes.

Two different rough beds, namely a sand bed (SB) and a gravel bed (GB) were installed in the wave current interaction area of the basin, covering a surface of 5 x 7.5 m. They have been obtained by gluing sand (d_{50}=0.9-1.6 mm) or gravel (d_{50}=16-32 mm) on wood tiles, whose dimensions are 1.25 x 2.5 m each. The tiles were thus drilled on the concrete floor in order to be fixed. In the GB case a three dimensional surface reconstruction of the rough bottom was also performed by means of several pictures of the bed.

6.1 Measurements

The free surface elevation was recorded by means of 24 resistive level gauges located throughout the rough bed area. Five wave gauges were located at a proper distance along the same y-coordinate in order to measure wave reflection inside the tank. The exact position of each probe is indicated in Table 6.1 and reported in Figure 6.2. In particular, a sketch of the wave gauges aligned with vectrinos, i.e. W9-W15, is reported in Figure 6.3.

Five vectrinos Single Point, one of which Vectrino side looking and the remaining four down looking, along with two Vectrino profilers were used in order to acquire velocity profiles over the rough bed in the uniform wave-current interaction area. In the sand and gravel tests the Single Point vectrinos are placed in square, (see Figure 6.4a, 6.4b, respectively). Their position inside the rough surface area is marked by a square and indicated by V. One Profiler is displaced 1 m upstream with respect to the center of the square, marked by a circle and indicated by $P1$. Initially a second Profiler $P2$ was placed 1 m downstream in the current direction. However during the first tests performed with the sand bed it was noticed that the latter Profiler was not giving any signal, and after many trials the relative profiles were not acquired. During the gravel campaign the Profiler was removed.

The location of the vectrinos is reported in Figure 6.5 for the sand and gravel bed case; their coordinates are also indicated in Table 6.2. Moreover, a seeding system was fixed to the vectrinos support in order to increase the data quality, see paragraph 6.1.3 (Figure 6.4d).

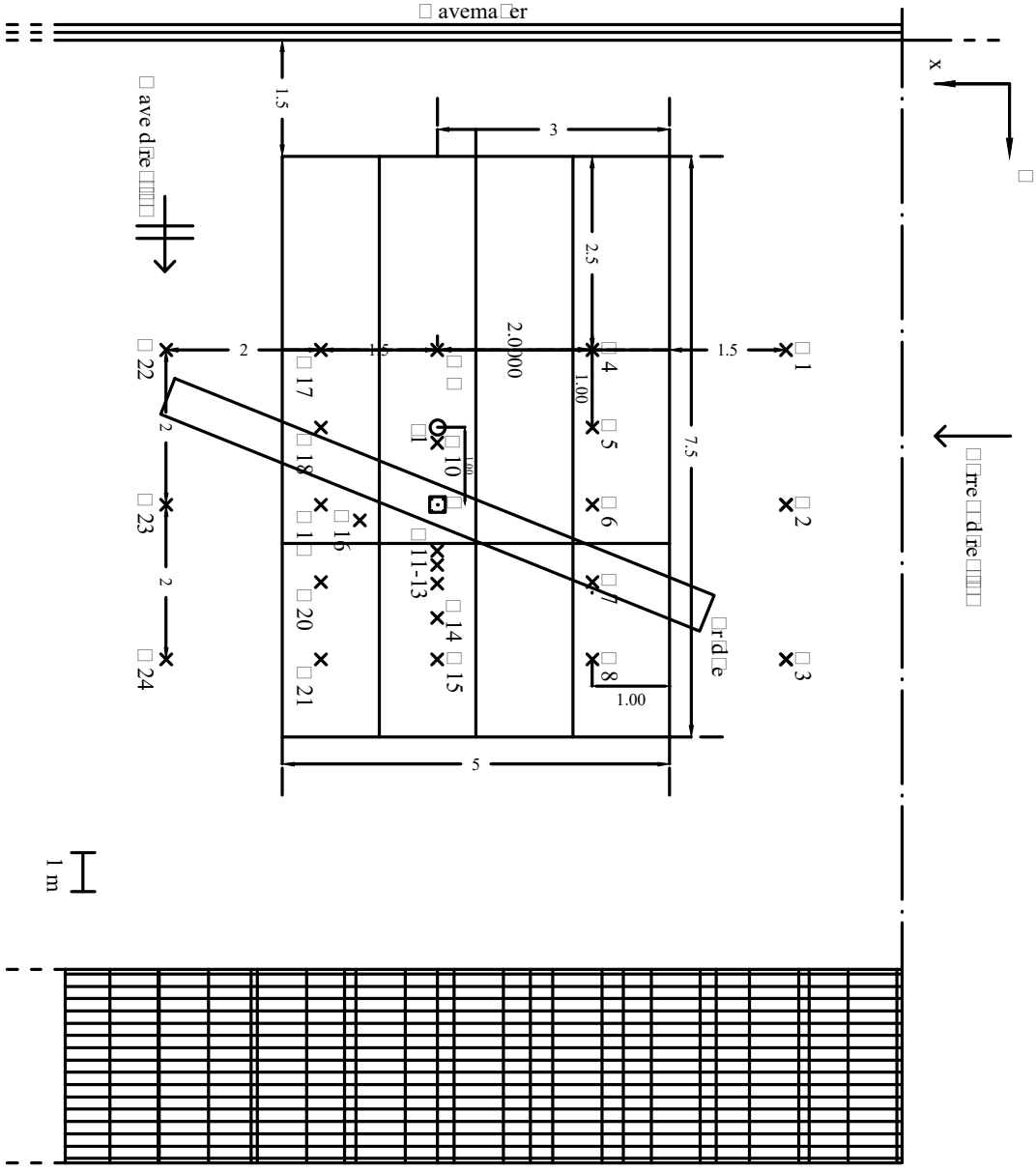

Figure 6.2: Sketch of the instrument location inside the basin during the WINGS experiment.

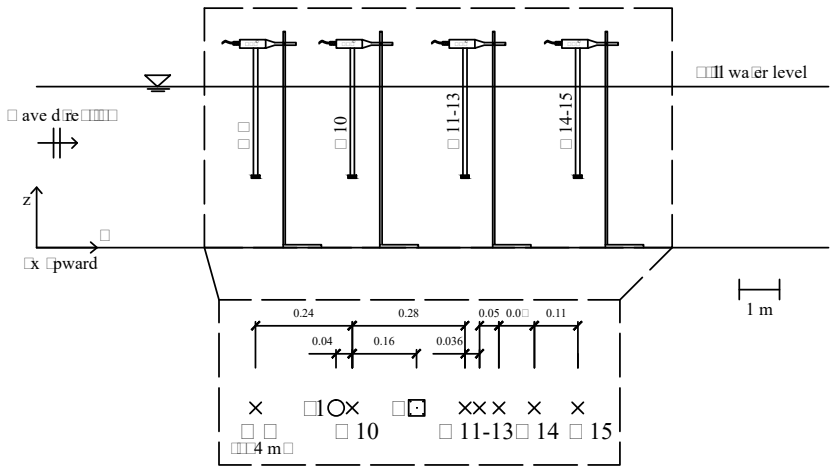

Figure 6.3: Sketch of the wave gauges aligned with vectrinos.

Table 6.1: Position of the wave gauges inside the basin.

Instrument name	Reference	x [m]	y [m]
Wave gauge 1	$W1$	13.5	4
Wave gauge 2	$W2$	13.5	6
Wave gauge 3	$W3$	13.5	8
Wave gauge 4	$W4$	16	4
Wave gauge 5	$W5$	16	5
Wave gauge 6	$W6$	16	6
Wave gauge 7	$W7$	16	7
Wave gauge 8	$W8$	16	8
Wave gauge 9	$W9$	18	4
Wave gauge 10	$W10$	18	5.2
Wave gauge 11	$W11$	18	6.6
Wave gauge 12	$W12$	18	6.78
Wave gauge 13	$W13$	18	7.02
Wave gauge 14	$W14$	18	7.46
Wave gauge 15	$W15$	18	8
Wave gauge 16	$W16$	19	6.2
Wave gauge 17	$W17$	19.5	4
Wave gauge 18	$W18$	19.5	5
Wave gauge 19	$W19$	19.5	6
Wave gauge 20	$W20$	19.5	7
Wave gauge 21	$W21$	19.5	8
Wave gauge 22	$W22$	21.5	4
Wave gauge 23	$W23$	21.5	6
Wave gauge 24	$W24$	21.5	8

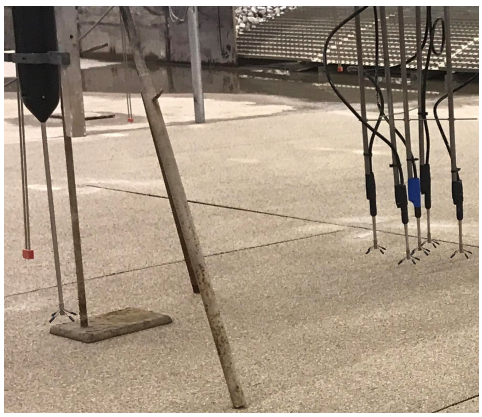

(a)

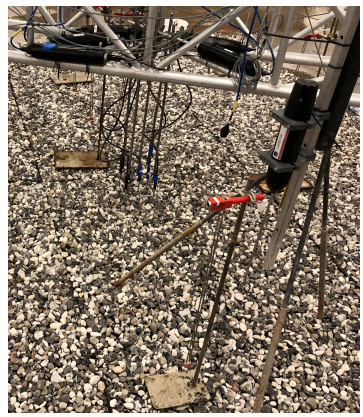

(b)

(c)

(d)

Figure 6.4: Vectrinos positioning: (a) sand bed; (b) gravel bed; (c) rippled bed; (d) seeding system.

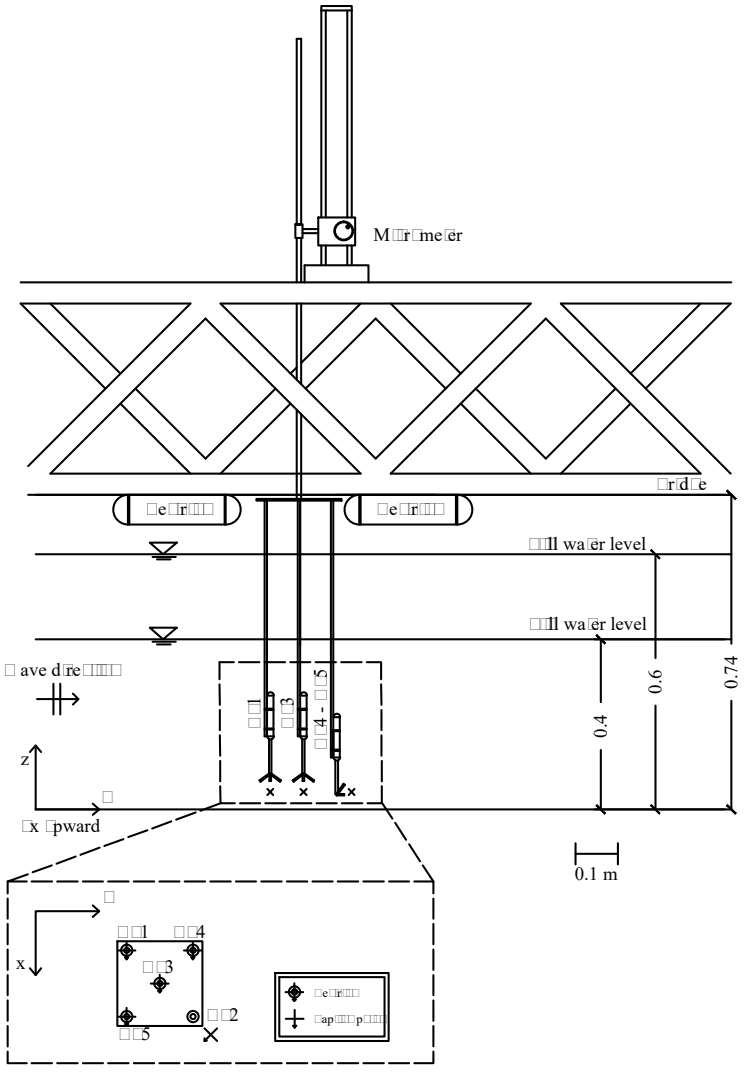

Figure 6.5: Position of the vectrinos on the sand and on the gravel bed.

6.1.1 Experimental procedure

Definition of time origin and instrument synchronization Measurement acquisition start after the reaching of stable flow conditions within the basin. Stable flow conditions are generally achieved after few minutes from the starting of both current and wave generation.

Wave gauges and vectrinos are synchronized by means of a TTL signal and acquired by means of the same data acquisition system.

The sample frequency of wave gauges is equal to 40 Hz, that of Vectrino Single Point was modified throughout the tests between 100 to 200 Hz, depending on the overall quality of the signal; finally the Profiler one was kept equal to 100 Hz.

Table 6.2: Position of the vectrinos for the sand and gravel bed.

Instrument name	Reference	x [m]	y [m]
Vectrino Profiler 1	VP1	18	5
Vectrino Profiler 2	VP2	19	6
Vectrino Single Point 1	VS1	17.88	6
Vectrino Single Point 2	VS2	18	5.88
Vectrino Single Point 3	VS3	18	6
Vectrino Single Point 4	VS4	18	6.12
Vectrino Single Point 5	VS5	18.12	6

Measured parameters After a calibration of the probe set, which was carried out once a day, in the early morning, the instantaneous water elevation is recovered, allowing both the wave height and period, respectively expressed in m and s, to be determined.

Velocity components in the three orthogonal directions along with the distance from the bed will be measured by the vectrinos (a single point measure for the Single Point vectrinos, a profile 0.034 m high for the profilers). Velocity components are expressed in m/s.

6.1.2 Organization of data files

The wave gauges data are stored as ASCII files containing a number of columns equal to the probe number and n rows, being n the time acquisition times the

frequency of acquisition set equal to 40 Hz. Each column is thus referred to the surface elevation measured by each probe; column separator is tabulation. Since the synchronization of the measurements is started by the wavemaker, also in the current only tests were acquired even in absence of waves. The wave software powered by DHI in this case allows the acquisition in case of "no waves". Each run is named as Txxxx.mat, where xxxx is a sequential number starting from 0001 to 1073.

Data files produced by Vectrino profilers are typically exported as binary $*$.mat files, where the velocity components are stored into the structure variables named *Data.Profiles_* followed by the velocity direction *VelX*, *VelY*, *VelZ1* or *VelZ2*. The vertical component is measured twice to serve as a reference value. Finally, the distance from the bed is stored into the variable *Data.BottomCheck_BottomDistance*.

Data files produced by Vectrino Single Point are typically exported both in ASCII files to be stored on the DHI server and in .hdr, .pck .dat files to be analysed in MATLAB environment. Vectrino Single Point files are named according to a univocal test naming, which includes the acronym of the considered instrument and a progressive number for tests, followed by an underscore and a progressive number for the position along the vertical profile, e. g. *VS2_run09_03_201802151427-11* will indicate the 9th test and the 3rd position along the vertical starting from the bed upward; also a suffix reporting year, month, day, hour, minutes and seconds was appended. Vectrino Profiler files are saved with progressive number for tests, followed by an underscore and a progressive number for the position along the vertical profile, followed by a suffix with day and year and the acronym of the Profiler, e.g. *run09_03_046.18.VP1.00000*.

6.1.3 Data processing

The signal post processing here described was adopted both for VSPs and for VP. Nevertheless, according to Thomas et al. (2017), 1, 2, 22-34 VP cells were considered not reliable and excluded from the analysis, see Paragraph 3.1.1.

In particular, the signal was despiked using the Goring and Nikora (2002) method. Thereafter, data characterized by COR < 65% or SNR $< 10dB$ were discarded. A zero up-crossing method was adopted to split the cleaned signal and to calculate the ensemble averaged velocities. Zeros were identified from the elevation measured by the resistive wave gauge closest to the vectrinos, i.e. $WG10$ for VSPs and $WG11$ for $VP1$, which signal was previously sampled at 200 Hz by the

linear interpolation. Finally, a matrix containing in each column a velocity fluctuation throughout a period and in each row a phase was arranged. Periods longer than 1.03 T or shorter than 0.97 T (generally 2-5 %) were rejected. Then the mean μ and the standard deviation std of each phase was calculated, discarding all items with values outside the threshold $\mu \pm 3std$. The phase mean was replaced by a NaN every time that each VSP or VP recorded less than 10 waves.

6.2 Experiments

Waves with periods between 1 and 2 s and wave heights between 0.05 m and 0.18 m were propagated along the basin. Two different water depths d have been considered, 0.4 and 0.6 m. In this way two different current conditions have been generated within the flume keeping the flow rate equal to 1 m^3/s. The combination of the wave and the current conditions led to reproduce both wave and current dominated regimes.

Some preliminary tests were performed in order to check the regularity of the flow within the test area and to set both the location of the rough panels inside the basin and the position of the instrumentation. First a Lagrangian particle tracking making use of neutrally buoyant particles allowed the large scale wave current interaction to be monitored and secondary flows to be investigated by means of visual inspection. One water depth (d=0.4 m), i.e. one current condition, and one wave condition (H=0.12 m and T=2 s) were selected in order to run this tests. After that a map of the flow conditions within the basin at one vertical position was carried out by means of one Vectrino single point. In this case a current only case (d=0.4 m) and a wave plus current one obtained by superimposing a wave (H=0.12 m and T=2 s) on the existing current were taken into account. Main goal was to check at what extent the velocity in the outer flow could be influenced by the local coordinate. The acquisition explored the area where the waves interact with the current, acquiring 14 measuring points in the current only case and 12 points in the wave plus current case (5 m$< x <$30 m; 3.5 m$< y <$8.5 m). Moreover, before starting with the test programme, a time convergence test has been performed, i.e. the velocity components were acquired at one point for 30 minutes and the convergence of the first and second order statistics have been analyzed by considering a different acquisition time. Moreover the comparison of the ensemble average with the single waves allowed to assess that no visible differences occurred within the acquisition time. This check ensured on the proper acquisition time for each measuring point. After these preliminary operations have been concluded, the trolley

with the instruments was positioned where the large scale wave current interaction reaches reasonably stable conditions. As soon as preliminary operations were completed, the test programme started. For each wave plus current condition, the current only and wave only conditions were also acquired separately.

In Tables 6.3 and 6.4 a summary of the experimental conditions is reported. Tables 6.3 and 6.4 indicate, for each of the performed tests with sand bed or gravel bed, the test type (current only CO, waves only WO, or waves plus currents WC), the water depth d, the wave characteristics, namely the wave height H and period T, the current velocity U_c, measured along x direction, the wave orbital velocity U_0 in the y direction and the velocity ratio U_c/U_0. On the complex 18 tests for each rough bed were performed.

Table 6.3: Hydraulic characteristics of the performed experiments at the DHI shallow water basin over a sand bottom.

	Test name	Test type	d $[m]$	H $[m]$	T $[s]$	U_c $[cm \cdot s^{-1}]$	U_0 $[cm \cdot s^{-1}]$	U_c/U_0 [-]
Sand bottom	Run_1	CO	0.4	-	-	24.76	-	-
	Run_{10}	CO	0.6	-	-	13.01	-	-
	Run_5	WO	0.4	0.08	1.00	-	8.88	-
	Run_9	WC	0.4	0.08	1.00	19.26	9.76	1.97
	Run_{16}	WO	0.6	0.08	1.00	-	5.59	-
	Run_{14}	WC	0.6	0.08	1.00	10.62	5.04	2.11
	Run_4	WO	0.4	0.08	2.00	-	14.92	-
	Run_8	WC	0.4	0.08	2.00	20.58	15.06	1.37
	Run_{15}	WO	0.6	0.08	2.00	-	12.34	-
	Run_{11}	WC	0.6	0.08	2.00	10.75	9.58	1.12
	Run_3	WO	0.4	0.12	2.00	-	22.27	-
	Run_7	WC	0.4	0.12	2.00	21.67	24.74	0.88
	Run_{17}	WO	0.6	0.12	2.00	-	18.91	-
	Run_{12}	WC	0.6	0.12	2.00	13.41	18.10	0.74
	Run_2	WO	0.4	0.18	2.00	-	26.83	-
	Run_6	WC	0.4	0.18	2.00	23.72	23.39	1.01
	Run_{18}	WO	0.6	0.18	2.00	-	28.76	-
	Run_{13}	WC	0.6	0.18	2.00	13.45	15.96	0.84

Table 6.4: Hydraulic characteristics of the performed experiments at the DHI shallow water basin over a gravel bottom.

	Test name	Test type	d $[m]$	H $[m]$	T $[s]$	U_c $[cm \cdot s^{-1}]$	U_0 $[cm \cdot s^{-1}]$	U_c/U_0 [-]
Gravel bottom	Run_{32}	CO	0.4	-	-	18.85	-	-
	Run_{19}	CO	0.6	-	-	11.59	-	-
	Run_{31}	WO	0.4	0.05	1.00	-	5.81	-
	Run_{28}	WC	0.4	0.05	1.00	20.43	4.87	4.20
	Run_{24}	WO	0.6	0.05	1.00	-	1.99	-
	Run_{20}	WC	0.6	0.05	1.00	11.04	1.95	5.66
	Run_{30}	WO	0.4	0.08	1.00	-	10.31	-
	Run_{35}	WC	0.4	0.08	1.00	21.13	8.70	2.43
	Run_{25}	WO	0.6	0.08	1.00	-	2.15	-
	Run_{21}	WC	0.6	0.08	1.00	8.60	3.65	2.35
	Run_{29}	WO	0.4	0.08	2.00	-	12.19	-
	Run_{33}	WC	0.4	0.08	2.00	21.79	17.14	1.27
	Run_{26}	WO	0.6	0.08	2.00	-	9.91	-
	Run_{22}	WC	0.6	0.08	2.00	10.81	13.21	0.82
	Run_{36}	WO	0.4	0.12	2.00	-	24.81	-
	Run_{34}	WC	0.4	0.12	2.00	23.03	24.29	0.95
	Run_{27}	WO	0.6	0.12	2.00	-	19.04	-
	Run_{23}	WC	0.6	0.12	2.00	7.80	14.35	0.54

In Table 6.5 the main non dimensional parameters, namely the current and the wave Reynolds numbers, along with the friction Reynolds number are reported for the performed experiments. They were calculated as:

$$Re_c = \frac{U_c \cdot d}{\nu} \qquad Re_w = \frac{U_0 \cdot A}{\nu} \qquad Re_c^* = \frac{u^* \cdot d}{\nu} \tag{6.1}$$

ν being the kinematic viscosity of water, A the wave orbital amplitude and u^* the friction velocity determined from velocity profiles in the current direction, as it will be shown in the next chapter.

Table 6.5: Main non dimensional parameters of the performed experiments at the DHI shallow water basin.

	Test name	Re_c [-]	Re_w [-]	Re_c^* [-]		Test name	Re_c [-]	Re_w [-]	Re_c^* [-]
Sand bottom	Run_1	99048	-	-	Gravel bottom	Run_{32}	75386	-	-
	Run_{10}	78063	-	-		Run_{19}	69523	-	-
	Run_5	-	1269	-		Run_{31}	-	548	-
	Run_9	77037	1519	2209		Run_{28}	81703	469	38058
	Run_{16}	-	499	-		Run_{24}	-	187	-
	Run_{14}	63704	404	1070		Run_{20}	66265	77	22797
	Run_4	-	7090	-		Run_{30}	-	1694	-
	Run_8	82330	7335	378		Run_{35}	84539	1212	11912
	Run_{15}	-	4859	-		Run_{25}	-	110	-
	Run_{11}	64515	3168	1220		Run_{21}	51619	283	14639
	Run_3	-	15800	-		Run_{29}	-	6312	-
	Run_7	86699	19494	16779		Run_{33}	87146	9370	14186
	Run_{17}	-	11403	-		Run_{26}	-	3379	-
	Run_{12}	80442	10484	2594		Run_{22}	64840	5575	19644
	Run_2	-	22923	-		Run_{36}	-	19597	-
	Run_6	94886	17661	14844		Run_{34}	92134	18842	30781
	Run_{18}	-	26344	-		Run_{27}	-	11570	-
	Run_{13}	80670	8186	2610		Run_{23}	46800	8730	10070

6.3 Analysis of results

Sections from one to three examine the nearshore hydrodynamics in a strictly two dimensional situation. Nevertheless, in nature waves and current interact at a certain angle, e.g. waves propagating orthogonally to the shoreline could interact with a longshore current. The following experiment aims to describe this occurrence paying particular attention to the nearbed hydrodynamics.

6.3.1 Water surface

Regular waves were measured by the wave gauges during all the tests, see Table 6.1 for gauges position inside the basin. Figure 6.6 show the wave series acquired during Run16 (SB, d=0.6 m; H=0.08 m; T=1 s, see Table 6.3) by the nearest wave gauge to the Vectrino Profiler, i.e. $W10$. In particular, Figure 6.6a reports the surface elevation measured throughout the test, starting one minute after the wavemaker launch. The reflection was mitigated by both the parabolic absorbers and the coarse beach. During the aforementioned test, the measured reflection coefficient was equal to 8%. Moreover, the maximum waves standard deviation was equal to 0.3 cm. Thus, waves were pretty constant throughout the test.

In Figure 6.6b the ensemble average is plotted above each single of the 180 recorded waves in Run16 (WO, d=0.6 m; H=0.08 m; T=1 s). The wave signal appears to be pretty regular and with good repeatability. A detail of the time series is also reported in Figure 6.6c.

The wave series acquired during Run14 (WC, d=0.6 m; H=0.08 m; T=1 s) are represented in Figure 6.7. The current superimposition increased the wave maximum standard deviation which became slightly smaller than 1 cm, see Figure 6.7a. This occurrence is related to the presence of a recirculating current which caused the direction of the wave propagation to vary throughout the test. Nevertheless, comparing Figure 6.7b and 6.6b it could be observed that the mean wave height did not change due to the presence of the current.

In the following Figure 6.8 the time-averaged wave height level is plotted in the sandy bed case. The vertical black lines correspond to the wave gauges located along the measuring area. More in details, Figure 6.8a refers to the case of current only (d=0.6 m), thus it indicates the water elevation above the mean level; since waves are not present, the blue surface is everywhere zero. Figure 6.8b and c respectively represent the wave only and the wave plus current cases. Looking at Figure 6.8b it is possible to observe that there is a shadow zone close to WG19-21 (coordinate x going from 14 to 16 m and coordinate y going from 4 to 9 m),

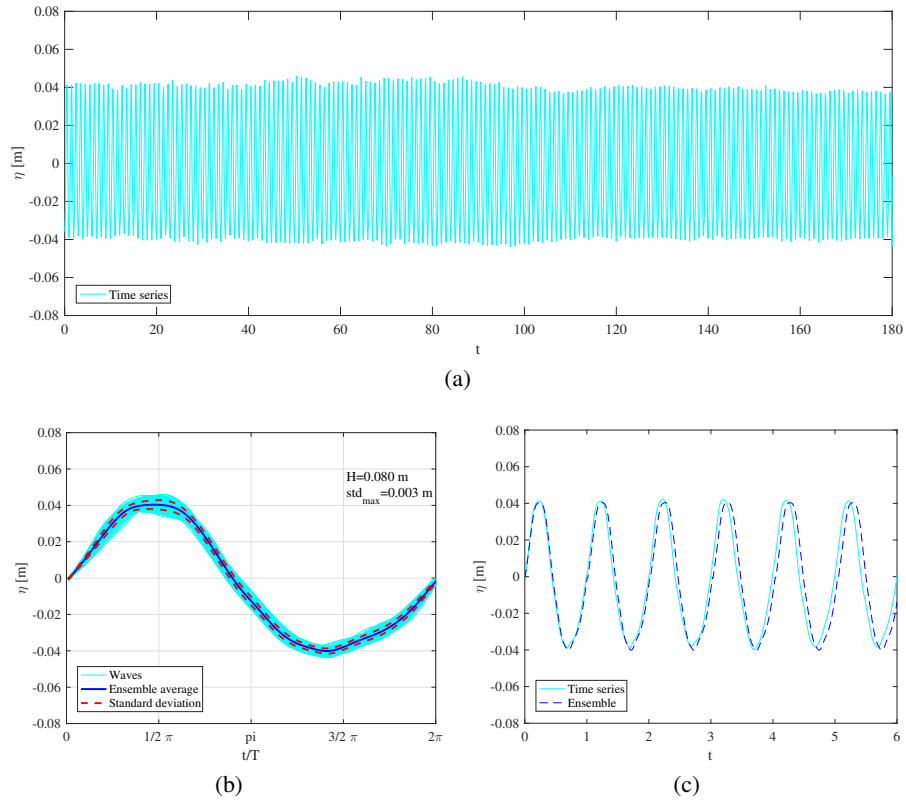

Figure 6.6: Wave series acquired during Run16 (d=0.6 m; H=0.08 m; T=1 s) by $W10$.

where the wave propagation is sheltered by the bridge and wave height is small if compared to those measured moving along the x axis, at the same ordinate ($y \approx 7$ m). Here the wave height is about 0.07 m, while elsewhere it is close to the target value. In the wave plus current case, Figure 6.8c, the shelter effect at WG19-21 is avoided by the current itself which spreads and levels the mean wave height; indeed wave height is almost constant everywhere apart from a margin area close to WG1-3 (coordinate x going from 14 to 16 m and coordinate y going from 4 to 9 m), where the wavemaker fronts end.

Similarly, in Figure 6.9 the time-averaged wave height level is plotted in the gravel bed case, for current only, wave only and wave plus current respectively in

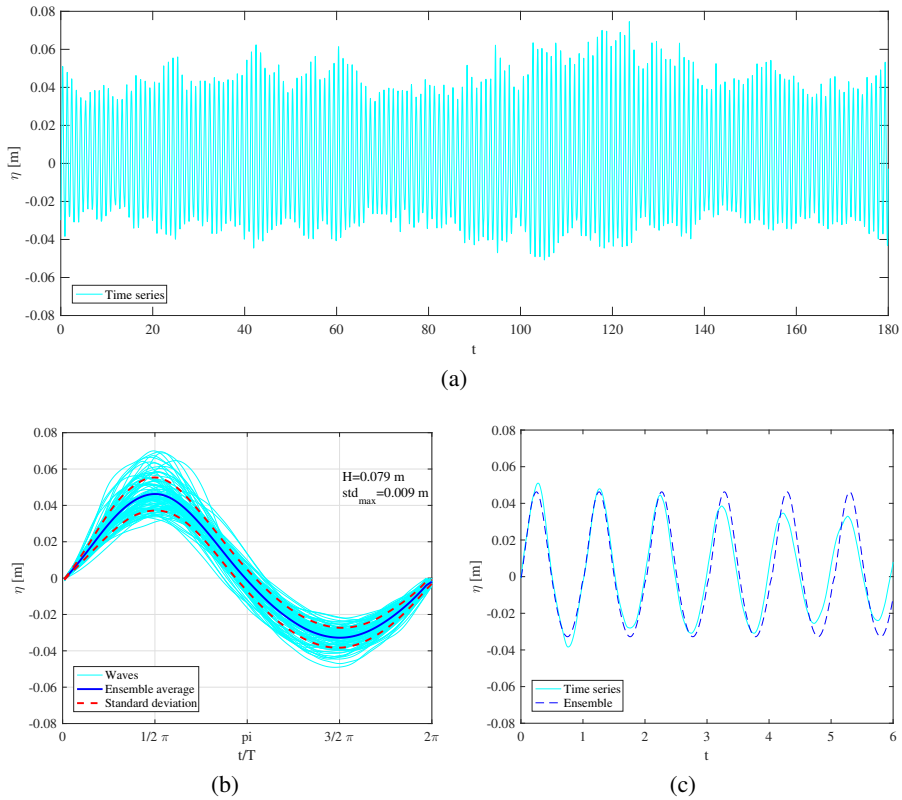

Figure 6.7: Wave series acquired during Run14 (d=0.6 m; H=0.08 m; T=1 s) by $W10$.

Figure 6.9 a, b and c. Results are pretty similar to the case of sandy bed.

In Figure 6.10 the time variability of the wave heights is plotted as reference for Run14 (d=0.6 m, H=0.08 m, T=1 s). In the picture each subplot is referred to each measuring gauge and reports the mean wave height recorded during each test (1-16) of the run, along with the offset and the reference zero-level. As it can be viewed by looking at each subplot, the wave height maintains the same value for all the run duration (i.e. from test 1 to 16 of the same run) at each gauge location. Comparing this picture with 6.8 and 6.9 the same considerations arise: indeed the spatial variability is limited to the border of the wave generation area.

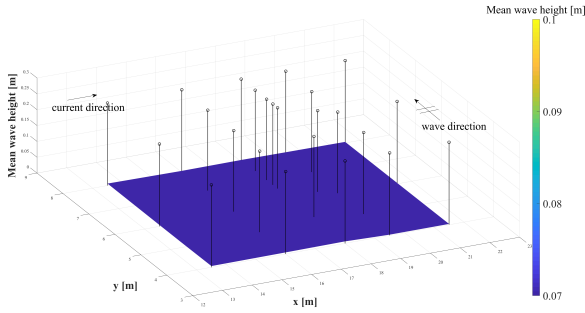

(a)

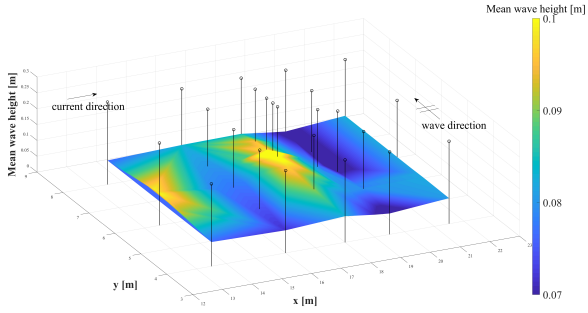

(b)

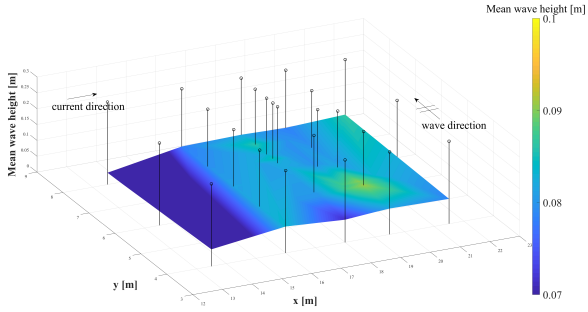

(c)

Figure 6.8: Time-averaged wave heights in the SB case (d=0.6 m): a) Run10 (CO); b) Run16 (WO, H=0.08, m T=1 s); c) Run14 (WC, H=0.08, m T=1 s)

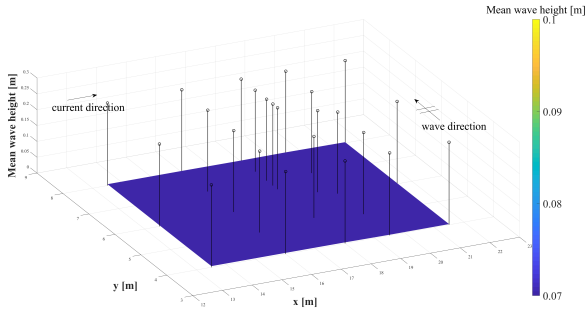

(a)

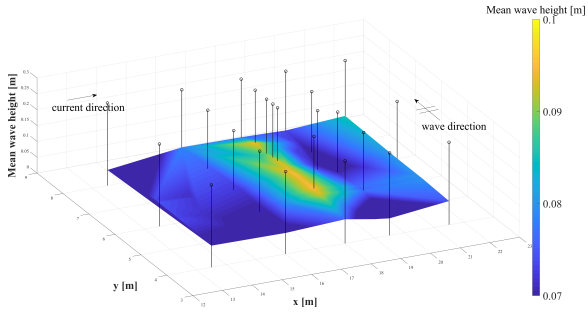

(b)

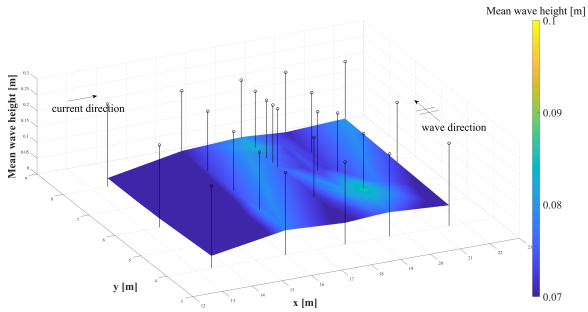

(c)

Figure 6.9: Time-averaged wave heights in the GB case (d=0.6 m): a) Run19 (CO); b) Run25 (WO, H=0.08, m T=1 s); c) Run21 (WC, H=0.08, m T=1 s)

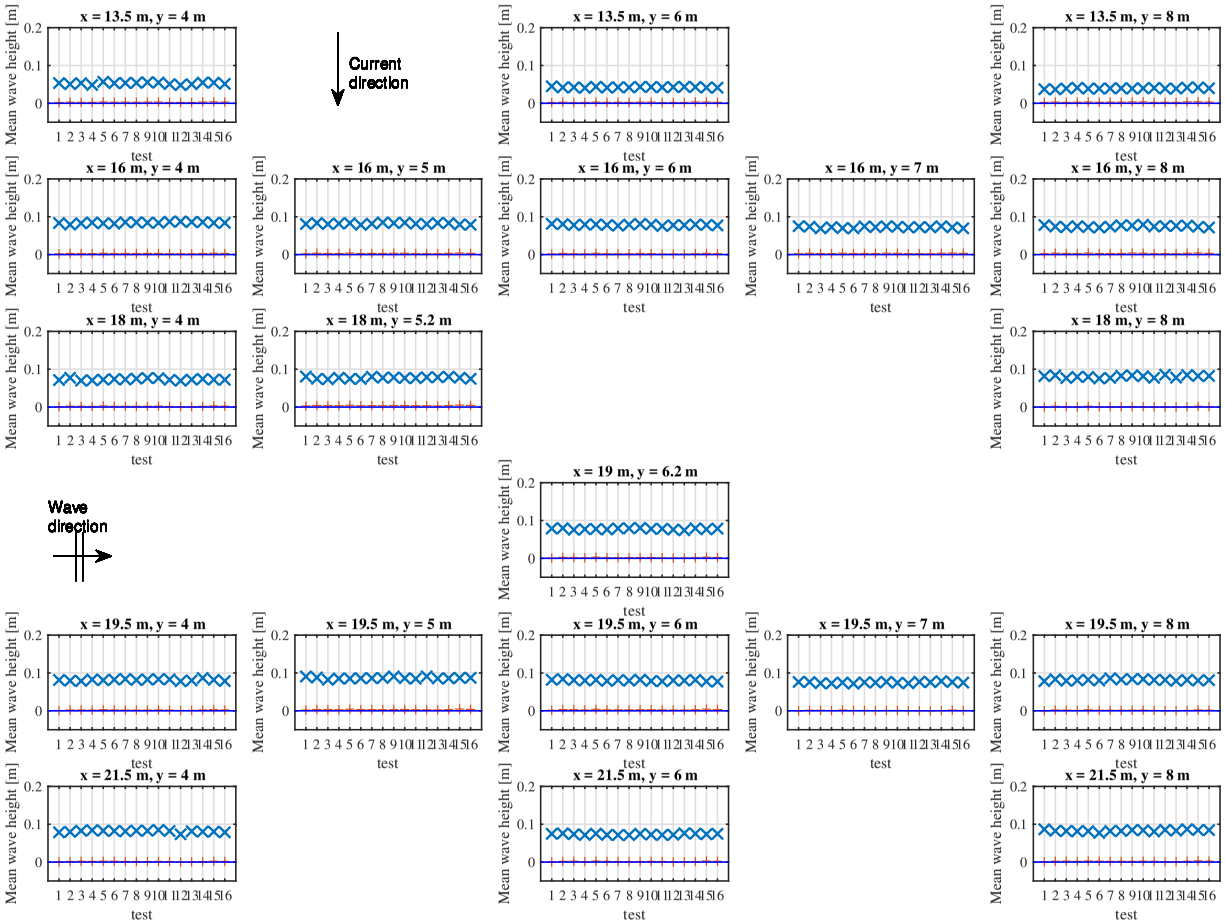

Figure 6.10: Time wave height variability within the tank at each gauge during all the tests of Run14 (d=0.6 m, H=0.08 m, T=1 s). The blue line indicates the zero level, the x symbols refer to the mean height during each test, the + symbols refer to the gauge offset.

6.3.2 Velocity profiles

In this section velocity profiles acquired by Vectrino Single Point and Vectrino Profiler are shown separately for mean flow ad phase averaged flow. In Table 6.6 the position of each Vectrino within the tank is reported.

Table 6.6: Position of the vectrinos for the sand and gravel bed

Instrument name	Reference	x [m]	y [m]
Vectrino profiler 1	VP1	18	5
Vectrino profiler 2	VP2	19	6
Vectrino single point 1	VS1	17.88	6
Vectrino single point 2	VS2	18	5.88
Vectrino single point 3	VS3	18	6
Vectrino single point 4	VS4	18	6.12
Vectrino single point 5	VS5	18.12	6

Mean flow As mentioned before, for each test the velocity was acquired by means of several vectrinos, which were then averaged in order to obtain a mean velocity. An example of this procedure is shown in Figure 6.11 where the velocities acquired by each vectrino in two current only tests characterized by a water depth d=0.4 m are reported all together along with the averaged profile. In particular, Figure 6.11a and 6.11b report respectively the x- and y-component in Run1, i.e an SB case, while Figure 6.11c and 6.11d similarly represent x- and y-component in Run32 which correspond to a GB experiment. The velocity is made non dimensional by means of the target current velocity. It is possible to observe that in the SB case the measured velocities are almost superimposed one with each other at all the measuring stations, both in the current and in the wave direction. The y component shows an irregular pattern which leads to suppose the existence of transverse circulation inside the basin at different depths. In the GB case on the contrary, the scatter between each vectrino single point is more relevant (up to 20% in the weak spot region), even though the averaged profile is less affected by abrupt changes.

For the sake of completeness the velocity profiles measured by the VSPs together with the averaged profile, in the case of d=0.6 m, are reported in Figure 6.12. More in detail, Figures 6.12a, b show the velocity profiles measured above

the sand bottom, respectively along the directions x and y; likewise, Figures 6.12c, d show the velocity profiles measured above the gravel bottom. Both Run10 and Run19 U_y velocities considerably vary throughout the water depth. The smaller values are reached at the bottom due to the no slip condition and at the elevation of $z/d \approx 0.2-0.3$. Few centimetres above and below $U_y \approx 0.5U_c$ due to the aforementioned transverse circulation.

In order to quantify the veering of the velocity with respect to the x-direction, the angle of the velocity vector with respect to the current propagation direction is reported in Figure 6.13 for the same four runs discussed above, i.e. Run1 (SB), Run32 (GB), Run10 (SB), Run19 (GB). Independently on the rough bed and on the water depth, at the bottom the veering trend is maximum, reaching 50-60° in the case of $d = 0.4$m and 80-90° in the case of $d = 0.6$m, while up above it reaches average values between 11 and 14° in the case of $d = 0.4$m and 20-30° in the case of $d = 0.6$m.

At $d = 0.6$m the current velocity was smaller due to the continuity principle. The water depth increasing affected particularly the U_c component along the x direction, thus augmenting its veering from the direction of the current propagation. Veering was maximum at $z/d < 0.1-0.2$ where velocities were small due to the interaction with the bottom.

The presence of a transverse circulation could be observed by comparing the velocities measured along the vertical direction by the Vectrinos Single Point and the Vectrino Profiler throughout the current only tests: Run1, Run10, Run19, Run32. Vectrinos Single Point measured a downward component of the velocity at each run which was nearly constant throughout the water depth, see Figure 6.14. More in detail, at each elevation, VS1 measured the biggest negative velocities both during Run10, Run19 and Run32. Analogously, VS4 measured the smallest velocities during the four tests. Such behaviour did not appear when VSPs measured the velocities along the two horizontal directions and suggests that the vertical component of the velocity slight varied with the measuring station. The presence of a three-dimensional circulation is confirmed by the vertical velocities measured by the Vectrino Profiler which were considerably smaller with respect to velocities measured by VSPs and slightly constant throughout the four runs, see Figure 6.15.

In Figure 6.16 a comparison between the velocity profiles acquired in the current direction for a current only, a wave only and a wave plus current condition is shown. More in detail, Run1 (CO), Run3 (WO), Run7 (WC) are plotted (d=0.4 m, H=0.12 m, T=2 s) in linear scale (Figure 6.16a) and in log scale (Figure 6.16b),

this latter limited to CO and WC runs. Run7 belongs to the current dominated (CD) conditions.

While the wave only profile, as expected, shows only fluctuations around zero, the CO and WC profiles exhibit an increasing velocity from the bottom up to about 0.2-0.3z/d. Here only the mean profile is plotted but the variability observed among the different vectrinos is still depicted in terms of an errorbar. Such variability is maximum at the bottom and almost disappears when moving away from the bed. To easily compare the CO and the WC profiles, they were also plotted in log-scale, highlighting in this way the existence of a logaritmic layer. According to Fredsøe et al. (1999) the upper limit of the boundary layer was established equal to 0.17 d_{50}.

Figure 6.16 (c), (d) show respectively the velocity profiles and the logarithmic profiles measured by the Vectrino Profiler VP1. Both profiles are in good agreement with the profiles measured by the Vectrinos Single Point throughout Run1, 3 and 7. The wave superimposition causes the velocities to decrease in the inner flow, i.e. $z/d < 0.2$ ($z < 8cm$) and the velocity to increase in the outer flow. The Vectrino Profiler VP1 was closer to the wavemaker than the Vectrinos Single Point. There the current veering was smaller and the bridge sheltering did not affect the waves. Thus velocities are bigger throughout the water depth if compared with the velocities measured by the Vectrinos Single Point. In particular, such effect hid the near bed steady offshore directed flow during the wave only test (Run3) which occurred due to the wave asymmetry (Scandura, 2007).

Similarly, Figure 6.17 show a current only, a wave only and a wave plus current conditions still over a sandy bed but in a wave dominated regime. Here Run10 (CO), Run17 (WO), Run12 (WC) are deployed (d=0.6 m, H=0.12 m, T=2 s).

In the GB case, the current only, wave only and wave plus current profiles are reported in Figures 6.18 and 6.19 respectively in the current dominated and in the wave dominated regime.

Along the y-direction (Figure 6.20), time averaged profiles show that in the case of wave only the mean velocity is negative for both SB and GB case for the majority of the vertical profile due to the settling of the undertow currents. The current only exhibits a not null component even in the wave direction due to the veering of the flow, as mentioned before; the addition of the wave onto the current tends to compensate these two opposite flows, with a mean profile that shows, on the complex, velocities smaller than in the current only case.

Representing the angle formed by the flow with the x-axis in the wave plus current condition, it can be noticed in Figure 6.21 that similarly to the current only

case, the veering of the flow tends to decrease far from the bed. Except from the bed, the angle formed with the x-axis is smaller than in the current only case, both in the sand bed case (Figure 6.21a) and in the gravel bed case (Figure 6.21b), i.e. the addition of the waves limits such veering behaviour. In order to investigate to what extent this happens, the mean angle formed by the flow outside the boundary layer was investigated as function of the current to wave ratio U_c/U_w, where U_c was deduced by the flow rate and $U_w = H\omega/(2sinh(kd))$. The results are exposed in Figure 6.22. Data are here grouped depending on the rough bed condition (GB or SB) but in both cases, even with a high dispersion, the angle formed with the x-axis tend to decrease as the velocity ratio increases.

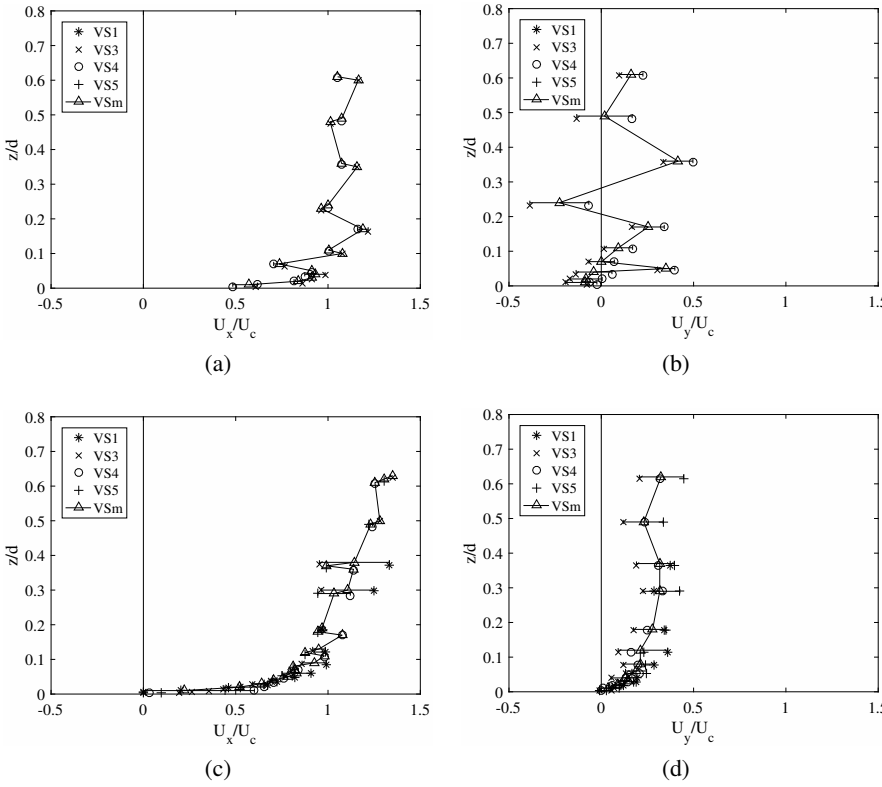

Figure 6.11: Mean velocity profiles acquired by the Vectrinos in the current only case (d=0.4 m): a) Run1 (CO, SB) Ux; b) Run1 (CO, SB) Uy c) Run32 (CO, GB) Ux; d) Run32 (CO, GB) Uy.

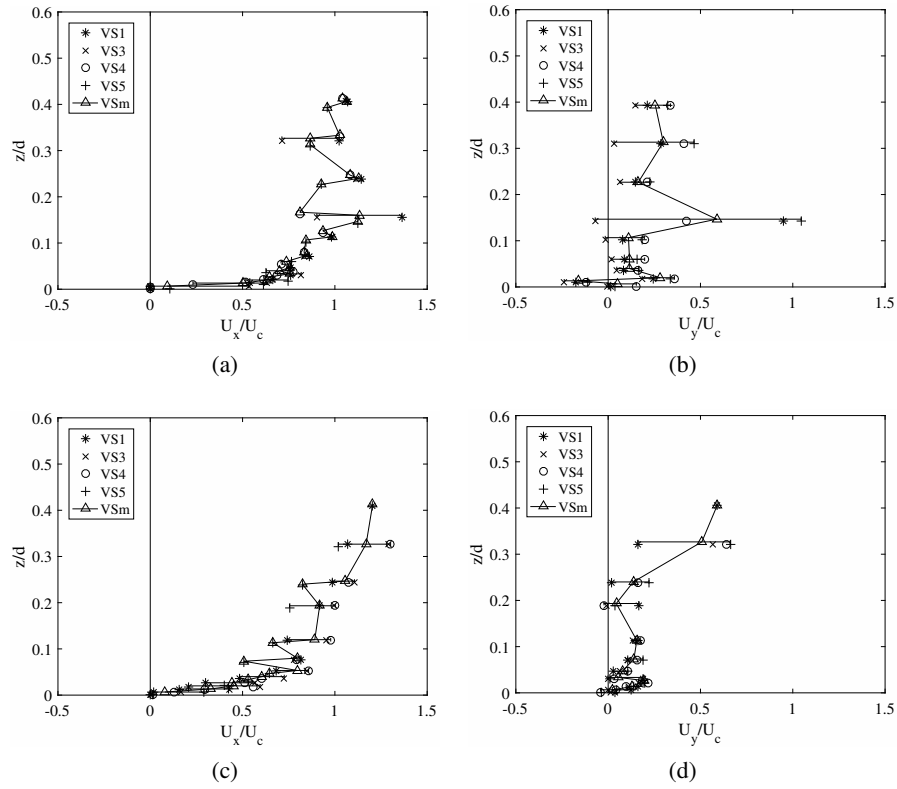

Figure 6.12: Mean velocity profiles acquired by the Vectrinos in the current only case (d=0.6 m): a) Run10 (CO, SB) Ux; b) Run10 (CO, SB) Uy c) Run19 (CO, GB) Ux; d) Run19 (CO, GB) Uy.

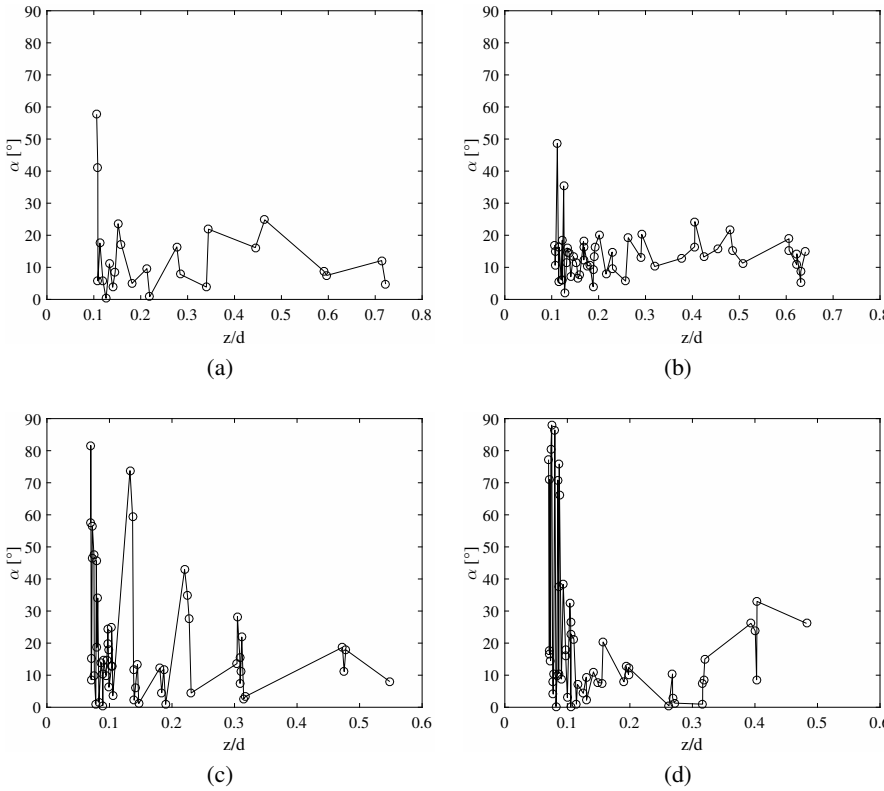

Figure 6.13: Mean flow direction in the current only case: a) Run1 (d=0.4 m, SB); b) Run32 (d=0.4 m, GB); c) Run10 (d=0.6 m, SB); d) Run19 (d=0.6 m, GB).

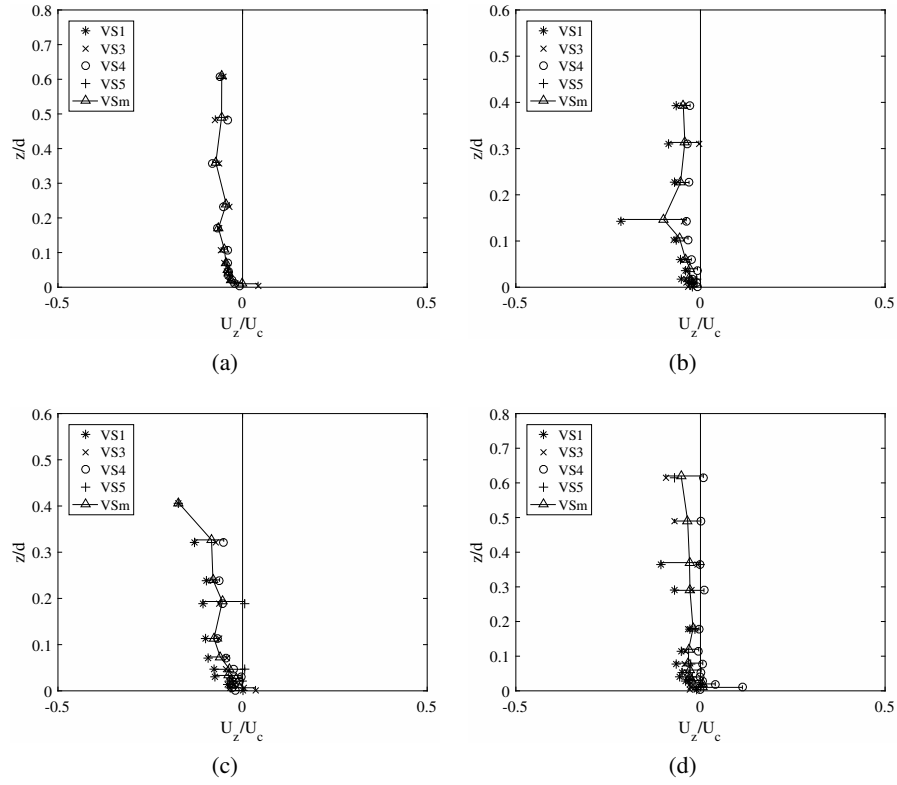

Figure 6.14: Mean velocity profiles acquired by the Vectrinos in the current only case along the vertical direction (d=0.4 m): a) Run1 (CO, SB); b) Run10 (CO, SB); c) Run19 (CO, GB); d) Run32 (CO, GB).

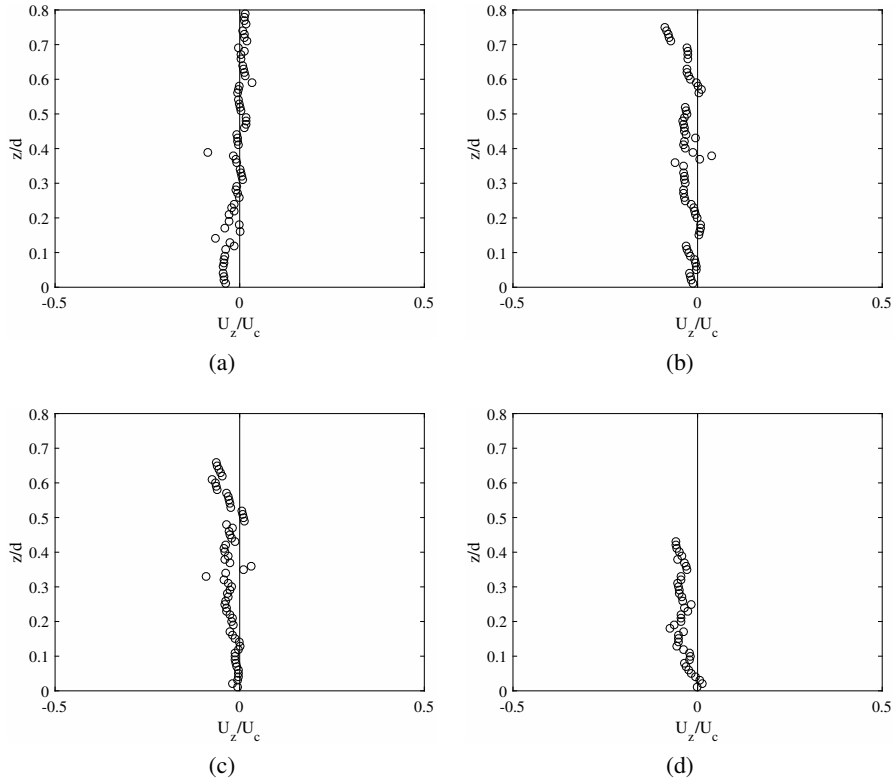

Figure 6.15: Mean velocity profiles acquired by the Vectrino Profiler VP1 in the current only case along the vertical direction (d=0.4 m): a) Run1 (CO, SB); b) Run10 (CO, SB); c) Run19 (CO, GB); d) Run32 (CO, GB).

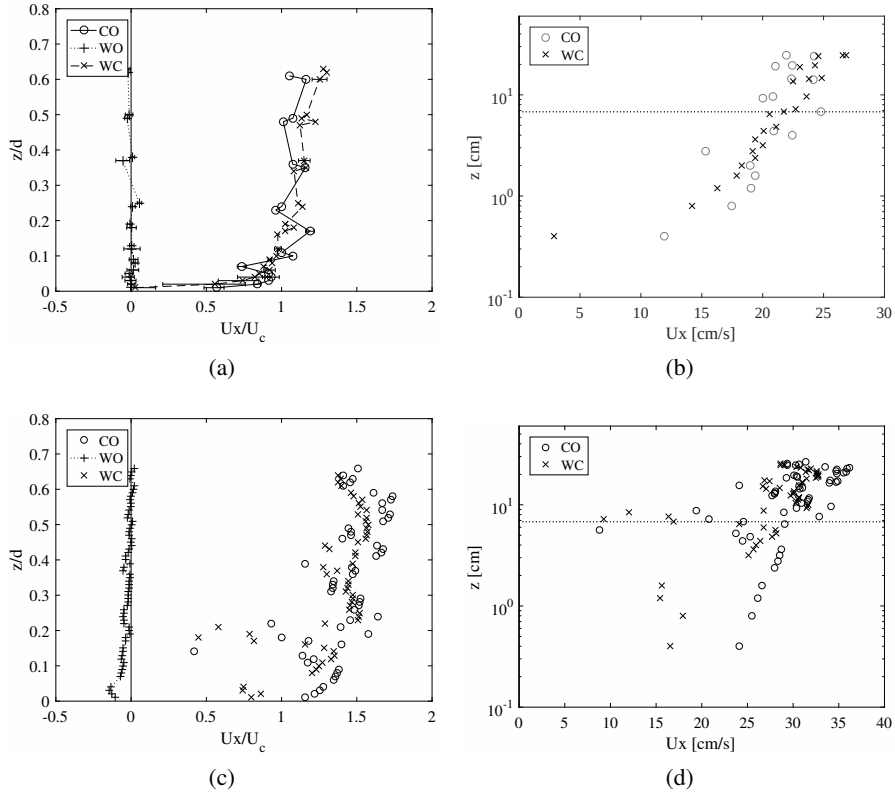

Figure 6.16: Velocity profiles along the x direction in the SB case Run1 (CO), Run3 (WO), Run7 (WC, CD) d=0.4 m, H=0.12 m, T=2 s, (a) VS1-VS5, (c) VP1; logarithmic profile of Run1 (CO) and Run7 (WC, CD) (b) VS1-VS5, (d) VP1.

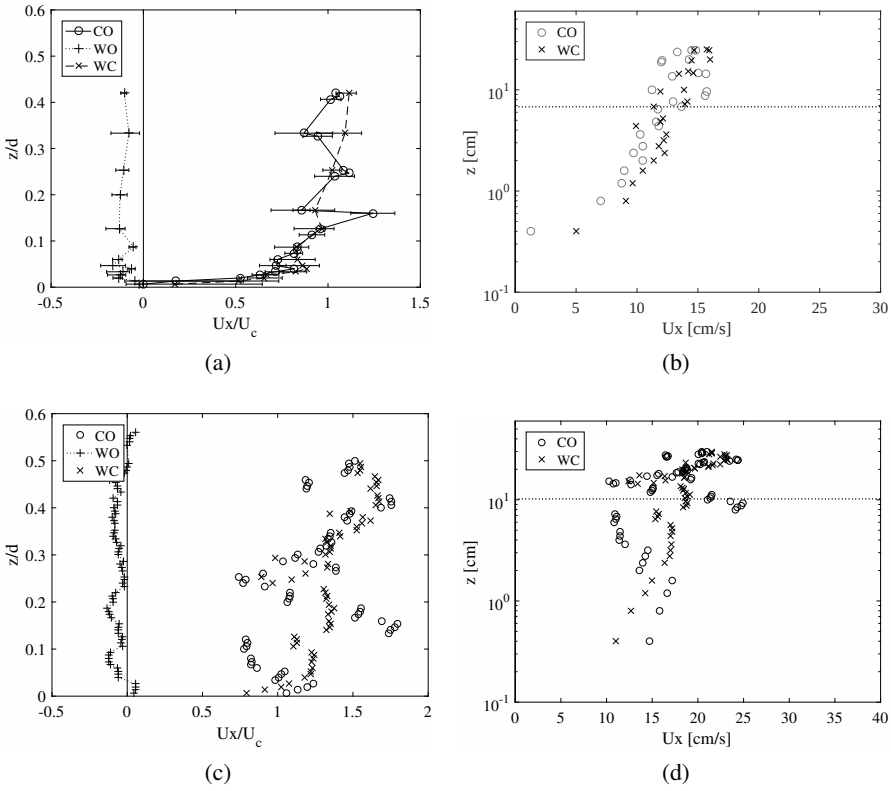

Figure 6.17: Velocity profiles along the x direction in the SB case Run10 (CO), Run17 (WO), Run12 (WC, WD) d=0.6 m, H=0.12 m, T=2 s (a) VS1-VS5, (c) VP1; logarithmic profile of Run10 (CO) and Run17 (WC, WD) (b) VS1-VS5, (d) VP1.

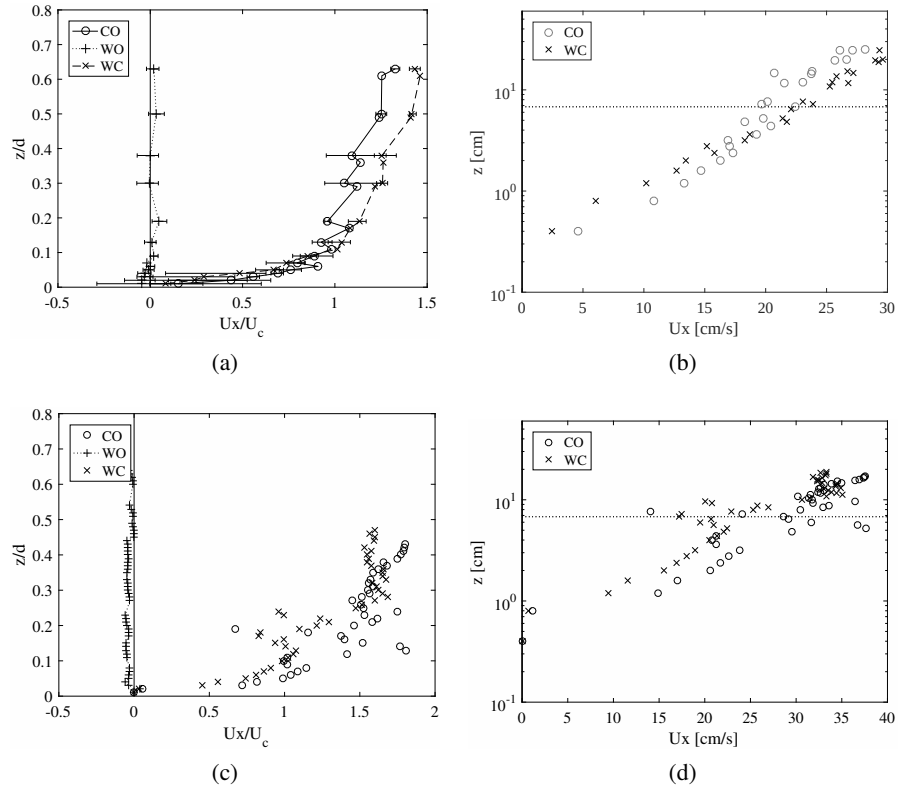

Figure 6.18: Velocity profiles along the x direction in the GB case Run32 (CO), Run36 (WO), Run34 (WC, CD) d=0.4 m, H=0.12 m, T=2 s (a) VS1-VS5, (c) VP1; logarithmic profile of Run32 (CO) and Run34 (WC, CD) (b) VS1-VS5, (d) VP1.

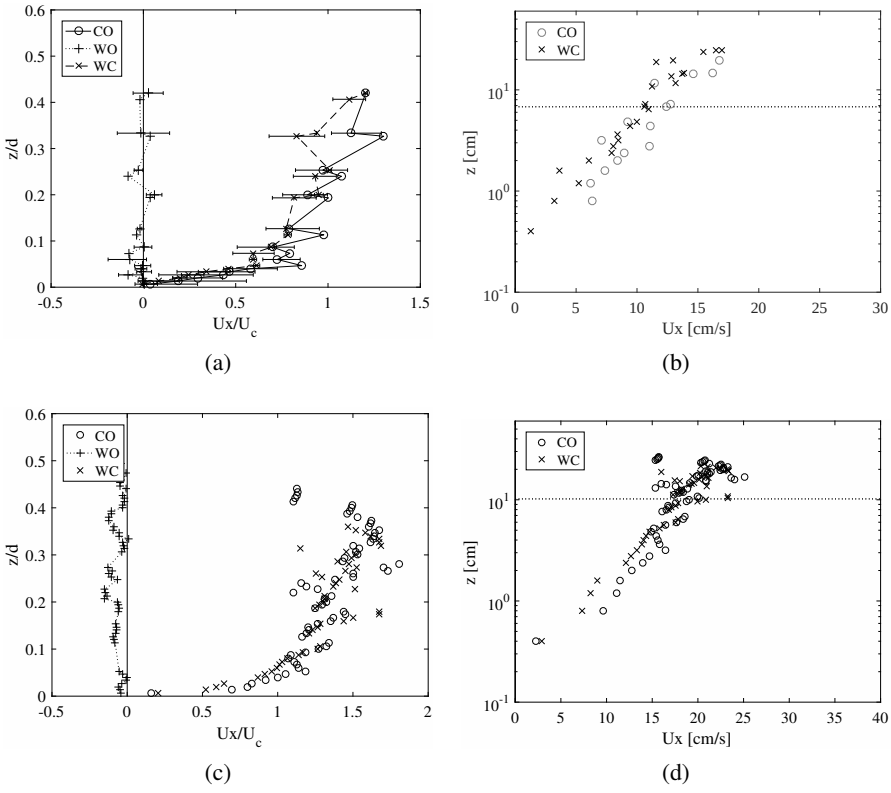

Figure 6.19: Velocity profiles along the x direction in the GB case Run19 (CO), Run26 (WO), Run22 (WC, WD) d=0.6 m, H=0.12 m, T=2 s (a) VS1-VS5, (c) VP1; logarithmic profile of Run19 (CO) and Run22 (WC, WD) (b) VS1-VS5, (d) VP1.

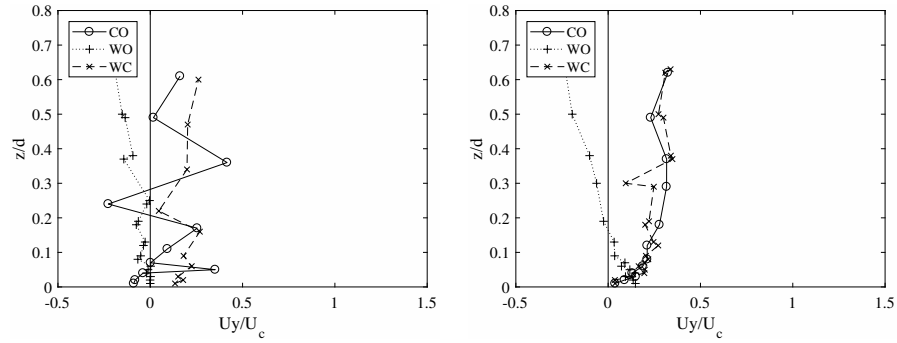

Figure 6.20: Velocity profiles along the y direction in the SB case case, Run1 (CO), Run3 (WO), Run7 (WC, CD) (a), and GB case, Run32 (CO), Run36 (WO), Run34 (WC, CD) (b). d=0.4 m, H=0.12 m, T=2 s.

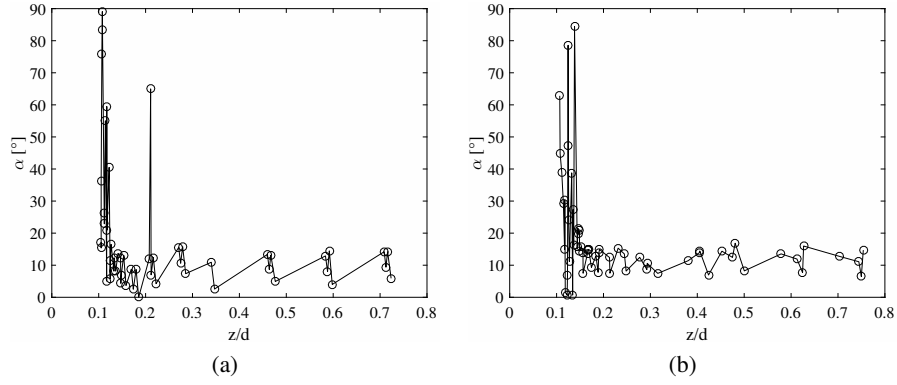

Figure 6.21: Flow direction in the wave plus current case: a) Run7 (SB); b) Run34 (GB) d=0.4 m, H=0.12 m, T=2 s.

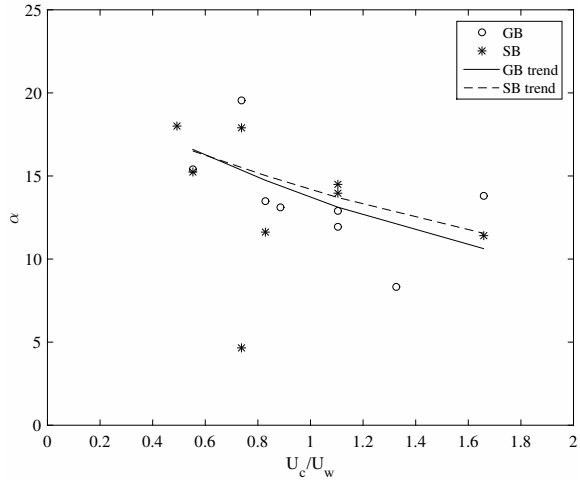

Figure 6.22: Mean flow direction versus the current to wave velocity ratio.

Shear stresses Following Fredsøe et al. (1999) it is possible to interpolate the already shown logarithmic profiles in order to determine the equivalent roughness k_s and the friction velocity u^* as 30 times the intercept and as the angular coefficient respectively. This is shown in Figures 6.23 and 6.24 respectively in the SB and GB cases. On the left side (a) in both pictures a current dominated situation is represented, while on the right side (b) a wave dominated one is depicted.

In the plots, a linear interpolation of both the CO and the WC data within the log layer is superimposed on the data. It is possible to observe how close to the bottom the addition of the wave onto the current leads the flow to decelerate, accordingly to what already observed by Musumeci et al. (2006) and Faraci et al. (2008). This is true for the observed tests with the exception of the wave dominated case in the presence of the sand bed. This behaviour can be better understood by looking at Figure 6.25a, where the non dimensional wall shear stress, obtained as the ratio of the wave-current shear stress to the current only one, is plotted versus the wave Reynold number. Data are grouped on the basis of the rough bed. In the SB case it may be noticed that at low Reynolds numbers, between 5000 and 6000, the non dimensional wall shear stress undergoes a reduction, i.e. the flow relaminarizes as already observed by Lodahl et al. (1998) and Faraci et al. (2008).

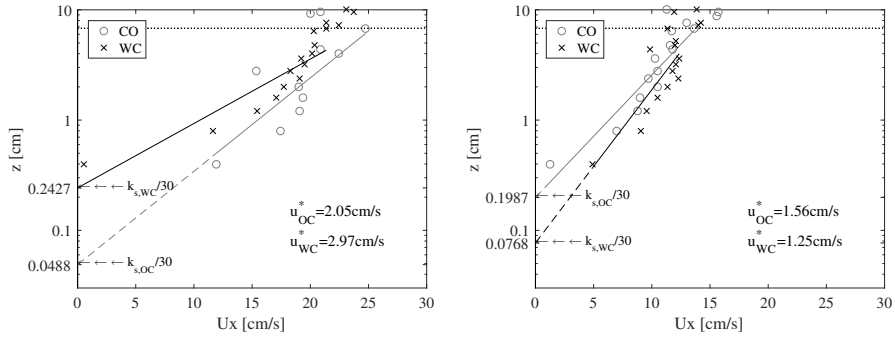

(a) (b)

Figure 6.23: Logarithmic profiles in the SB case Run1 (CO), Run7 (WC, CD) d=0.4 m, H=0.12 m, T=2 s (a); Run10 (CO), Run12 (WC, WD) d=0.6 m, H=0.12 m, T=2 s (b).

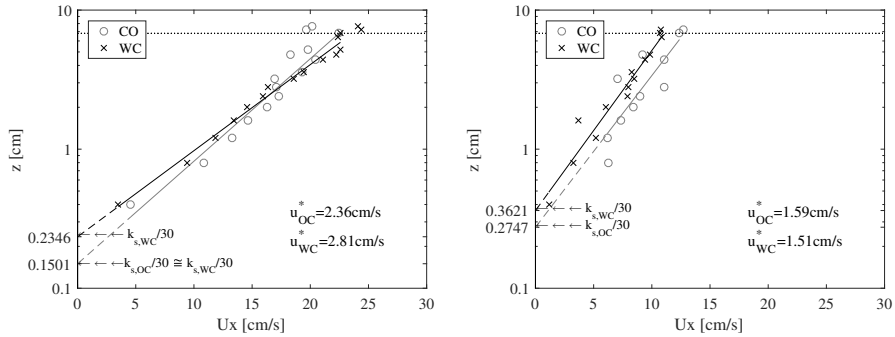

(a) (b)

Figure 6.24: Logarithmic profiles in the GB case Run32 (CO) and Run34 (WC, CD) d=0.4 m, H=0.12 m, T=2 s (a); Run19 (CO), Run22 (WC, WD) d=0.6 m, H=0.12 m, T=2 s (b).

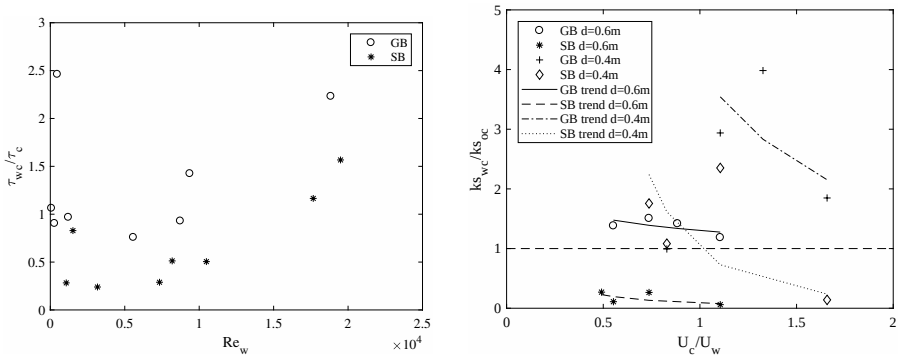

(a) (b)

Figure 6.25: (a) Non dimensional wall shear stress as a function of wave Reynolds number; (b) non dimensional equivalent roughness versus the current to wave velocity ratio.

Then, it resumes to increase and at about $1.5{\cdot}10^4$, it overcome unity, i.e. a non-linear increase of the shear stress takes place.

Figure 6.25b shows how the non dimensional equivalent roughness $ks_{\mathrm{wc}}/ks_{\mathrm{co}}$ in the direction of the current propagation changes with respect to the current to wave velocity ratio. Both the SB and GB trend for $d = 0.6$m lies within the wave dominated field $U_c/U_w < 1$ and are slightly affected by the magnitude of wave velocity U_w. This dependence could be related to the wave slope, being $U_w \sim H/T$, thus to the flow acceleration, according to Flores and Sleath (1998), Camenen et al. (2009) and Nielsen (1992). However, above the two beds, the non dimensional roughness behaviour is quite different. Indeed, above the sand bottom the wave superimposition induces the flow to relaminarize, thus reducing the equivalent roughness $ks_{wc}/ks_{oc} < 1$. According to Lodahl et al. (1998), this phenomenon could occur only in presence of a laminar boundary layer and wave dominated conditions. Above the gravel bottom, the considerable bed roughness causes the boundary layer to become turbulent, thus impeding this phenomenon to occur. Finally, the non dimensional roughness varies considerably within the current dominated field $U_c/U_w > 1$. In such case, the non dimensional roughness has an inverse relationship with the current velocity and, as a consequence, with the current Reynolds number. Such equivalent roughness behaviour occurs similarly in the steady flow, outside the fully turbulent regime.

6.4 Discussion

The hydrodynamics of the coastal region is usually characterized by the simultaneous presence of waves and currents. A wave field superimposed on a steady current can significantly change the mean velocity profile and the turbulent properties of the current close to the bottom. Because of the complexity of this phenomenon, theoretical investigations are rare. Moreover, the continuously changing characteristics of waves and currents, which can cross at any angle, make impossible to perform a systematic investigation in the field. Thus, most experimental studies were carried out in laboratory, notwithstanding the presence of unavoidable scale effects.

The case of waves and current crossing at a right angle was here examined over either a sand d_{50}=0.9 mm) or a gravel (d_{50}=2.5 cm) bottom. The work was aimed at understanding how the vertical velocity profile of a steady current is affected by the presence of a wave which propagates in the direction orthogonal to the current.

Throughout the experiments, waves broke on the parabolic absorbers causing the undertow to appear throughout the measured water depth. Moreover, a transverse circulation was measured inside the basin due to the different length of the current inlet from the outlet which was wider. Such a circumstance lead velocity to veer with respect to the direction of the current propagation x of about 50-60° at the bottom and 11-14° in the outer flow. Thus, during the current only tests, velocities were not null in the direction of the wave propagation y.

Particular attention was given to the boundary layer and its modification both in terms of the Nikuradse equivalent roughness k_s and of the friction velocity u^* due to the wave on current superimposition. More in detail, two behaviours were detected. In the wave dominated regime $U_c/U_w < 1$ the equivalent roughness was slightly affected by the wave superimposition, whereas it became up to three times bigger in the current dominated regime $U_c/U_w > 1$, thus causing the near bed flow to become slower. Furthermore, within the current dominated regime, the equivalent roughness decreased with the Reynolds number increasing as occurs in the steady flow, outside the fully developed turbulent regime. Finally, according to Lodahl et al. (1998) and Faraci et al. (2008), at low Reynolds number and above the sand bottom, the waves on current superimposition caused the flow to relaminarize. This phenomenon did not occur on the gravel bottom. There, the considerable roughness cause strong near bed turbulences, which did not allow the boundary layer to be laminar.

7 Conclusions

A wave propagating over a sloping beach undergoes substantial modifications. In the nearshore zone, the interaction with the seabed causes the wave to become skewed and asymmetric, i.e. with the trough broader and the crest shaped. Moreover, the turbulence asymmetry in successive wave half-cycles (beneath asymmetric forcing) and the presence of a vertical wave velocity within the seabed boundary layer cause respectively the wave asymmetry steady streaming and the Longuet-Higgins steady streaming to appear near the bottom. These two mechanisms act in opposite ways. The asymmetry steady streaming causes an offshore directed flow, whereas the Longuet-Higgins steady streaming causes an onshore directed flow. Finally, in the surf zone, the wave breaking cause a considerable increase in the flow turbulence. Here, in the proximity of the water surface, the Stokes drift combined to the action of the surface rollers produce a shoreward flux which, in a strictly two-dimensional situation, is balanced by a strong seaward current that is called undertow.

These mechanisms give rise to a complex flow which, over a non-cohesive bed, could trigger the appearance of small scale bedforms known as ripples. The ripple growth, in turn, increases the seabed roughness and affects the near bed flow where the so-called recirculating cells appear. Ripple shape reflects the wave shape at a certain depth whereas ripple migration is considerably affected by the flow turbulence and by the direction of the steady flow. Thus, in the deep water ripples are often symmetrical, i.e. the offshore half-wavelength is equal to the onshore half-wavelength, and migrate around an equilibrium position. Otherwise, in the shallow water, where the bed slope is significant, ripples could be considerably asymmetrical and could migrate offshore or onshore.

The hydrodynamics in the nearshore zone was described throughout this Ph.D. thesis by means of the experimental results of three campaigns. The complex interaction between wave and currents and its influence on the coastal morphodynamics was analysed.

A non-cohesive sandy beach was built within the small-scale wave flume of

the University of Messina (Italy). Throughout the experiments, the characteristics of flow and bedforms at two sections of the beach were examined and compared. The first section was located in the deep water where the bottom is horizontal, whereas the second one was located in the shallow water, where the bottom was sloped. Above the horizontal bed, the Longuet-Higgins shoreward steady streaming was measured. Ripples appeared to be pretty symmetrical and quickly reached an equilibrium position. Instead, above the sloping bed, waves were observed to become asymmetric, thus, causing the asymmetry steady streaming to prevail on the Longuet-Higgins steady streaming. As a consequence, an offshore directed current was measured both at the bottom and slight up in the water due to the undertow. Ripples were considerably asymmetrical, i.e. with offshore half-wavelengths larger than onshore ones, and migrated downward of the sloping bottom.

At a later time, the rippled bed was fixed without altering its slope and roughness. The fixed rippled bed allowed to examine, more in details, the flow field along the flume. Phase and period averaged velocity profiles showed the effects of the ripple shape on the near bed flow. Indeed, on the ripple located within the plane bed, an onshore directed steady streaming appeared above the ripple lee flank and an offshore directed steady streaming appeared above the ripple stoss flank. The interaction between these two currents is in good agreement with the morphodynamic measured within the moveable bed experiments. Moreover, the analysis of the turbulence shed a light on the differences in terms of ripple shape and migration velocity previously measured above the sloping bed. Both the turbulent kinetic energy and the Reynolds stress extends up to 1-2 cm from the bottom, whereas, above the sloping bed the turbulence was considerable throughout the water depth. This occurrence caused a strong flow stirring which, combined with the undertow, was able to move suspended sediments offshore, i.e. in the direction of the observed ripple migration.

A similar flow field was observed throughout the experimental campaign carried out within the large scale wave flume of the Polytechnic University of Catalonia (Spain). There, the hydrodynamics generated by a plunging wave above a sloping hard bed was measured. In particular, the effects induced on the flow by the presence of a breaking bar were examined. Both the mean and the turbulent components of the velocity were analysed. Approaching the surf zone, the wave propagation triggers the appearance of the Stokes drift in the proximity of the water surface and, in turn, of the undertow down in the water, as well as in the small scale campaign. Such offshore directed current was measured throughout

the bar and reached its maximum above the trough. In the surf zone, the plunging jet considerably increased the vertical velocity component in the downward direction just beyond the bar trough and, consequently, the vertical component in the upward direction above the bar trough. This flow stirring could raise a large amount of sediment which could be transported offshore by the aforementioned undertow. Here again, the sloping bed caused the velocity skewness, asymmetry and undertow to increase. Thus, the turbulence in terms of the Reynolds stress not to vanish outside the bottom boundary layer.

Throughout these campaigns, the wave current interaction and its effects on sediment transport were analysed in two-dimensional situations. On the other hand, the fourth campaign aimed to analyse a three dimensional situation, with waves and current at a right angle, to give a more complete overview of the nearshore hydrodynamics. The analysis was performed within the shallow water basin of the DHI (Denmark). The basin is able to generate both waves and current, thus allowing to filter out the influence of the bed slope on the flow. The hydrodynamics was measured focussing on the bottom boundary layer. Both wave and current dominated conditions were investigated. Two roughness conditions were examined, i.e. respectively the sand and the gravel covered bottom.In the current dominated condition the wave superimposition caused the equivalent roughness to increase. This phenomenon weakened with the current velocity increase. In the wave dominated condition, on the sandy bed, the wave superimposition gave rise to a flow relaminarization which made the equivalent roughness to considerably decrease.

Bibliography

Akhavan, R., Kamm, R., and Shapiro, A. (1991). An investigation of transition to turbulence in bounded oscillatory stokes flows part 1. experiments. *Journal of Fluid Mechanics*, 225:395–422.

Andersen, K. H. (1999). *The dynamics of ripples beneath surface waves and topics in shell models of turbulence*. Københavns universitet, Det Naturvidenskabelige fakultet.

Andersen, K. H. and Faraci, C. (2003). The wave plus current flow over vortex ripples at an arbitrary angle. *Coastal engineering*, 47(4):431–441.

Armenio, V. and Sarkar, S. (2002). An investigation of stably stratified turbulent channel flow using large-eddy simulation. *Journal of fluid mechanics*, 459:1–42.

Arnskov, M., Fredsøe, J., and Sumer, B. (1993). Bed shear stress measurements over a smooth bed in three-dimensional wave-current motion. *Coastal Engineering*, 20(3-4):277–316.

Aydin, I. (1987). *Computation and analysis of unsteady turbulent flow on flat bottom and over rigid ripples*. PhD thesis, Tohoku University.

Bagnold, R. A. (1946). Motion of waves in shallow water. interaction between waves and sand bottoms. In *Proceedings of the Royal Society of London A: Mathematical, Physical and Engineering Sciences*, volume 187, pages 1–18. The Royal Society.

Bagnold, R. A. (1947). Sand movement by waves: some small-scale experiments with sand of very low density. *Journal of the Institute of Civil Engineers*, 27(5554):447–469.

Bakker, W. (1974). Sand concentration in an oscillatory flow, paper pre-sented at 14th coastal engineering conference. *Am. Soc. Civ. Eng., Copenhagen*.

Bakker, W. T. and Van Doorn, T. (1978). Near-bottom velocities in waves with a current. In *Coastal Engineering 1978*, pages 1394–1413. Elsevier.

Batchelor, G. K. (2000). *An introduction to fluid dynamics*. Cambridge university press.

Battjes, J. (1988). Surf-zone dynamics. *Annual Review of Fluid Mechanics*, 20(1):257–291.

Bayazit, M. (1976). Free surface flow in a channel of large relative roughness. *Journal of Hydraulic Research*, 14(2):115–126.

Bayazit, M. (1983). Flow structure and sediment transport mechanics in steep channels. In *Euromech*, volume 156, pages 197–206.

Bijker, E., Hijum, E. v., and Vellinga, P. (1976). Sand transport by waves proc. In *15th Coastal Eng. Conf., Honolulu*, volume 2, pages 1149–1167.

Bijker, E. W. (1969). Littoral drift as function of waves and current. In *Coastal Engineering 1968*, pages 415–435. Elsevier.

Bijker, E. W., Kalkwijk, J. P. T., and Pieter, T. (1974). Mass transport in gravity waves on a sloping bottom. In *Coastal Engineering Proceedings*, pages 447–465. ASCE, Elsevier.

Binder, G. and Favre-Marinet, M. (1979). The inner layer in unsteady turbulent boundary layers.

Blondeaux, P. (1990). Sand ripples under sea waves. part I: ripple formation. *Journal of Fluid Mechanics*, 218(1):1–17.

Blondeaux, P., Foti, E., and Vittori, G. (2015). A theoretical model of asymmetric wave ripples. *Philosophical Transactions of the Royal Society of London A: Mathematical, Physical and Engineering Sciences*, 373(2033):20140112.

Blondeaux, P. and Seminara, G. (1979). Transizione incipiente al fondo di un'onda di gravitá. *Acc. Naz. Lincei*, 67:408–411.

Blondeaux, P. and Vittori, G. (1991). Vorticity dynamics in an oscillatory flow over a rippled bed. *Journal of Fluid Mechanics*, 226:257–289.

Boussinesq, J. (1877). *Essai sur la théorie des eaux courantes*. Impr. nationale.

Brebner, A., Askew, J., and Law, S. (1967). The effect of roughness on the mass-transport of progressive gravity waves. In *Coastal Engineering 1966*, pages 175–184. Elsevier.

Brevik, I. (1981). Oscillatory rough turbulent boundary layers. *Journal of the Waterway, Port, Coastal and Ocean Division*, 107(3):175–188.

Brevik, I. and Bjørn, A. (1979). Flume experiment on waves and currents. i. rippled bed. *Coastal Engineering*, 3:149–177.

Brinkkemper, J., Bakker, A., and Ruessink, B. (2017). Intrawave sand suspension in the shoaling and surf zone of a field-scale laboratory beach. *Journal of Geophysical Research: Earth Surface*, 122(1):356–370.

Caligny, A. F. H. d. (1878). *Experiences sur les mouvements des molecules liquid des ondes courant, considerees dans leur mode d'action sur la marche des navires*. Comptes rendus de l'Académie des Sciences.

Camenen, B., Larson, M., and Bayram, A. (2009). Equivalent roughness height for plane bed under oscillatory flow. *Estuarine, Coastal and Shelf Science*, 81(3):409–422.

Carstens, M., Neilson, F. M., and Altinbilek, H. D. (1969). Bed forms generated in the laboratory under an oscillatory flow: Analytical and experimental study. Technical Report 28, US Army Corps of Engineers.

Cavallaro, L., Scandura, P., and Foti, E. (2011). Turbulence-induced steady streaming in an oscillating boundary layer: On the reliability of turbulence closure models. *Coastal Engineering*, 58(4):290–304.

Christoffersen, J. (1980). A simple turbulence model for a three-dimensional current wave motion on a rough bed. *Int. Rep. no. 1, Inst. Hydrodyn. Hydr. Engng (ISVA), Tech. Univ. Denmark*.

Clauser, F. H. (1956). The turbulent boundary layer. In *Advances in applied mechanics*, volume 4, pages 1–51. Elsevier.

Collins, J. (1963). Inception of turbulence at the bed under periodic gravity waves. *Journal of Geophysical Research*, 68(21):6007–6014.

Costamagna, P., Vittori, G., and Blondeaux, P. (2003). Coherent structures in oscillatory boundary layers. *Journal of Fluid Mechanics*, 474:1–33.

Cox, D. T. and Kobayashi, N. (2000). Identification of intense, intermittent coherent motions under shoaling and breaking waves. *Journal of Geophysical Research: Oceans*, 105(C6):14223–14236.

Davies, A. and Li, Z. (1997). Modelling sediment transport beneath regular symmetrical and asymmetrical waves above a plane bed. *Continental Shelf Research*, 17(5):555–582.

De Serio, F. and Mossa, M. (2006). Experimental study on the hydrodynamics of regular breaking waves. *Coastal Engineering*, 53(1):99–113.

Dean, R. G. and Dalrymple, R. A. (1991). *Water wave mechanics for engineers and scientists*, volume 2. World Scientific Publishing Company.

Deigaard, R. et al. (1992). *Mechanics of coastal sediment transport*, volume 3. World scientific publishing company.

Deigaard, R., Jakobsen, J. B., and Fredsøe, J. (1999). Net sediment transport under wave groups and bound long waves. *Journal of Geophysical Research: Oceans*, 104(C6):13559–13575.

Dingler, J. R. and Inman, D. L. (1976). Wave-formed ripples in nearshore sands. *Coastal Engineering Proceedings*, 1(15).

Doucette, J. and O'Donoghue, T. (2006). Response of sand ripples to change in oscillatory flow. *Sedimentology*, 53(3):581–596.

Falcomer, L., Armenio, V., and Tassan-Toffola, M. (2001). Large eddy simulation of secondary flows over longitudinally-ridged walls. In *TSFP DIGITAL LIBRARY ONLINE*. Begel House Inc.

Faraci, C. (2018). Experimental investigation of the hydro-morphodynamic performances of a geocontainer submerged reef. *Journal of Waterway, Port, Coastal, and Ocean Engineering*, 144(2).

Faraci, C. and Foti, E. (2002). Geometry, migration and evolution of small-scale bedforms generated by regular and irregular waves. *Coastal Engineering*, 47(1):35–52.

Faraci, C., Foti, E., Marini, A., and Scandura, P. (2012). Waves plus currents crossing at a right angle: sandpit case. *Journal of Waterway, Port, Coastal, and Ocean Engineering*, 138(5):339–361.

Faraci, C., Foti, E., and Musumeci, R. (2008). Waves plus currents at a right angle: The rippled bed case. *Journal of Geophysical Research: Oceans*, 113(C7). doi: 10.1029/2007JC004468.

Faraci, C., Scandura, P., Musumeci, R., and Foti, E. (2018). Waves plus currents crossing at a right angle: near-bed velocity statistics. *Journal of Hydraulic Research*, 0(0):1–18.

Flores, N. Z. and Sleath, J. F. (1998). Mobile layer in oscillatory sheet flow. *Journal of Geophysical Research: Oceans*, 103(C6):12783–12793.

Fredsøe, J., Andersen, K. H., and Sumer, B. M. (1999). Wave plus current over a ripple-covered bed. *Coastal Engineering*, 38(4):177–221.

Fuhrman, D. R., Fredsøe, J., and Sumer, B. M. (2009). Bed slope effects on turbulent wave boundary layers: 2. comparison with skewness, asymmetry, and other effects. *Journal of Geophysical Research: Oceans*, 114(C3).

George, C. and Sleath, J. (1979). Measurements of combined oscillatory and steady flow over a rough bed. *Journal of Hydraulic Research*, 17(4):303–313.

Germano, M., Piomelli, U., Moin, P., and Cabot, W. H. (1990). A dynamic subgrid-scale eddy viscosity model. In *Studying Turbulence Using Numerical Simulation Databases. 3: Proceedings of the 1990 Summer Program*.

Goring, D. G. and Nikora, V. I. (2002). Despiking acoustic doppler velocimeter data. *Journal of Hydraulic Engineering*, 128(1):117–126.

Govender, K., Michallet, H., and Alport, M. (2011). Dciv measurements of flow fields and turbulence in waves breaking over a bar. *European Journal of Mechanics-B/Fluids*, 30(6):616–623.

Govender, K., Mocke, G., and Alport, M. (2002). Video-imaged surf zone wave and roller structures and flow fields. *Journal of Geophysical Research: Oceans*, 107(C7).

Grant, W. (1975). Discussion of "friction factors under oscillatory waves" by jw kamphuis. *Journal of the Waterways, Harbors, and Coastal Engineering Dis., ASCE*, 101:466–467.

Grant, W. D. (1977). *Bottom friction under waves in the presence of a weak current: it's relationship to coastal sediment transport.* PhD thesis, Massachusetts Institute of Technology.

Grant, W. D. and Madsen, O. S. (1979). Combined wave and current interaction with a rough bottom. *Journal of Geophysical Research: Oceans*, 84(C4):1797–1808.

Grant, W. D. and Madsen, O. S. (1986). The continental-shelf bottom boundary layer. *Annual review of fluid mechanics*, 18(1):265–305.

Grant, W. D., Williams, A. J., Glenn, S. M., and Cacchione, D. A. (1983). High frequency bottom stress variability and its prediction in the code region. Technical report, Woods Hole Oceanographic Institution.

Grasmeijer, B. and Kleinhans, M. (2004). Observed and predicted bed forms and their effect on suspended sand concentrations. *Coastal Engineering*, 51(5):351–371.

Guizien, K., Dohmen-Janssen, M., and Vittori, G. (2003). 1dv bottom boundary layer modeling under combined wave and current: Turbulent separation and phase lag effects. *Journal of Geophysical Research: Oceans*, 108(C1).

Hattori, M. (1987). Experimental study on the validity range of various wave theories. In *Coastal Engineering 1986*, pages 232–246. Elsevier.

Heller, V. (2011). Scale effects in physical hydraulic engineering models. *Journal of Hydraulic Research*, 49(3):293–306.

Henn, D. S. and Sykes, R. I. (1999). Large-eddy simulation of flow over wavy surfaces. *Journal of Fluid Mechanics*, 383:75–112.

Hino, M., Sawamoto, M., and Takasu, S. (1976). Experiments on transition to turbulence in an oscillatory pipe flow. *Journal of Fluid Mechanics*, 75(2):193–207.

Holmedal, L. E. and Myrhaug, D. (2006). Boundary layer flow and net sediment transport beneath asymmetrical waves. *Continental Shelf Research*, 26(2):252–268.

Holmedal, L. E. and Myrhaug, D. (2009). Wave-induced steady streaming, mass transport and net sediment transport in rough turbulent ocean bottom boundary layers. *Continental Shelf Research*, 29(7):911–926.

Huang, Z. and Mei, C. C. (2003). Effects of surface waves on a turbulent current over a smooth or rough seabed. *Journal of Fluid Mechanics*, 497:253–287.

Huang, Z.-C., Hsiao, S.-C., Hwung, H.-H., and Chang, K.-A. (2009). Turbulence and energy dissipations of surf-zone spilling breakers. *Coastal Engineering*, 56(7):733–746.

Hughes, S. A. (1993). *Physical models and laboratory techniques in coastal engineering*, volume 7. World Scientific.

Hurther, D., Thorne, P. D., Bricault, M., Lemmin, U., and Barnoud, J.-M. (2011). A multi-frequency acoustic concentration and velocity profiler (acvp) for boundary layer measurements of fine-scale flow and sediment transport processes. *Coastal Engineering*, 58(7):594–605.

Inman, D. L. and Bowen, A. J. (1962). Flume experiments on sand transport by waves and currents. *Coastal Engineering Proceedings*, 1(8):11.

Jensen, B., Sumer, B., and Fredsøe, J. (1989). Turbulent oscillatory boundary layers at high reynolds numbers. *Journal of Fluid Mechanics*, 206:265–297.

Johns, B. (1975). The form of the velocity profile in a turbulent shear wave boundary layer. *Journal of Geophysical Research*, 80(36):5109–5112.

Jonsson, I. (1963). Measurements in the turbulent wave boundary layer. In *Proc. 10th Congress of IAHR*, volume 1, pages 85–92.

Jonsson, I. (1976). Discussion of: Friction factor under oscillatory waves, by jw kamphuis. *J. Waterw., Harbors Coastal Eng. Div*, 102.

Jonsson, I. G. (1966). *The friction factor for a current superimposed by waves*. Coastal engineering laboratory, hydraulic laboratory, technical University of Denmark.

Jonsson, I. G. (1967). Wave boundary layers and friction factors. In *Coastal Engineering 1966*, pages 127–148.

Jonsson, I. G. (1980). A new approach to oscillatory rough turbulent boundary layers. *Ocean Engineering*, 7(1):109–152.

Jonsson, I. G. (1990). Wave-current interactions. *The Sea: Ocean Engineering Science*, 9:65–119.

Jonsson, I. G. and Carlsen, N. A. (1976). Experimental and theoretical investigations in an oscillatory turbulent boundary layer. *Journal of Hydraulic Research*, 14(1):45–60.

Kajiura, K. (1968). A model of the bottom boundary layer in water waves. *Bull. Earthquake Res. Inst. Univ. Tokyo*, 46:75–123.

Kamphuis, J. (1974). Determination of sand roughness for fixed beds. *Journal of Hydraulic Research*, 12(2):193–203.

Kamphuis, J. W. (1975). Friction factor under oscillatory waves. *Journal of the Waterways, Harbors and Coastal Engineering Division*, 101(2):135–144.

Kemp, P. and Simons, R. (1982). The interaction between waves and a turbulent current: waves propagating with the current. *Journal of Fluid Mechanics*, 116:227–250.

Kemp, P. and Simons, R. (1983). The interaction of waves and a turbulent current: waves propagating against the current. *Journal of fluid mechanics*, 130:73–89.

Khelifa, A. and Ouellet, Y. (2000). Prediction of sand ripple geometry under waves and currents. *Journal of waterway, port, coastal, and ocean engineering*, 126(1):14–22.

King, C. A. M. (1948). *Ph.D. Dissertation*. PhD thesis, Cambridge University (unpublished).

Kobus, H. (1980). Hydraulic modelling. german association for water resources and land improvement. *Bulletin*, 7.

Koca, K., Noss, C., Anlanger, C., Brand, A., and Lorke, A. (2017). Performance of the vectrino profiler at the sediment–water interface. *Journal of Hydraulic Research*, pages 1–9.

Kundu, P. K., Cohen, I. M., and Dowling, D. R. (1990). Fluid mechanics.

Lavelle, J. and Mofjeld, H. (1983). Effects of time-varying viscosity on oscillatory turbulent channel flow. *Journal of Geophysical Research: Oceans*, 88(C12):7607–7616.

Le Méhauté, B. (1990). Similitude. *The sea ocean engineering science*, 9:955–980.

Li, H. (1954). Stability of oscillatory laminar flow along a wall. *Tech. Memo. No. 47*.

Lim, K. Y. and Madsen, O. S. (2016). An experimental study on near-orthogonal wave–current interaction over smooth and uniform fixed roughness beds. *Coastal Engineering*, 116:258–274.

Liu, P. L. (1977). Mass transport in the free-surface boundary layers. *Coastal Engineering*, 1:207–219.

Liu, Y. and Faraci, C. (2014). Analysis of orthogonal wave reflection by a caisson with open front chamber filled with sloping rubble mound. *Coastal Engineering*, 91:151–163.

Lodahl, C., Sumer, B. M., and Fredsøe, J. (1998). Turbulent combined oscillatory flow and current in a pipe. *Journal of Fluid Mechanics*, 373:313–348.

Long, C. E. (1981). A simple model for time-dependent, stably stratified turbulent boundary layers.

Longuet-Higgins, M. (1958). The mechanics of the boundary layer near the bottom in a progressive wave. In *Proceedings of the 6th International Conference on Coastal Engineering, Berkeley (CA), ASCE*, volume 184, page 193.

Longuet-Higgins, M. S. (1953). Mass transport in water waves. *Philosophical Transactions of the Royal Society of London A: Mathematical, Physical and Engineering Sciences*, 245(903):535–581.

Longuet-Higgins, M. S. (1981). Oscillating flow over steep sand ripples. *Journal of Fluid Mechanics*, 107:1–35.

Lwin, K., Liu, H., and Sato, S. (2012). The role of steady streaming in sheetflow transport. In *Asian And Pacific Coasts 2011*, pages 902–909. World Scientific.

Malarkey, J. and Davies, A. (2012). Free-stream velocity descriptions under waves with skewness and asymmetry. *Coastal Engineering*, 68:78–95.

Mansard, E. P. and Funke, E. (1980). The measurement of incident and reflected spectra using a least squares method. In *Coastal Engineering 1980*, pages 154–172.

Martin, H. and Pohl, R. (2000). Technische hydromechanik 4 (technical hydromechanics). *Verlag für Bauwesen, Berlin [in German]*.

Mathisen, P. and Madsen, O. (1997). Waves and currents over a fixed rippled bed 2. bottom and apparent roughness experienced by currents in the presence of waves. *Oceanographic Literature Review*, 5(44):430.

Mathisen, P. P. and Madsen, O. S. (1996). Waves and currents over a fixed rippled bed: 1. bottom roughness experienced by waves in the presence and absence of currents. *Journal of Geophysical Research: Oceans*, 101(C7):16533–16542.

Meneveau, C., Lund, T. S., and Cabot, W. H. (1996). A lagrangian dynamic subgrid-scale model of turbulence. *Journal of fluid mechanics*, 319:353–385.

Musumeci, R., Cavallaro, L., Foti, E., Scandura, P., and Blondeaux, P. (2006). Waves plus currents crossing at a right angle: Experimental investigation. *Journal of Geophysical Research: Oceans*, 111(C7).

Musumeci, R. E., Svendsen, I. A., and Veeramony, J. (2005). The flow in the surf zone: a fully nonlinear boussinesq-type of approach. *Coastal Engineering*, 52(7):565–598.

Myrhaug, D. (1982). On a theoretical model of rough turbulent wave boundary layers. *Ocean Engineering*, 9(6):547–565.

Myrhaug, D., Holmedal, L. E., Simons, R. R., and MacIver, R. D. (2001). Bottom friction in random waves plus current flow. *Coastal Engineering*, 43(2):75–92.

Nadaoka, K., Hino, M., and Koyano, Y. (1989). Structure of the turbulent flow field under breaking waves in the surf zone. *Journal of Fluid Mechanics*, 204:359–387.

Nadaoka, K. and Kondoh, T. (1982). Laboratory measurements of velocity field structure in the surf zone by ldv. *Coastal Engineering in Japan*, 25(1):125–145.

Nielsen, P. (1979). *Some Basic Concepts of Wave Sediment Transport*. Institute of Hydrodynamics and Hydraulic Engineering København: Series paper. Institute of Hydrodynamics and Hydraulic Engineering, Technical University of Denmark.

Nielsen, P. (1981). Dynamics and geometry of wave-generated ripples. *Journal of Geophysical Research: Oceans*, 86(C7):6467–6472.

Nielsen, P. (1992). *Coastal bottom boundary layers and sediment transport*, volume 4. World scientific.

Novák, P. and Cabelka, J. (1981). *Models in hydraulic engineering; physical principles and design applications*. Pitman Advanced Publishing Program.

O'Donoghue, T., Doucette, J., Van der Werf, J., and Ribberink, J. (2006). The dimensions of sand ripples in full-scale oscillatory flows. *Coastal Engineering*, 53(12):997–1012.

Okayasu, A., Shibayama, T., and Mimura, N. (1987). Velocity field under plunging waves. In *Coastal Engineering 1986*, pages 660–674. Elsevier.

Ourmieres, Y. and Chaplin, J. (2004). Visualizations of the disturbed-laminar wave-induced flow above a rippled bed. *Experiments in Fluids*, 36(6):908–918.

Oweis, G. F., Winkel, E. S., Cutbrith, J. M., Ceccio, S. L., Perlin, M., and Dowling, D. R. (2010). The mean velocity profile of a smooth-flat-plate turbulent boundary layer at high reynolds number. *Journal of Fluid Mechanics*, 665:357–381.

Peregrine, D. (1976). Interaction of water waves and currents. *Advances in applied mechanics.*, 16:9–117.

Peregrine, D. H. (1983). Breaking waves on beaches. *Annual Review of Fluid Mechanics*, 15(1):149–178.

Petrotta, C., Faraci, C., Scandura, P., and Foti, E. (2017a). The flow over asymmetrical ripples: an experimental investigation on the hydrodynamics behavior. *Procc. of Coastal Dynamics*.

Petrotta, C., Faraci, C., Scandura, P., and Foti, E. (2017b). Hydrodynamics above fixed asymmetrical ripples. *Proc. SCACR*, 6.

Petrotta, C., Faraci, C., Scandura, P., and Foti, E. (2018). Experimental investigation on sea ripple evolution over sloping beaches. *Ocean Dynamics*.

Ranasoma, K. M. and Sleath, J. F. (1994). Combined oscillatory and steady flow over ripples. *Journal of waterway, port, coastal, and ocean engineering*, 120(4):331–346.

Raudkivi, A. J. (1997). Ripples on stream bed. *Journal of Hydraulic Engineering*, 123(1):58–64.

Raudkivi, A. J. (1998). *Loose boundary hydraulics*. CRC Press.

Ribberink, J. S. and Al-Salem, A. A. (1995). Sheet flow and suspension of sand in oscillatory boundary layers. *Coastal engineering*, 25(3-4):205–225.

Roesler, T. C., Stevenson, W. H., and Thompson, H. D. (1980). Investigation of bias errors in laser doppler velocimeter measurements. Technical report, PURDUE UNIV LAFAYETTE IND SCHOOL OF MECHANICAL ENGINEERING.

Ruessink, B. (2010). Observations of turbulence within a natural surf zone. *Journal of Physical Oceanography*, 40(12):2696–2712.

Salon, S., Armenio, V., and Crise, A. (2007). A numerical investigation of the stokes boundary layer in the turbulent regime. *Journal of Fluid Mechanics*, 570:253–296.

Sarghini, F., Piomelli, U., and Balaras, E. (1999). Scale-similar models for large-eddy simulations. *Physics of Fluids*, 11(6):1596–1607.

Scandura, P. (2007). Steady streaming in a turbulent oscillating boundary layer. *Journal of Fluid Mechanics*, 571:265–280.

Scandura, P., Faraci, C., and Foti, E. (2016). A numerical investigation of acceleration-skewed oscillatory flows. *Journal of Fluid Mechanics*, 808:576–613.

Scandura, P., van der Zanden, J., Petrotta, C., Faracis, C., Cooper, J., Clark, S., Eltard-Larsen, B., Carstensen, S., Fuhrman, D. R., Caceres, I., et al. (2018). Hydrodynamics under large-scale waves breaking over a barred beach. In *7th International Conference on the Application of Physical Modelling in Coastal and Port Engineering and Science (Coastlab18)*.

Scandura, P., Vittori, G., and Blondeaux, P. (2000). Three-dimensional oscillatory flow over steep ripples. *Journal of Fluid Mechanics*, 412:355–378.

Schüttrumpf, H. and Oumeraci, H. (2005). Scale and model effects in crest level design. In *Proc. 2nd Coastal Symposium. Höfn. Iceland*.

Scott, C. P., Cox, D. T., Maddux, T. B., and Long, J. W. (2005). Large-scale laboratory observations of turbulence on a fixed barred beach. *Measurement Science and Technology*, 16(10):1903.

Sergeev, S. (1966). Fluid oscillations in pipes at moderate reynolds numbers. *Fluid Dynamics*, 1(1):121–122.

Simons, R. R., Grass, T. J., and Mansour-Tehrani, M. (1993). Bottom shear stresses in the boundary layers under waves and currents crossing at right angles. In *Coastal Engineering 1992*, pages 604–617. Elsevier.

Simons, R. R., Grass, T. J., Saleh, W. M., and Tehrani, M. M. (1995). Bottom shear stresses under random waves with a current superimposed. In *Coastal Engineering 1994*, pages 565–578. Elsevier.

Simons, R. R., MacIver, R. D., and Saleh, W. M. (1997). Kinematics and shear stresses from combined waves and longshore currents in the uk coastal research facility. In *Coastal Engineering 1996*, pages 3481–3494. Elsevier.

Sleath, J. (1982). Friction coefficients of rippled beds in oscillatory flow. *Continental Shelf Research*, 1(1):33–47.

Sleath, J. (1990). Seabed boundary layers. *The sea B*, 9:693–727.

Sleath, J. (1991). Velocities and bed friction in combined flows. In *Coastal Engineering 1990*, pages 450–463. Elsevier.

Sleath, J. F. (1984). *Sea bed mechanics*. John Wiley and Sons Inc., New York, NY.

Smith, E. R. and Kraus, N. C. (1991). Laboratory study of wave-breaking over bars and artificial reefs. *Journal of waterway, port, coastal, and ocean engineering*, 117(4):307–325.

Smith, J. D. (1975). Modeling of sediment transport on continental shelves. Technical report, Washington Univ., Seattle (USA). Dept. of Oceanography.

Soulsby, R., Whitehouse, R., et al. (1997). Threshold of sediment motion in coastal environments. In *Pacific Coasts and Ports' 97: Proceedings of the 13th Australasian Coastal and Ocean Engineering Conference and the 6th Australasian Port and Harbour Conference; Volume 1*, page 145. Centre for Advanced Engineering, University of Canterbury.

Soulsby, R. L., Hamm, L., Klopman, G., Myrhaug, D., Simons, R. R., and Thomas, G. P. (1993). Wave-current interaction within and outside the bottom boundary layer. *Coastal engineering*, 21(1-3):41–69.

Stokes, G. G. (1847). On the theory of oscillatory waves. *Transactions of the Cambridge Philosophical Society*, 8:441.

Stringer, M., Allmond, J., Proto, C., Wilson, D., and Kutter, B. (2014). Evaluating the response of new pore pressure transducers for use in dynamic centrifuge tests. *Physical Modelling in Geotechnics*.

Sumer, B. M., Guner, H., Hansen, N. M., Fuhrman, D. R., and Fredsøe, J. (2013). Laboratory observations of flow and sediment transport induced by plunging regular waves. *Journal of Geophysical Research: Oceans*, 118(11):6161–6182.

Sunamura, T. (1980). A laboratory study of offshore transport of sediment and a model for eroding beaches. In *Coastal Engineering 1980*, pages 1051–1070. Elsevier.

Swart, D. H. (1974). *Offshore sediment transport and equilibrium beach profiles*. PhD thesis, TU Delft, Delft University of Technology.

Thomas, R., Schindfessel, L., McLelland, S., Creëlle, S., and De Mulder, T. (2017). Bias in mean velocities and noise in variances and covariances measured using a multistatic acoustic profiler: the nortek vectrino profiler. *Measurement Science and Technology*, 28(7):075302.

Ting, F. C. and Kirby, J. T. (1994). Observation of undertow and turbulence in a laboratory surf zone. *Coastal Engineering*, 24(1):51 – 80.

Ting, F. C. and Kirby, J. T. (1995). Dynamics of surf-zone turbulence in a strong plunging breaker. *Coastal Engineering*, 24(3-4):177–204.

Ting, F. C. and Kirby, J. T. (1996). Dynamics of surf-zone turbulence in a spilling breaker. *Coastal Engineering*, 27(3-4):131–160.

Trowbridge, J. and Madsen, O. S. (1984a). Turbulent wave boundary layers: 1. model formulation and first-order solution. *Journal of Geophysical Research: Oceans*, 89(C5):7989–7997.

Trowbridge, J. and Madsen, O. S. (1984b). Turbulent wave boundary layers: 2. second-order theory and mass transport. *Journal of Geophysical Research: Oceans*, 89(C5):7999–8007.

Tunstall, E. B. and Inman, D. L. (1975). Vortex generation by oscillatory flow over rippled surfaces. *Journal of Geophysical Research*, 80(24):3475–3484.

Van Der A, D. A., Van Der Zanden, J., O'Donoghue, T., Hurther, D., Cáceres, I., McLelland, S. J., and Ribberink, J. S. (2017a). Large-scale laboratory study of breaking wave hydrodynamics over a fixed bar. *Journal of Geophysical Research: Oceans*, 122(4):3287–3310.

Van Der A, D. A., Van Der Zanden, J., O'Donoghue, T., Hurther, D., Cáceres, I., McLelland, S. J., and Ribberink, J. S. (2017b). Large-scale laboratory study of breaking wave hydrodynamics over a fixed bar. *Journal of Geophysical Research: Oceans*, 122(4):3287–3310.

Van der Werf, J., Doucette, J., O'Donoghue, T., and Ribberink, J. (2007). Detailed measurements of velocities and suspended sand concentrations over full-scale ripples in regular oscillatory flow. *Journal of Geophysical Research: Earth Surface*, 112(F2).

van der Zanden, J. (2016). *Sand transport processes in the surf and swash zones*. University of Twente.

van der Zanden, J., Van Der A, D., Hurther, D., Cáceres, I., O'Donoghue, T., and Ribberink, J. (2016). Near-bed hydrodynamics and turbulence below a large-scale plunging breaking wave over a mobile barred bed profile. *Journal of Geophysical Research: Oceans*, 121(8):6482–6506.

Van Der Zanden, J., van der A, D. A., Cáceres, I., Hurther, D., McLelland, S. J., Ribberink, J. S., and O'Donoghue, T. (2018). Near-bed turbulent kinetic energy budget under a large-scale plunging breaking wave over a fixed bar. *Journal of geophysical research: Oceans*, 123(2):1429–1456.

van Doorn, J. (1981). Experimental investigation of near-bottom velocities in water waves without and with a current. *M1423*.

Van Hoften, J. and Karaki, S. (1977). Interaction of waves and a turbulent current. *Coastal Engineering Proceedings*, pages 404–422.

Van Rijn, L. C. (1993). *Principles of sediment transport in rivers, estuaries and coastal seas*, volume 1006. Aqua publications Amsterdam.

Visser, P. J. (1986). Wave basin experiments on bottom friction due to current and waves. *Coastal Engineering Proceedings*, 1(20).

Vittori, G. and Verzicco, R. (1998). Direct simulation of transition in an oscillatory boundary layer. *Journal of Fluid Mechanics*, 371:207–232.

Welch, P. (1967). The use of fast fourier transform for the estimation of power spectra: a method based on time averaging over short, modified periodograms. *IEEE Transactions on audio and electroacoustics*, 15(2):70–73.

Wengrove, M. and Foster, D. (2014). Field evidence of the viscous sublayer in a tidally forced developing boundary layer. *Geophysical Research Letters*, 41(14):5084–5090.

Wu, X. and Squires, K. D. (1998). Numerical investigation of the turbulent boundary layer over a bump. *Journal of Fluid Mechanics*, 362:229–271.

Yalin, M. S. and Yalin, M. S. (1971). *Theory of hydraulic models*. Springer.

Yoon, H.-D. and Cox, D. T. (2010). Large-scale laboratory observations of wave breaking turbulence over an evolving beach. *Journal of Geophysical Research: Oceans*, 115(C10).

Zhang, Z. (2002). Velocity bias in lda measurements and its dependence on the flow turbulence. *Flow Measurement and Instrumentation*, 13(3):63–68.

List of Figures

List of Tables

List of symbols

Roman Symbols

A	orbital displacement amplitude
Asy	Asymmetry
d	water depth
d_{50}	mean particle diameter
f	mass forces
f_w	friction factor
$f_{2.5}$	grain roughness friction factor
H	wave height
H_{max}	maximum wave height
H_s	significant wave height
h	water depth
i	imaginary number
k	angular wavenumber
k	kurtosis
k	turbulent kinetic energy
k_s	virtual wall location
L	wave length
l	mixing length
N	number of waves
P_η	Pressure at the wave surface
p	pressure
p^*	non dimensional pressure
Re	flow Reynolds number
Re_w	wave Reynolds number
Re_c	current Reynolds number

Re_c^*	friction Reynolds number
Re_d	sediment Reynolds number
Re_δ	Reynolds number just outside the boundary layer
r	roughness
S	standard deviation
Sk	free stream velocity skewness
s	relative density of sediments
s	PDF skewness
T	wave period
T_{gr}	wave group period
T_m	wave mean period
T_p	wave peak period
t	time
t^*	non dimensional time
U	velocity
U_x	velocity in the direction of the x axis
U_c	current velocity
U_{AVG}	outer flow averaged velocity
U_{MA}	moving averaged velocity
U_{max}	maximum velocity during the cycle
U_{min}	minimum velocity during the cycle
U_0	amplitude of velocity oscillation in the outer flow
U_+	dimensionless law-of-the-wall velocity
U_∞	outer flow velocity in the direction of the x axis
$\overline{U}$	second-order drift velocity in the direction of the x axis
$< U >$	ensemble averaged velocity in the direction of the x axis
u_i	observed velocity
u'	turbulent fluctuating velocity in the direction of the x axis
u_*	friction velocity in the direction of the x axis
u^*	non dimensional velocity component in the direction of the x axis
$\overline{u}$	period averaged velocity in the direction of the x axis
$\tilde{u}$	oscillating velocity in the direction of the x axis
$\dot{u}_{max}$	maximum acceleration during the cycle
$\dot{u}_{min}$	minimum acceleration during the cycle
v'	turbulent fluctuating velocity in the direction of the y axis
v_0	ripple crest migration velocity
W	velocity in the direction of the z axis

$W1$	velocity in the direction of the z axis as measured by Vectrinos
$W2$	velocity in the direction of the z axis as measured by Vectrinos
w'	turbulent fluctuating velocity in the direction of the z axis
x	coordinate
x^*	non dimensional coordinate
y	distance to the wall
y^*	non dimensional coordinate
y_+	dimensionless law-of-the-wall distance to the wall
y_0	Nikuradse equivalent roughness
z	coordinate
$z1$, $z2$	Vectrino's coordinates

Greek Symbols

β	acceleration skewness parameter
γ	peak enhancement factor
Δy	displacement thickness
δ	boundary layer thickness
δ_{ij}	Kronecker symbol
η	water surface elevation
η_{eq}	ripple height at the equilibrium
θ	Shields parameter
θ_{crit}	critical Shields parameter
$\theta_{2.5}$	grain roughness Shields parameter
κ	von Kármán constant
λ	ripple wavelength
λ_{eq}	ripple wavelength at the equilibrium
λ_{off}	ripple offshore half-wavelength
λ_{on}	ripple onshore half-wavelength
μ	dynamic viscosity of the water
ν	kinematic viscosity of the water
ν_t	turbulent or eddy viscosity
ϕ	velocity potential function
ρ	water density
ρ_s	sediment density
τ, τ_{xy}	shear stresses
tau^*	non dimensional shear stress

τ_0	shear stress at the wall
ψ	mobility number
ξ	non dimensional distance to the wall
ω	angular frequency of velocity oscillation in the outer flow